

ORIENTATION-PATTERNED GALLIUM ARSENIDE
FOR QUASI-PHASEMATCHED INFRARED NONLINEAR OPTICS

A DISSERTATION
SUBMITTED TO THE DEPARTMENT OF APPLIED PHYSICS
AND THE COMMITTEE ON GRADUATE STUDIES
OF STANFORD UNIVERSITY
IN PARTIAL FULFILLMENT OF THE REQUIREMENTS
FOR THE DEGREE OF
DOCTOR OF PHILOSOPHY

Thierry Jacques Pinguet

March 2002

© Copyright by Thierry J. Pinguet 2002
All rights reserved

I certify that I have read this dissertation and that, in my opinion, it is fully adequate in scope and quality as a dissertation for the degree of Doctor of Philosophy.

James S. Harris, Jr. (Principal Adviser)

I certify that I have read this dissertation and that, in my opinion, it is fully adequate in scope and quality as a dissertation for the degree of Doctor of Philosophy.

Martin M. Fejer

I certify that I have read this dissertation and that, in my opinion, it is fully adequate in scope and quality as a dissertation for the degree of Doctor of Philosophy.

Walter A. Harrison

Approved for the University Committee on Graduate Studies

Abstract

There are numerous applications of nonlinear optical frequency conversion in the infrared, ranging from generation of coherent radiation for spectroscopy and military applications, to wavelength conversion in communication systems. Semiconductors such as $\text{Al}_x\text{Ga}_{1-x}\text{As}$ have excellent properties for nonlinear frequency conversion, in particular large nonlinear coefficients and transparency throughout the mid-infrared. However, the absence of birefringence has severely limited their usefulness. Quasi-phasematching (QPM) provides an alternative solution to the phasematching problem, but requires a modulation of the sign of the nonlinear coefficient along the material. In this work we have developed an all-epitaxial fabrication process for both bulk-like and waveguide devices using orientation patterning in the $\text{Al}_x\text{Ga}_{1-x}\text{As}$ material system and have demonstrated various nonlinear optical interactions which show that orientation-patterned $\text{Al}_x\text{Ga}_{1-x}\text{As}$ is a promising candidate for infrared applications.

Our orientation template is fabricated in three steps. First, we use the polar-on-nonpolar growth of GaAs/Ge/GaAs heterostructure in a molecular beam epitaxy system (MBE) to control lattice inversion. The orientation pattern is then defined by a combination of photolithography and a series of selective chemical etching steps. Finally, we reload the sample in the MBE system for regrowth to complete the template. Orientation-patterned $\text{Al}_x\text{Ga}_{1-x}\text{As}$ films regrown in this fashion exhibit vertical propagation of the antiphase domains under all MBE conditions tested. QPM periods short enough to phasematch any interaction in the transparency range of $\text{Al}_x\text{Ga}_{1-x}\text{As}$ have been demonstrated.

Using this technique, $\text{Al}_x\text{Ga}_{1-x}\text{As}$ QPM waveguide devices were fabricated and we achieved second harmonic generation from a pump laser at 1.55 μm . However, the conversion efficiency in these devices was limited by large propagation losses at both fundamental and harmonic wavelengths that we attributed to corrugation at the core/cladding interfaces. We also grew 0.5 mm thick films of orientation-patterned GaAs in a hydride vapor phase epitaxy reactor using the orientation template as a seed. Antiphase domain boundaries propagated vertically throughout the films for QPM periods as short as 20 μm , sufficient to phasematch nonlinear interactions pumped at 1.3 μm . The thick films exhibited very low attenuation at near-infrared wavelengths. Good long-range homogeneity was confirmed by performing second harmonic generation from an optical parametric oscillator with tunable output around 4 μm with very good agreement to theory. Finally, we demonstrated 8 μm generation from difference frequency

mixing of two near-infrared lasers at 1.3 and 1.55 μm . These results show that orientation-patterned $\text{Al}_x\text{Ga}_{1-x}\text{As}$ is a very attractive solution for nonlinear frequency conversion in the infrared.

Acknowledgements

First of all, I would like to thank Prof. James Harris for being my research advisor during my time at Stanford. Prof. Harris took me into his group at a time when I was uncertain about the direction of my graduate studies, and helped me find the right project. Working in his group has truly been a very enjoyable experience, as well as a great learning experience in the ways of science and research. Prof. Harris has created a unique environment that relies on strong teamwork between the students and a good amount of individual initiative to keep things running. For this, I think I will for the rest of my life be in debt to him.

I would also like to thank Prof. Martin Fejer, who in effect was a co-advisor to this project and the students involved in it. I took great pleasure in listening to him and learning from his seemingly unlimited amount of technical knowledge. Trying to please or impress Prof. Fejer is a great challenge that has made many graduate students shiver, but at the same time has made them better. My thanks go to Prof. Harrison for many good conversations about my research and his help in my first year here, when as a student freshly arrived from France, I was getting confused by the choice of classes offered. I would also like to thank Prof. Feigelson and Prof. Byer for serving on my orals committee.

I enjoyed very much my research project, because of the combination of different disciplines that were involved in it, and the resources available to me to meet the challenges I faced. But while doing research was the primary reason for me coming to Stanford, it is the people that I interacted with every day that truly made it a very special period in my life.

First of all, I want to acknowledge all the students, visiting scholars and postdocs who participated in this project over the years. An immense place is reserved here for Loren Eyres and Chris Ebert, who were collaborators on the first years of this project, and served as role models for me. Loren was the creative driving force, almost in the image of his advisor, Prof. Fejer, in the amount of knowledge and ingenuity he carried around in his head. Chris took me under his wing when I joined the Harris group and

showed me the ropes of MBE. I shared many lunch breaks with him talking about the world and our aspirations. I have missed both of them dearly since they left. Other temporary contributors to this project include Patrick Tourreau, Torbjorn Skauli, Ofer Levi and Konstantin Vodopyanov, all of whom have helped inject new energy when things were slowing down. I am very grateful for their help over the years. I want to wish good luck to Paulina Kuo, Xiaojun Yu, and Luigi Scaccabarozzi, who are taking over after me. I hope the gods of MBE are with you!

My fellow members of the Harris group are very dear to me, and have contributed to this work in more ways than just helping with a technical problem. The atmosphere in our group is unparalleled, and somehow every new addition by our advisor just seems to reinforce it. I will start by remembering the old guard, people who were on their way out when I joined and have taught me how to use most of the equipment and shared their knowledge with me: Chris Coldren, Wayne Martin, Fred Sughwo, Hong Liu, Erji Mao, Sylvia Spruytte and Glenn Solomon. But I have shared most of my waking hours and experiences with a group of remarkable people that I will not forget soon, and that have made my life bearable when outside events were threatening to make it miserable. For this, I want to thank Chien-Chung Lin, Xian Liu, Kai Ma, Vincent Gambin, Rafael Aldaz, Vijit Sabnis, and Evan Thrush; you all have had a lasting influence on me, and I can only hope I am as good a friend to you as you have been to me. My gratitude goes to the rest of the Harris group, for many conversations, parties and help in the lab. I will remember my time in the Harris group very fondly forever.

None of this work would have ever happened without the people that work to keep things running smoothly. Gail Chun-Creech and Lu Miao deserve credit for keeping the Harris group in good shape despite all of our individual problems and our advisor's busy schedule. Paula Perron of Applied Physics was very helpful in keeping us sometimes distracted students aware of our obligations and in accommodating our schedules as well, making the AP department feel like a family. The staff of CIS, while constantly changing, has done a great job of keeping the cleanroom running as smoothly as can be expected, and Tom Carver deserves the gratitude of many students for his efforts in maintaining the Ginzton microfab.

Finally, I want to thank people that were part of my life, while not directly involved in my research. First I want to thank my Physics and Applied Physics classmates, in particular Gordon Keeler, Bianca Nelson, Ali Mokhberi, Mike Rozler, and Aaron Birch. Having people like them around made the transition from France to Northern California easier, and they proved to me that scientists are also real people. Then I want to thank my friends outside of Stanford and in France, who have lived through my lack of correspondence and still somehow want to hear from me. Getting together with them is always fun, and I wish I had more occasions to do so.

I would like to thank my parents for letting their only child go live a few thousand miles away from them, and for never complaining about it. Their continuous support has only reinforced my desire to please them and make them proud of me. My family-in-law has also been very supportive of me, and provided a home-away-from-home, and for this I thank them. And last, but not least, I want to express my love and thanks to my wife and best friend, Nivalda, for all the years that I have know her. More than her strength and desire to make me be the best I can be, it is the balance that she brought to my life that I cherish the most. When she went away more than two years ago to resume her studies, I realized how much she meant to me. She has helped shape the person that I have become as much as my experience at Stanford. Finishing this thesis brings me a great sense of accomplishment, but more than anything, it brings me joy because we will once again be together.

Table of contents

CHAPTER 1: INTRODUCTION.....	1
1.1 MOTIVATIONS.....	1
1.2 INFRARED OPTICS APPLICATIONS	2
1.3 CURRENT INFRARED SOURCES.....	3
1.4 NONLINEAR OPTICS FOR INFRARED APPLICATIONS	4
1.5 INFRARED NONLINEAR OPTICAL MATERIALS	5
1.6 NONLINEAR OPTICS IN SEMICONDUCTORS	7
1.7 ORGANIZATION.....	10
CHAPTER 2: THEORY OF NONLINEAR FREQUENCY CONVERSION.....	11
2.1 PHYSICS OF NONLINEAR OPTICS	11
2.2 NONLINEAR INTERACTIONS OF PLANE WAVES.....	13
2.3 CONVERSION EFFICIENCY AND PHASEMATCHING CONDITIONS.....	16
2.4 DIFFERENCE-FREQUENCY GENERATION AND PARAMETRIC OSCILLATION.....	24
2.5 INTRODUCING REAL-LIFE EFFECTS: TENSOR SYMMETRY AND LOSS	26
2.5.1 <i>Nonlinear tensor symmetry and polarization effects</i>	26
2.5.2 <i>Effects of optical loss on conversion efficiency</i>	27
2.6 FREQUENCY CONVERSION IN WAVEGUIDES.....	29
2.6.1 <i>Waveguide geometry and waveguide modes</i>	30
2.6.2 <i>Conversion efficiency</i>	32
2.7 FREQUENCY CONVERSION IN BULK MATERIAL	33
2.6.3 <i>SHG with focused gaussian beams</i>	34
2.6.4 <i>DFG with focused gaussian beams</i>	35
2.8 CONCLUSION.....	36
CHAPTER 3: ALL-EPITAXIAL ORIENTATION-PATTERNING	37
3.1 LATTICE INVERSION IN GAAS	37
3.2 MOLECULAR BEAM EPITAXY	40
3.2.1 <i>Basic components of an MBE system</i>	41

3.2.2	<i>MBE growth of GaAs</i>	43
3.2.3	<i>MBE growth of Ge</i>	44
3.3	ORIENTATION TEMPLATE FABRICATION PROCESS.....	45
3.3.1	<i>Lattice inversion</i>	45
3.3.2	<i>Template fabrication process</i>	46
3.3.3	<i>MBE regrowth results</i>	52
3.4	CONCLUSION.....	55
 CHAPTER 4: GROWTH AND CHARACTERIZATION OF THICK FILMS OF ORIENTATION-PATTERNED GAAS		57
4.1	HYDRIDE VAPOR PHASE EPITAXY	58
4.2	GROWTH OF 0.5 MM THICK FILMS OF OP-GAAS	59
4.2.1	<i>Antiphase domain propagation and film quality</i>	59
4.2.2	<i>Selective area growth results applied to antiphase domain behavior</i>	65
4.3	ATTENUATION COEFFICIENT MEASUREMENTS IN THICK OP-GAAS FILMS	68
4.4	MATERIAL CHARACTERIZATION USING SECOND-HARMONIC GENERATION	71
4.4.1	<i>SHG setup</i>	71
4.4.2	<i>SHG measurements</i>	72
4.4.3	<i>Measurement of d_{14} of GaAs using SHG at 4 μm</i>	74
4.5	GENERATION OF MID-IR RADIATION BY DIFFERENCE-FREQUENCY MIXING	76
4.6	CONCLUSION.....	79
 CHAPTER 5: QPM ALGAAS WAVEGUIDE DEVICES FOR COMMUNICATION APPLICATIONS		81
5.1	ALGAAS WAVEGUIDES FOR OPTICAL COMMUNICATION APPLICATIONS	81
5.2	WAVEGUIDE DESIGN AND FABRICATION	83
5.2.1	<i>Design considerations</i>	83
5.2.3	<i>Waveguide mode solver</i>	85
5.2.4	<i>Parametric analysis of waveguide design</i>	87
5.2.5	<i>Waveguide fabrication</i>	94
5.3	WAVEGUIDE TESTING USING SHG	97
5.3.1	<i>Loss measurements in patterned waveguides</i>	97

5.3.2	<i>Second harmonic generation setup</i>	99
5.3.3	<i>SHG measurements</i>	100
5.4	CONCLUSION.....	103
CHAPTER 6: CONCLUSION.....		104
6.1	ACCOMPLISHMENTS.....	104
6.1.1	<i>Materials research</i>	104
6.1.2	<i>Nonlinear frequency conversion</i>	105
6.2	FUTURE WORK	106
6.3	CONCLUSION.....	107
BIBLIOGRAPHY		108

List of tables

Table 1.1: Properties of some nonlinear materials.....	7
Table 4.1: Attenuation coefficient in patterned and unpatterned regions of the 2 cm long piece with 26.3 μm period QPM grating, at three near-IR wavelengths. The value of 0.025 cm^{-1} for 1.064 μm was inserted as a comparison, and is taken from [47], where attenuation was measured in a 4 mm long, 200 μm thick piece with 212 μm period, which we considered to be unpatterned compared to the sample considered here.....	70

List of illustrations

Figure 1.1: Schematic of two common types of nonlinear optical interactions.....	4
Figure 1.2: Typical quasi-phases-matched device for frequency conversion. The + and – signs indicate the modulation of the sign of the nonlinear coefficient for maximum conversion efficiency. L_c is called the coherence length and is determined by the nonlinear interaction of interest.	8
Figure 1.3: Orientation template for epitaxial growth of QPM structures. The template can be obtained either by bonding two semiconductor plates, or by the all-epitaxial fabrication technique used in this work.	9
Figure 2.1: The relationship between polarization and applied electric field for (a) a linear dielectric medium, and (b) a nonlinear dielectric medium.	12
Figure 2.2: Tuning curve obtained from the sinc^2 term as a function of dephasing from the optimal phases-matching condition.	20
Figure 2.3: SHG power vs. material length for three different phases-matching conditions. Quasi-phases-matching (QPM) results in quasi-quadratic increase of SHG power with distance, with the effective nonlinear coefficient reduced by $2/\pi$	21
Figure 2.4: Birefringent phases-matching in a negative uniaxial material, with fundamental propagating with ordinary index, and second harmonic with extraordinary index. .	22
Figure 2.5: A typical QPM bulk device, where the fields propagate through sections of alternating signs for the nonlinear coefficient.	23
Figure 2.6: Typical polarization configuration for collinear SHG in GaAs.	27
Figure 2.7: Schematic of two common types of waveguides; a) is a ridge waveguide, the type used in this work, while b) is a representation of an optical fiber found in communication networks.	30
Figure 3.1: The sign of the nonlinear coefficient is changed by inverting the direction of the Ga-As bond in the GaAs lattice, which is equivalent to a 90° rotation of the lattice around the [100] direction.	38
Figure 3.2: The nonpolar Ge layer is used as a buffer to isolate both orientations of the GaAs crystal.	39

Figure 3.3: To achieve the all-epitaxial inversion, we have to use a misoriented Ge surface, as shown in a), and the right growth conditions to get to b), where single-domain GaAs of opposite orientation to that of the substrate is obtained after APDs have annihilated 40

Figure 3.4: Schematic of an MBE system showing the most important parts 42

Figure 3.5: Orientation-patterned GaAs fabrication process: a) MBE growth of inverted layers (indicated by + and -) using GaAs/Ge/GaAs heteroepitaxy, followed by patterning of desired QPM grating with photoresist; b) both orientations are exposed with the patterned period after various chemical etching steps; c) the sample is reloaded in the MBE system for regrowth; d) either the waveguide growth follows or the sample is taken out and put in an HVPE system for thick film growth..... 47

Figure 3.7: The wet-etching steps for the template fabrication involve using selective etchants to control the corrugation depth. The etch-stop layers are also used to isolate the GaAs surface that will be regrown on from contamination such as the photoresist. 51

Figure 3.8: SEM cross-section of MBE-regrown orientation-patterned film, showing clearly the APBs propagating vertically. One can also see the AIAs marker layers in both the original epitaxial growth and the subsequent regrowth[30]. 53

Figure 3.9: A 60 μm grating top surface viewed through an optical microscope shows a) a lot of defects accumulating at the APBs for only 500 \AA of MEE, and b) a better quality film when 1000 \AA of MEE is used. An SEM close-up of the defects reveals that they are pits forming during the epitaxial regrowth..... 54

Figure 3.10: Optical microscope view of template top surface for a) 60 microns period, and b) 8 microns period. Defects tend to accumulate at the boundaries between the domains of different orientations, and the density of defects as well as the roughness of the surface visibly increases as the domain period is reduced. 54

Figure 4.1: Schematic describing the idea behind the growth of thick films on the orientation templates. We hope that the template can serve as a seed and that the epitaxial process used to grow the thick layers can let the domains grow vertically without closing..... 57

Figure 4.2: Orientation of the gratings on the template. All the QPM gratings were placed with their k vector in the [011] direction, since those in the other directions did not produce good quality films. 60

Figure 4.3: Signal/idler wavelength vs. QPM period for nonlinear interactions pumped at 1.064, 1.55 and 2.1 μm . The QPM period gets shorter with shorter pump wavelength. 60

Figure 4.4 shows complete cross-sections obtained by the method described above, for 1 cm long gratings with 60, 15.4 and 8.6 μm periods. The best results are obtained for the sample with a 60 μm period, shown in 4.4a. In this picture, we can see that most of the domains grow completely vertically throughout the film, with no change in duty cycle. Figure 4.5 is a close-up of the same cross-section, confirming that the domain boundaries do not have significant deviations from the vertical direction. . 61

Figure 4.5: Close-up of the stain-etched cross section of the QPM grating with 60 μm period. 63

Figure 4.6: Optical microscope pictures of the top of the samples with a) 15.4 and b) 8.6 μm periods. Some domains still propagate all the way to the top in a), while almost none make it in b). 64

Figure 4.7: Top view of the 60 μm period sample, showing both types of defects appearing on the HVPE grown thick films: single domain interruptions, and random pyramidal growths. 65

Figure 4.8: Morphologies of selective area growth with HVPE on stripes opened in a silicon nitride mask, using similar growth conditions to those used for our thick OP-GaAs films[59]. 66

Figure 4.9: The morphology of the surface of the thick OP-GaAs film can help understand the growth mechanism. a) shows a close-up optical microscope view of the top surface of the 60 μm period QPM grating, with clear evidence of two different types of surface behavior depending on the domain orientation. b) is an attempted explanation of the growth mechanism, where the growth rate is coupled in both domain orientation across the antiphase boundaries. 67

Figure 4.10: Top view of the sample for transmission measurements. The figure shows the 1.064 μm beam focused through the patterned region with a 26.3 μm period. We also used the unpatterned region next to it for comparison.	69
Figure 4.11: Experimental setup for SHG at 4 μm	72
Figure 4.12: Tuning curve for the 4 μm SHG obtained with a 1 cm long, 61.2 μm period grating. The circles are the experimental data, and the line is the theoretical tuning curve based on a well-known dispersion model[62].....	73
Figure 4.13: Comparison of the SHG phasematching wavelength between experiment and theory, based on Pikhtin[62], for three different grating periods.	74
Figure 4.14: SHG efficiency in the low conversion limit vs. pump intensity for OP-GaAs (L =1 cm) and PPLN (L = 6.2mm) at the phasematching wavelength of 4.135 μm , with fitted straight lines.	75
Figure 4.15: Difference-frequency mixing setup for generation of mid-IR radiation	77
Figure 4.16: Normalized tuning curve for the generation of mid-IR generation by difference-frequency mixing from a pump at 1307 nm and tunable signal around 1560 nm. The points indicate the experimental data, and the curve is a theoretical calculation whose peak has been shifted to match the measurement.	78
Figure 5.1: Configuration used in frequency converters for optical communication applications. a) shows how such a device could be used for channel shifting, where ω_s is the frequency for a WDM channel around 1550 nm, ω_{LO} is the pump frequency around 775 nm, and the output by difference-frequency mixing is ω_{out} , another WDM channel. b) shows that the difference-frequency mixing output field is the complex conjugate of the input one, which could be useful in dispersion compensation.	82
Figure 5.2: Schematic of the basic structure of our AlGaAs waveguides.	84
Figure 5.3: Basic ridge waveguide structure input into the waveguide mode solver	86
Figure 5.4: Index mesh generated by the mode solver.	86
Figure 5.5: Examples of mode profiles obtained with the mode solver from earlier tests.	86
Figure 5.6: Parameter analysis as function of width for an almost symmetrical waveguide with 1 μm core, for different core/cladding composition combinations.....	89

Figure 5.7: Parameter analysis as function of width for an almost symmetrical waveguide, for different values of the core thickness.....	90
Figure 5.8: Loss due to leakage in the substrate as a function of bottom cladding thickness.....	91
Figure 5.9: Δn_{eff} as a function of waveguide width for varying ridge height. As the core gets completely etched (2 μm deep in this case), the etch depth becomes noncritical. The values next to the h in the legend represent the etch depth in hundreds of nanometers.....	92
Figure 5.10: Δn_{eff} as a function of waveguide width for the same structure as in figure 5.9, with a 2 μm etch depth. Δn_{eff} does not have an optimum as a function of etch depth, so we just have to use the widest possible guides.....	93
Figure 5.11: Final waveguide structure, with the profile of the fundamental TE mode at 1550 nm.	94
Figure 5.12: SEM of ridges etched with the Plasmaquest ECR-RIE dry etching system, followed by a dip in a diffusion-limited etching solution. The close-up shows an 8 μm wide ridge, with very smooth sidewalls.	95
Figure 5.13: The end facets of a waveguide act as mirrors, thus creating a Fabry-Perot cavity. The transmission then shows peaks and valleys.	96
Figure 5.14: Measurement of losses for samples processed with varying parameters, showing that we have been able to fabricate unpatterned waveguides with loss as low as 3-4 dB/cm.	96
Figure 5.15: Attenuation from corrugated core/cladding interface calculated using coupled-mode theory for a planar waveguide with 1500 \AA corrugation at both fundamental and second harmonic wavelengths.....	98
Figure 5.16: Waveguide SHG setup	99
Figure 5.17: Tuning curves for 4 mm long, 8 μm wide waveguides, with QPM periods of 4.7 and 4.8 μm , overlayed with theoretical calculations.	101
Figure 5.18: Tuning curves of three waveguides located side by side for two different QPM periods, to verify the local homogeneity of the samples.....	102

CHAPTER 1: INTRODUCTION

This dissertation describes the investigation, fabrication and testing of orientation-patterned-GaAs-based nonlinear optical frequency conversion devices. It thus provides a combination of semiconductor physics, material science, and nonlinear optics. In the chapters to follow, I will go into more details in the various parts of this research. This chapter serves as an introduction to the motivations behind this work, and a short description of the organization of the text.

1.1 Motivations

Since the discovery of the laser, many applications for it have flourished. This has sparked a whole sector of scientific research dedicated to discovering new materials or engineering new devices from existing technologies to reach new areas of the electromagnetic spectrum with coherent sources. However, there often do not exist materials with the required properties to make a laser in the region of interest, or the existing materials can not provide the end user with desired features, such as ease of use, portability and low cost.

For these reasons, nonlinear optical frequency conversion has slowly grown into an established way to generate wavelengths of interest. A large part of nonlinear optics research is to look for materials with useful properties, such as a large nonlinear coefficient (of second or third order in most cases). Over the years, many such materials have been studied and successfully used in various applications[1].

In this work, we will focus our interest on the near to mid-infrared region of the optical spectrum. We will explore the properties of AlGaAs as a nonlinear optical material, and describe the technique we developed to fabricate frequency conversion devices using it.

1.2 Infrared optics applications

For the purpose of this dissertation, we will limit ourselves to the $1\mu\text{m}$ to $12\mu\text{m}$ region of the optical spectrum. Why the interest in this region? For the near infrared, between $1\mu\text{m}$ and $2\mu\text{m}$, the largest current application is optical communication through fiber links. Most current installed fibers have an absorption minimum around $1.55\mu\text{m}$, and a dispersion minimum around $1.3\mu\text{m}$. Current trends focus on increasing the number of channels per fiber[2], and dynamically controlling wavelength allocations. One can imagine that all-optical frequency conversion devices would prove very useful as building blocks of future communication networks.

In the mid infrared region ($2\mu\text{m}$ to $12\mu\text{m}$), a variety of applications exist. Many molecules such as atmospheric pollutants and biological compounds have signature absorption bands in this wavelength region. A coherent source tuned to one of these lines provides a very sensitive detection and concentration monitoring system. One can think of checking automobile pollution from exhaust pipes or monitoring industrial side-products. Medical applications, such as measuring blood sugar levels or tissue ablation are another possibility[3].

Furthermore, there are also some military applications, such as laser remote sensing systems (laser radar), and airborne countermeasure systems designed to protect aircraft from heat-seeking missiles by scrambling them with fake information. Both of these applications, as well as spectroscopy remote monitoring, can take advantage of the low-loss atmospheric windows from $3\mu\text{m}$ to $5\mu\text{m}$ and $8\mu\text{m}$ to $12\mu\text{m}$.

Depending on the application, the desirable features can vary. Spectroscopy applications typically require narrow linewidth but low average power sources, while high power sources are more suited to the military systems described above. In the next section, we describe currently available coherent sources in the infrared region. Keeping in mind the desirable characteristics mentioned above, we will demonstrate the usefulness of frequency-conversion-based sources for applications of interest.

1.3 Current infrared sources

In the near infrared, solid-state lasers clearly dominate. 1.064 μm lasers have seen a huge amount of development, and are now produced in large quantities, with a wide variety of beam, pulse and power properties. Semiconductor diode lasers cover most of this region as well. They have proven to be highly efficient, very small, long-lived and low-cost, and have found many applications, from optical storage to optical communications[4]. GaAs-based lasers usually operate in the 600nm to 1 μm range, although recent developments are extending GaAs lattice-matched materials to the 1.3 μm and 1.55 μm ranges[5]. Traditionally, communication lasers have been developed with InP substrates and lattice-matched materials[4]. Reaching longer wavelengths with III-V semiconductor lasers using electron/hole recombination becomes difficult because as the band gap gets smaller, thermal effects and non-radiative processes such as Auger recombination limit their performance[6]. As another alternative, lead-salt lasers, despite lower Auger recombination rates, still require cryogenic cooling and produce poor power levels[7]. The need for cooling makes these sources more difficult to package and unattractive for deployment in the field.

An alternative to bipolar semiconductor lasers is the quantum cascade laser[8], which is based on intersubband transitions inside of specially engineered coupled quantum wells. Previously, quantum cascade lasers required cryogenic cooling to operate, but recent improvements have brought their operating temperature to more easily attainable levels[9], and they now cover a large part of the mid to far infrared spectrum[10]. However, quantum cascade lasers are still at a very early experimental stage, and their limitations have to be established, in particular in the areas of tuning range and peak and average powers. For this reason, it is uncertain if they can become a viable mid-infrared laser solution.

Besides semiconductor lasers, there are also other types of lasers available. Some gas lasers with transitions in the infrared spectrum are also available, such as HeNe at 3.39 μm , and CO₂ between 9.2 and 10.8 μm , and they are capable of outputting large powers. These lasers, however, are usually very large, relatively inefficient, fragile, and lack sufficient tunability. This limits their usage outside of a lab for the applications described above.

1.4 Nonlinear optics for infrared applications

As seen in the previous section, current laser sources in the region of interest usually lack one or more of the required features for the applications considered. While undoubtedly technological advances will help solve some of the problems raised above, an attractive alternative has emerged in the meantime: generation of coherent radiation by nonlinear optical frequency mixing.

Some materials, submitted to intense light beams, exhibit nonlinear terms in the induced polarization. In general, terms of second or third order can appear, depending on the symmetry of the material studied[1]. This nonlinear polarization in turn radiates a field at a frequency depending on the fields inducing it. Figure 1.1 shows two of the most common examples of second order nonlinear optical interactions, second harmonic generation (SHG), and difference frequency generation (DFG). In SHG, the intense field from a source induces a polarization radiating a twice the frequency, called the second harmonic. In DFG, an intense pump beam at frequency ω_3 and a signal beam at frequency ω_1 combine to generate a third frequency, called the idler, at $\omega_2 = \omega_3 - \omega_1$. For instance, DFG using two near-infrared lasers at 1.064 and 1.3 μm respectively would generate an idler beam at 5.86 μm .

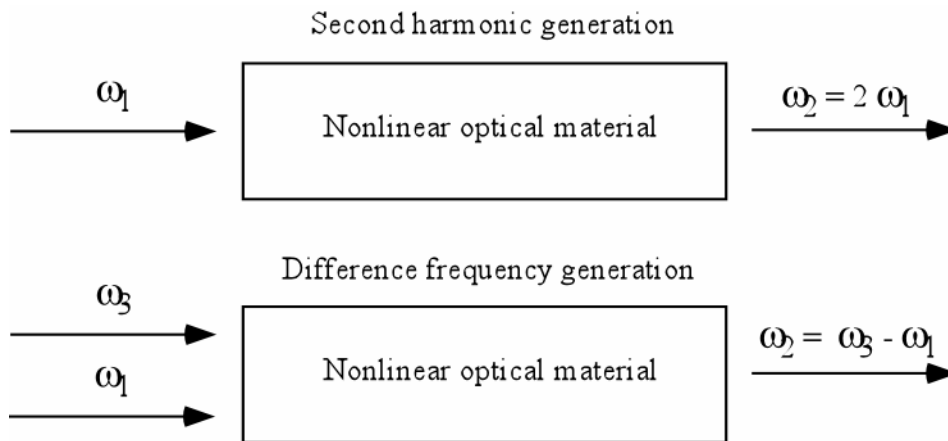


Figure 1.1: Schematic of two common types of nonlinear optical interactions.

Another important variation on the DFG scheme is to put the nonlinear optical material in a cavity that is resonant for at least one of the wavelengths present, and build what is called an optical parametric oscillator (OPO). The nonlinear optical material acts

as a gain medium for signal, idler, or both, when pumped with an intense pump beam. In addition, in the DFG/OPO scheme, a small change in the pump or signal wavelength can result in a large change of the corresponding idler wavelength. Taking advantage of the plethora of near-infrared semiconductor and diode-pumped lasers available, with a wide variety of spectral properties, pulse formats, and output powers, one can think of fabricating a widely tunable infrared source with equally as good output properties. Considering the size of current solid-state and semiconductor lasers, a mid-infrared source based on a DFG or OPO scheme could easily become portable and thus very useful for the spectroscopy and military applications described above, for instance. A description of existing mid-infrared sources based on these techniques can be readily found in the literature[11-13].

For optical communication applications, a DFG device could be used to all-optically shift data from one WDM channel to another: mixing wavelength at $1.55-\Delta \mu\text{m}$ with a pump at 775 nm would result in an output at $1.55+\Delta \mu\text{m}$. By tuning the pump wavelength, such a device could convert any WDM wavelength into any other one. Additionally, it could also convert multiple channels simultaneously in a “broadcast” configuration. Finally, such devices can also be used as mid-span spectral inverters to correct for accumulated dispersion. Most of these applications have been demonstrated in LiNbO_3 waveguide devices[14-17].

1.5 Infrared nonlinear optical materials

As mentioned earlier, a large part of the activity in the field of nonlinear optics is the search for materials suitable for the various applications envisaged. Accordingly, a few materials have emerged as choice candidates for different regions of the infrared. For instance, periodically-poled lithium niobate (PPLN) has seen widespread use in many applications, from generation of blue-green light at 532 nm (using SHG pumped with a 1.064 μm laser)[18], to mid-IR generation[11,12,19], to the communication devices described above[14-17]. However, LiNbO_3 is not transparent beyond 5 μm , which is the main reason why other materials have to be used to reach the rest of the mid-infrared spectrum.

The most common crystals for mid-infrared frequency conversion are the chalcopyrite family, including ZnGeP_2 , AgGaSe_2 , AgGaS_2 , and CdGeAs_2 . These are usually available in bulk-like shape, with centimeter dimensions. Frequency conversion in these materials has already been successfully demonstrated. ZnGeP_2 , for instance, has been used to build widely tunable OPOs covering the region from over 3 to 12 μm , despite needing pump lasers with wavelength longer than 2 μm , and phonon-related absorption at long wavelength above 9 μm [20-22]. Unfortunately, the chalcopyrite family suffers from extrinsic problems, such as point defects generating excess absorption, or difficulties in growing large high-quality crystals.

Taking into account all of these factors, it becomes obviously important to look for alternatives, with improved intrinsic properties such as higher nonlinear coefficients, or better growth/fabrication techniques. The properties that limit the usefulness of a given material tend to be simple and limited: absorption, thermal conductivity, noncritical phasematching, and scalable growth. Therefore, in developing new materials, we favor those that have such favorable intrinsic properties, and additionally, we would also prefer them to be systematically engineerable for the applications of interest. This explains the success of PPLN, due to the possibility of building into the material the desired properties for a given application. The goal of the work described in this dissertation is admittedly to try and develop a new nonlinear optical material that would essentially extend the properties of PPLN into the mid-infrared region, thus allowing more flexibility than that offered by the chalcopyrites.

Zincblende semiconductors offer many very attractive properties such as large nonlinear coefficients and a wide transparency range. In addition, they have other useful material properties such as high thermal conductivity, important for high power applications, and they also benefit from high quality, high purity crystals, advanced fabrication techniques, and the possibility to be integrated with semiconductor lasers of the same materials. To emphasize the attractiveness of zincblende semiconductors, table 1.1 shows a comparison of two zincblende semiconductors, GaAs and ZnSe, with representatives of the chalcopyrite family, as well as PPLN.

	GaAs	ZnSe	ZnGeP₂	AgGaSe₂	LiNbO₃
Effective Nonlinear coefficient (pm/V)	57	38	70	33	17
Useful range (μm)	1-12	0.5-20	2-13	0.5-15	0.4-4.5
Thermal conductivity (W/m.K)	52	18	35	1	5.6
Phasematching type	QPM	QPM	Birefringent	Birefringent	QPM

Table 1.1: Properties of some nonlinear materials

As is visible in this table, both ZnSe and GaAs have major advantages over the current materials of choice. For instance, GaAs and ZnSe both offer transparency in the mid-IR and larger effective nonlinear coefficients than PPLN. Historically, though, GaAs and ZnSe were not used for nonlinear optics, due to their lack of birefringence which was necessary to obtain efficient frequency conversion. However, in recent years, much effort has been devoted to trying to make these materials useful.

1.6 Nonlinear optics in semiconductors

To take full advantage of zincblende semiconductors, a way to achieve efficient nonlinear conversion has to be developed, which has been the roadblock over which all these efforts have stumbled. Recent developments have slowly pointed the way towards our current implementation. In GaAs, two different approaches have been used to achieve efficient conversion.

The first one relies on a technique called form birefringence, which introduces artificial birefringence by using periodic structures of GaAs/Aluminum oxide[23]. The TE and TM modes see different boundary conditions which lead to different indices of refraction. Unfortunately, this technique is limited to thin films, is technically challenging

due in particular to the oxidation step, and the final structures are mechanically unstable because of the Aluminum oxide. Even so, some good results have been obtained with this approach[24,25].

The other way to tackle the problem is to implement a quasi-phasematching (QPM) scheme, which relies on a periodic modulation of the nonlinear coefficient. This is the technique used in PPLN. Following the success of PPLN, QPM in semiconductors has become very sought-after technology. Figure 1.2 illustrates what kind of structure one would like to achieve for QPM in GaAs. The length L_c is called the coherence length and depends on the interaction of interest, but will ideally have to be as short as a few microns in GaAs for laser pumps at around $1\ \mu\text{m}$ (see chapter 2 for more details).

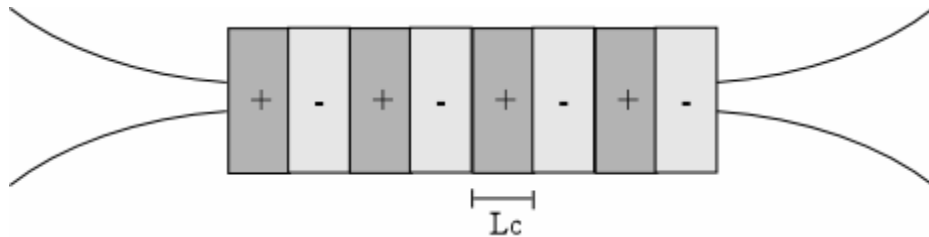


Figure 1.2: Typical quasi-phasematched device for frequency conversion. The + and – signs indicate the modulation of the sign of the nonlinear coefficient for maximum conversion efficiency. L_c is called the coherence length and is determined by the nonlinear interaction of interest.

The first method used to achieve QPM in GaAs was to use a bonded stack of plates with the right nonlinear coefficient modulation[26,27]. While this approach was somewhat successful, in particular due to the fact that it allows large apertures for high power handling, it remains of limited usefulness because of the highly serial process needed to fabricate these devices. In particular, one needs to thin down the GaAs plates to a small multiple of the coherence length, which makes it very difficult for coherence lengths on the order of microns. Additionally, even if one manages to get very thin plates, many of them would have to be stacked to get any reasonable useful length for high conversion efficiency.

The other approach for QPM in GaAs is to fabricate an orientation template, and use it as a seed to grow the desired structure, as shown in figure 1.3. This has mostly one great advantage over the stack of plate approach: the QPM pattern is defined

lithographically, thus allowing for much shorter QPM periods than in the stacks. This was first realized by using a similar bonding technique to the one described above, but using only two GaAs plates, and etching the QPM pattern so as to expose areas of both nonlinear coefficient signs. The template was then put into an epitaxial growth system and the desired structure was regrown. This led in particular to the demonstration of frequency conversion in waveguide devices[28]. Unfortunately, this approach is limited by the large corrugations in the template that lead to substantial propagation loss in the devices grown on the templates.

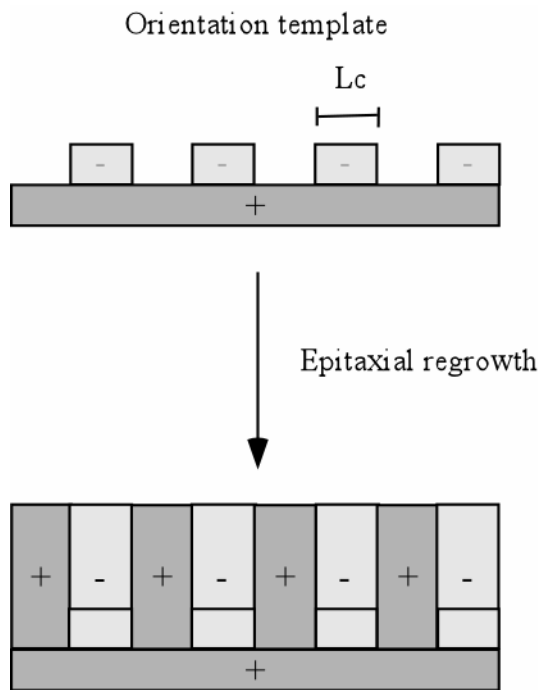


Figure 1.3: Orientation template for epitaxial growth of QPM structures. The template can be obtained either by bonding two semiconductor plates, or by the all-epitaxial fabrication technique used in this work.

Despite these issues, the orientation template idea still appears as the most promising idea, given the fact that it also allows for more complex devices, such as angled or chirped gratings, and wafer-scale processing. The idea of an all-epitaxial fabrication process then started to appear, because presumably one could keep the corrugations to much smaller sizes, or even make zero-corrugation templates. The first attempt at all-epitaxial fabrication process was done by Angell et al., in II-VI materials,

using CdTe seed layers and ZnTe/ZnSe waveguide layers[29]. The QPM modulation was only an on/off modulation rather than a sign modulation and the devices had very high propagation losses.

This work represents the state-of-the-art in terms of all-epitaxial fabrication of orientation-patterned GaAs templates and QPM devices based on them. The techniques used were independently invented at Stanford University[30,46,47], and in a Japanese group at the University of Tokyo[31,32]. Both use polar-on-nonpolar epitaxy of GaAs on Ge, or GaAs on Si to achieve the sign reversal of the nonlinear coefficient.

1.7 Organization

This dissertation is organized as follows. Chapter 2 presents the theory of nonlinear frequency conversion in both bulk material and waveguides. Chapter 3 reviews previous results on the development and fabrication of GaAs-based nonlinear optical devices, as well as describes the state-of-the-art in the fabrication process at the time of writing of this dissertation. Based on this knowledge, chapter 4 details the results of the growth and characterization of thick orientation-patterned GaAs films by hydride vapor phase epitaxy, and describes various very successful nonlinear optical experiments accomplished with samples of the thick films. Chapter 5 reports waveguide device fabrication as well as optical results of frequency conversion in these waveguides. Finally, chapter 6 concludes and offers some potential directions for future research.

CHAPTER 2: THEORY OF NONLINEAR FREQUENCY CONVERSION

In this chapter, we present the theoretical background necessary to understand the results presented in the rest of this dissertation. We focus on second-order nonlinear interactions, which are the types of interactions we are using for frequency conversion in GaAs-based devices. The theory of nonlinear optics has already been well-covered in the literature[1,33], so I will only include the basic foundations which are all that are needed to understand this dissertation. I will emphasize particular points of interest and relevance to GaAs-based devices.

This chapter begins with a brief explanation of the physics of nonlinear optics, introducing the nonlinear polarization, followed by presentation of the theory of frequency conversion using plane waves and coupled-wave equations. This simple description helps introduce the important concepts of frequency conversion, such as conversion efficiency and phasematching. We follow this by expanding the theory into two distinct parts: waveguide nonlinear optics, and gaussian beams interacting in bulk material.

2.1 Physics of nonlinear optics

A linear dielectric medium is characterized by the linear relationship between the polarization and the electric field applied to the medium:

$$P = \epsilon_0 \cdot \chi \cdot E \tag{2.1}$$

where ϵ_0 is the permittivity of free space, and χ is the dielectric susceptibility. Until the invention of the laser and the associated intense electric fields, all media were considered to have the linear response of equation 2.1. However, nonlinear effects started appearing with the use of laser radiation, such as frequency doubling[34] and intensity-dependent refractive indices. The optical nonlinearity of a dielectric medium translates into a

nonlinear relationship between the polarization induced in the material and the electric field applied, as shown in figure 2.1.

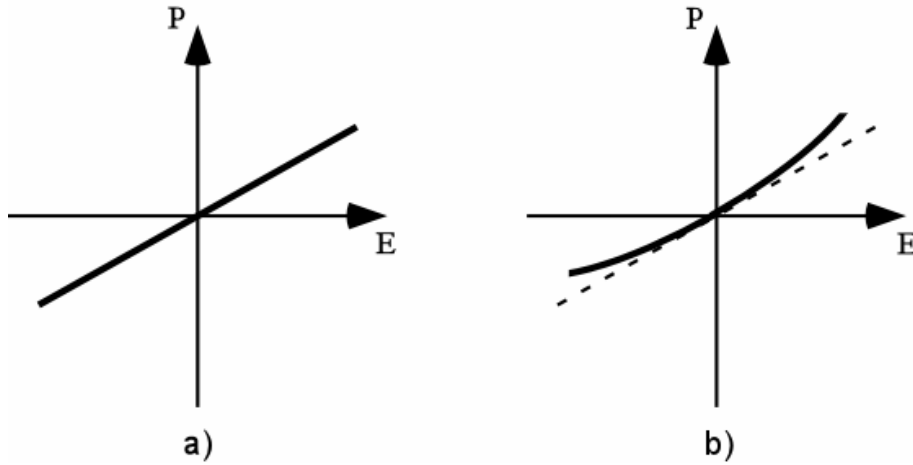


Figure 2.1: The relationship between polarization and applied electric field for (a) a linear dielectric medium, and (b) a nonlinear dielectric medium.

Typically, when the applied electric field is small, the relationship between P and E can be assumed to be linear, but when E approaches interatomic electric field values, typically 1 kV/cm, then the relationship becomes highly nonlinear. We can use the Lorentz model of atoms in a medium as a collection of oscillators to understand this. When an electric field is applied, electrons vibrate in response to the field, thus creating electric dipoles $p = -e \cdot r$, where r is the displacement of individual electrons to which the force $-e \cdot E$ is applied. The polarization in the material is then $P = Np$, where N is the number of dipoles in the material. In a linear material, the restoring force of the atomic potential obeys Hooke's law and thus the equilibrium displacement is proportional to the applied field, giving p proportional to E . However, the atomic parabolic potential is an approximation that breaks down with strong applied fields, giving a restoring force that contains higher orders of the displacement. The result is that the equilibrium displacement, and thus the polarization, is a nonlinear function of E .

It is customary to write the polarization as:

$$P = \epsilon_0 \cdot (\chi^{(1)} E + \chi^{(2)} E^2 + \chi^{(3)} E^3 + \dots) \quad (2.2)$$

where the first term is the usual linear polarization, and the higher order terms are called the nonlinear polarization, written:

$$P_{NL} = \varepsilon_0 (\chi^{(2)} E^2 + \chi^{(3)} E^3 + \dots) \quad (2.3)$$

This equation is the basis for all the theory that follows. The higher order terms of the nonlinear polarization must radiate electromagnetic radiation, thus resulting in fields at different frequencies from the ones incident on the medium. Controlling these effects is the essential goal of nonlinear optical experiments, to be able to generate desired frequencies from available sources.

2.2 Nonlinear interactions of plane waves

A plane wave propagating in a dielectric isotropic medium follows the wave equation which can be derived from Maxwell's equations:

$$\nabla^2 E - \frac{1}{c_0^2} \frac{\partial^2 E}{\partial t^2} = \mu_0 \frac{\partial^2 P}{\partial t^2} \quad (2.4)$$

where c_0 is the speed of light in vacuum. Using equation 2.3, splitting the polarization between linear and nonlinear parts, and using c as the speed of light in the medium, we obtain the nonlinear wave equation:

$$\nabla^2 E - \frac{1}{c^2} \frac{\partial^2 E}{\partial t^2} = \mu_0 \frac{\partial^2 P_{NL}}{\partial t^2} \quad (2.5)$$

This is a nonlinear partial differential equation in E , where the right hand term acts as a radiation source in a linear medium. We are going to use the coupled-wave approach to solve for the various fields propagating through the medium.

For simplicity, we will take the example of three wave-mixing, which is the most important case that we are interested in for this work. Let's assume that the field E is a superposition of three fields of frequencies $\omega_1, \omega_2, \omega_3$ propagating along the z direction.

$$\begin{aligned} E(z,t) &= \sum_{n=1,2,3} E_n(z) e^{i\omega_n t} + c.c. \\ E(z,t) &= \sum_{p=\pm 1, \pm 2, \pm 3} E_p(z) e^{i\omega_p t} \end{aligned} \quad (2.6)$$

where $E_n(z) = A_n e^{-ik_n z}$ is the complex amplitude of the field as it propagates through the material, and $k_n = \omega_n/c$. The second equation is a convenient way to write the E field, where $E_{-p} = E_p^*$, and $\omega_{-p} = -\omega_p$.

The nonlinear polarization, used as a radiation source, is written as:

$$P_{NL} = 2\varepsilon_0 d_{eff} E^2 \quad (2.7)$$

where d_{eff} is called the effective nonlinear coefficient, and is commonly used in place of $\chi^{(2)}$ for simplicity in writing equations for three-wave mixing.

The resulting nonlinear polarization obtained is a sum of all the cross-product terms:

$$P_{NL} = \frac{1}{2} \varepsilon_0 d_{eff} \sum_{n,p=\pm 1, \pm 2, \pm 3} E_n E_p e^{i(\omega_n + \omega_p)t} \quad (2.8)$$

giving a series of different frequency components. Substituting equations 2.6, 2.7 and 2.8 into the nonlinear wave equation 2.5, we obtain a single differential equation with all these frequency components. If $\omega_1, \omega_2, \omega_3$ are distinct, then we can write three separate equations for the evolution of the electric field associated with them, called Helmholtz equations with sources:

$$\begin{aligned}
(\nabla^2 + k_1^2)E_1 &= -S_1 \\
(\nabla^2 + k_2^2)E_2 &= -S_2 \\
(\nabla^2 + k_3^2)E_3 &= -S_3
\end{aligned} \tag{2.9}$$

The source terms can be calculated easily from the nonlinear polarization. In particular cases of interest, where the frequencies are related, such as $\omega_3 = \omega_1 + \omega_2$, then the source term for one of the equations is related to the electric fields at the other two frequencies, thus coupling the three waves. This is the origin of the term ‘‘coupled-wave’’ equations. Continuing with the example $\omega_3 = \omega_1 + \omega_2$, we obtain the following three-wave mixing coupled equations:

$$\begin{aligned}
(\nabla^2 + k_1^2)E_1 &= -2\mu_0\omega_1^2\varepsilon_0d_{eff}E_3E_2^* \\
(\nabla^2 + k_2^2)E_2 &= -2\mu_0\omega_2^2\varepsilon_0d_{eff}E_3E_1^* \\
(\nabla^2 + k_3^2)E_3 &= -2\mu_0\omega_3^2\varepsilon_0d_{eff}E_1E_2
\end{aligned} \tag{2.10}$$

Before proceeding, it is convenient for us to normalize the complex envelopes of the plane waves by defining the variables $a_p = A_p/(2\hbar\omega_p/\varepsilon_0c_0n_p)^{1/2}$, with n_p the refractive index of the material at frequency ω_p . Thus we get:

$$E_p(z) = \left(\frac{2\hbar\omega_n}{\varepsilon_0c_0n_p}\right)^{1/2} a_p e^{-ik_p z} \tag{2.11}$$

and we can instantly write the intensities of the waves as $I_p = \hbar\omega_p|a_p|^2$, clearly showing that $|a_p|^2$ equals the flux of photons at frequency ω_p . So it is doubly convenient to adopt this notation, since the frequency mixing process must exhibit photon conservation.

We can then derive the equations describing the evolution of the envelopes, a_n , of the fields as they propagate along z with the above assumptions. To write these down, we assume that the coupling between the waves is weak (since this is a second order effect). Following this, we can safely claim that the variation of the amplitudes with distance is slow, and that they can be taken as approximately constant over the length of a

wavelength. This is called the slowly-varying envelope approximation, and results in being able to neglect the second order derivative terms.

The three-wave mixing coupled equations then become:

$$\begin{aligned}\frac{da_1}{dz} &= -iga_3a_2^*e^{-i\Delta k.z} \\ \frac{da_2}{dz} &= -iga_3a_1^*e^{-i\Delta k.z} \\ \frac{da_3}{dz} &= -iga_1a_2e^{i\Delta k.z}\end{aligned}\tag{2.12}$$

where

$$g = \left(\frac{2\hbar\omega_1\omega_2\omega_3d_{eff}^2}{n_1n_2n_3\epsilon_0c_0^3}\right)^{1/2}\tag{2.13}$$

and

$$\Delta k = k_3 - (k_1 + k_2)\tag{2.14}$$

Δk is called the phase vector mismatch and represents the error in the phase-matching condition. From these equations, we can calculate the evolution of the amplitudes with propagation distance in the nonlinear medium for various interactions of interest.

2.3 Conversion efficiency and phasematching conditions

The three-wave mixing equations derived in section 2.2 are our starting point to determine the efficiency of a particular nonlinear optical interaction. For simplicity, we will go over the equations for the case of second-harmonic generation, and in the end, we will extend this to another simple case, difference frequency generation.

Second-harmonic generation is a degenerate case of three-wave mixing where

$$\omega_1 = \omega_2 = \omega \quad \text{and} \quad \omega_3 = \omega_1 + \omega_2 = 2\omega$$

Two interactions, described by the two coupled-wave equations obtained from equations 2.12, compete:

- One photon at frequency 2ω splits into two photons at frequency ω .
- Two photons of frequency ω add up to form a photon at frequency 2ω .

$$\begin{aligned} \frac{da_1}{dz} &= -iga_3 a_1^* e^{-i\Delta k \cdot z} \\ \frac{da_3}{dz} &= -i \frac{g}{2} a_1^2 e^{i\Delta k \cdot z} \\ g &= \left(\frac{4\hbar\omega^3 d_{eff}^2}{n_1^2 n_3 \epsilon_0 c_0^3} \right)^{1/2} \\ \Delta k &= k_3 - 2k_1 \end{aligned} \tag{2.15}$$

These equations can be integrated, using appropriate boundary conditions such as $a_3(0) = 0$, to get the evolution of the amplitudes along z . Assuming perfect phasematching, $\Delta k = 0$, and conservation of photon numbers $|a_1(z)|^2 + 2|a_3(z)|^2 = \text{constant}$, it is easy to get

$$\begin{aligned} a_1(z) &= a_1(0) \operatorname{sech} \frac{ga_1(0)z}{\sqrt{2}} \\ a_3(z) &= -\frac{i}{\sqrt{2}} a_1(0) \tanh \frac{ga_1(0)z}{\sqrt{2}} \end{aligned} \tag{2.16}$$

We then write the conversion efficiency of the second-harmonic generation as:

$$\begin{aligned} \frac{I_3(L)}{I_1(0)} &= \tanh^2 \left(\frac{\gamma L}{2} \right) \\ \gamma &= \frac{2ga_1(0)}{\sqrt{2}} \end{aligned} \tag{2.17}$$

For large γL (long device, large input intensity, large nonlinear coupling), this efficiency can approach one, meaning that all the input power has been converted into power at the second harmonic. For small γL (short devices or smaller intensities and nonlinear coefficients), the argument of the tanh function is small and thus we can approximate it with $\tanh x \sim x$. The efficiency then becomes

$$\frac{I_3(L)}{I_1(0)} = \frac{2\omega^2 d_{eff}^2}{n_1^2 n_3 \epsilon_0 c_0^3} L^2 I_1(0) = \frac{8\pi^2 d_{eff}^2}{n_1^2 n_3 \epsilon_0 c_0 \lambda^2} L^2 I_1(0) \quad (2.18)$$

It is more common to write this in terms of power, using $P_n = I_n A_n$, where A_n is the input area. The efficiency can then be written:

$$P_3 = \eta L^2 P_1^2$$

$$\eta = \frac{2\omega^2 d_{eff}^2}{n_1^2 n_3 \epsilon_0 c_0^3 A_{eff}} = \frac{8\pi^2 d_{eff}^2}{n_1^2 n_3 \epsilon_0 c_0 \lambda^2 A_{eff}} \quad (2.19)$$

where η is called the normalized conversion efficiency and has units of $1/(\text{W}\cdot\text{cm}^2)$, and A_{eff} has units of area, and depends on the geometry of the interaction.

For a perfectly phasematched interaction, in the low conversion limit, the conversion efficiency increases quadratically with length and linearly with input power. It is easy to see that to maximize efficiency, one must obtain the longest possible interaction length, L , while minimizing the area, A_{eff} . We will see that this is best accomplished in waveguide devices, which can produce some of the highest conversion efficiencies. However, the waveguide configuration is not always optimal for the application of interest. We will go into further detail in waveguides and bulk configurations later in this chapter. Another point to notice from this is that d^2/n^3 emerges as a good figure of merit to compare various materials for efficient frequency conversion.

The derivations made above assumed the condition called perfect phasematching, where $\Delta k = 0$. In general, if no particular care is taken, this condition is not automatically

fulfilled. To study the effect of phase mismatch, let us for simplicity consider the low conversion case only, where we can assume the amplitude of the fundamental beam to remain approximately constant throughout the material. In this approximation, we can easily derive the amplitude of the second harmonic and the conversion efficiency is then given by

$$P_3 = \eta \operatorname{sinc}^2\left(\frac{\Delta k L}{2}\right) L^2 P_1^2 \quad (2.20)$$

where $\operatorname{sinc}(x) = \sin(x)/x$.

It becomes obvious that the effect of phase mismatch is to reduce the efficiency of the interaction by the sinc^2 factor. When the mismatch $\Delta k = 0$, as we saw above, this factor is one, and the power keeps growing quadratically. However, when $\Delta k \neq 0$, then the sinc^2 factor is smaller than one, sometimes much smaller. Figure 2.2 shows the tuning curve obtained as a function of phase mismatch. The width of the curve is inversely proportional to the length of the material, making the phasematching condition increasingly narrow with length. When $\Delta k \neq 0$, the length $L_c = 2\pi / \Delta k$, called the coherence length, is the maximum length over which the nonlinear interaction is efficient

Because virtually all materials exhibit dispersion of the refractive index, it is rare to obtain accidentally perfect phasematching, which in the case of second harmonic generation simplifies to $n_1 = n_3$. So in general, Δk is not 0, and the conversion efficiency is very small. It's not hard then to understand that most of the work in the field of experimental nonlinear optics has historically been to try and achieve some kind of phasematching to obtain high conversion efficiencies. Figure 2.3 illustrates both perfectly phasematched and unphasematched cases, as well as a third possibility, which is called quasi-phasematched, which we will cover further in this section.

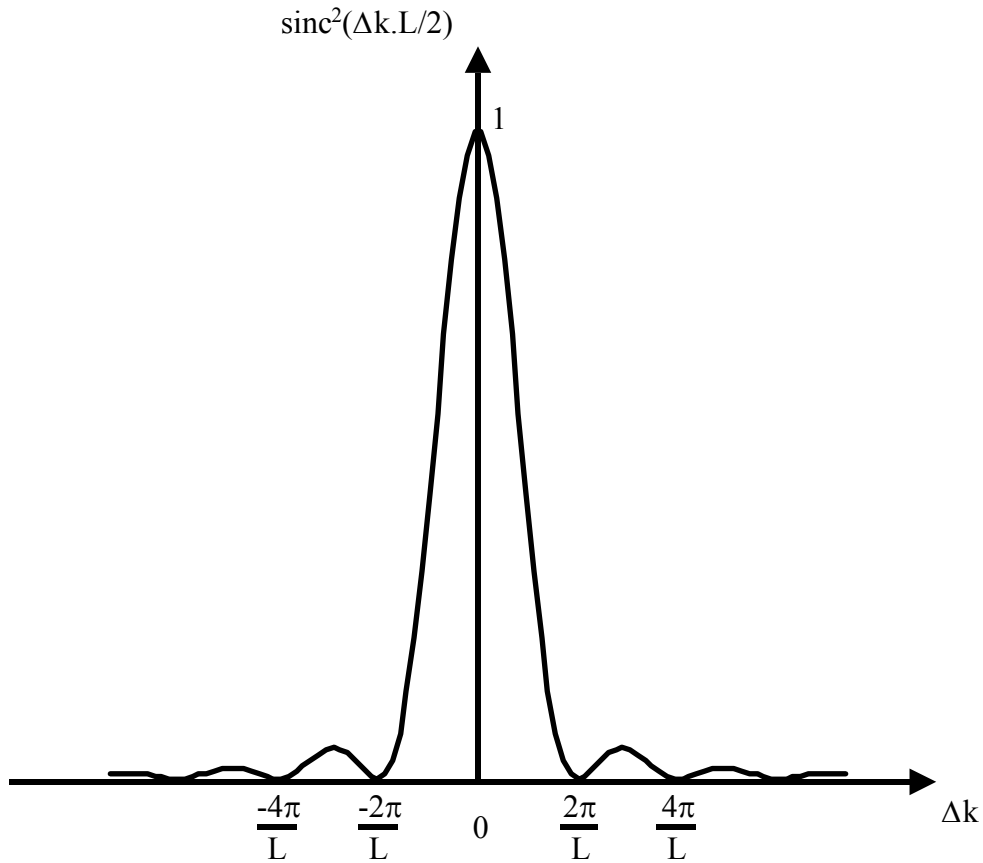


Figure 2.2: Tuning curve obtained from the sinc^2 term as a function of dephasing from the optimal phasematching condition.

When the interaction is not phasematched, power flows into the second harmonic along a length of size L_c , then flows back into the fundamental in the next section of length L_c , continuing to alternate similarly during the rest of the length of material. For this reason, no length of material longer than L_c is useful for conversion. In the case of perfect phasematching, the second harmonic power increases quadratically with length, at least in the undepleted pump, or low conversion, regime.

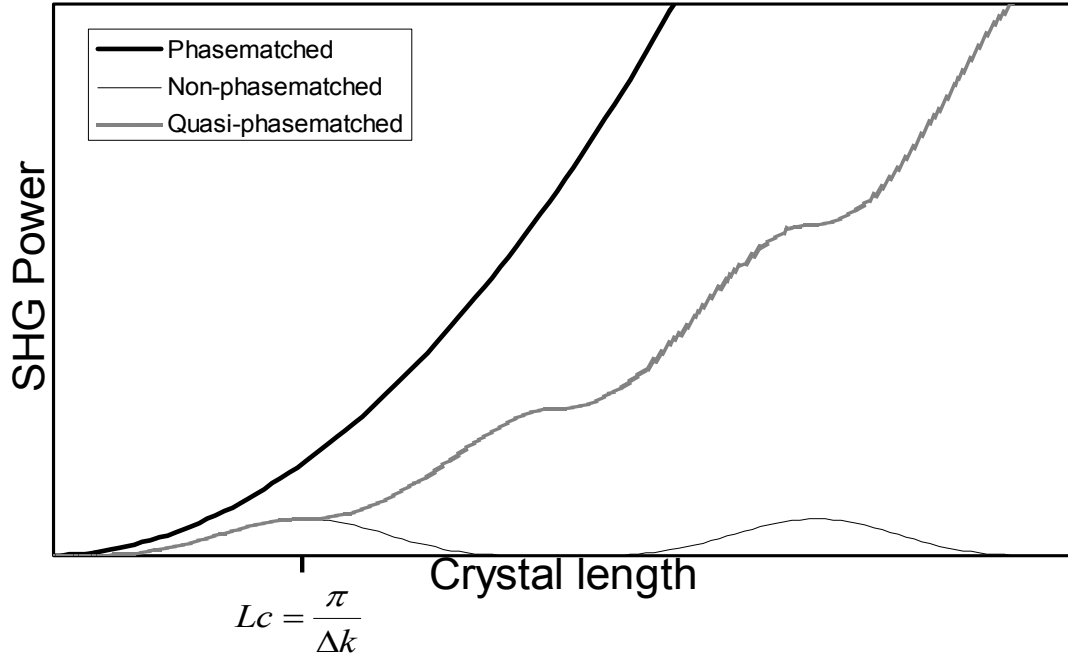


Figure 2.3: SHG power vs. material length for three different phasematching conditions. Quasi-phasematching (QPM) results in quasi-quadratic increase of SHG power with distance, with the effective nonlinear coefficient reduced by $2/\pi$.

Historically, perfect phasematching has been obtained by using the birefringence of nonlinear materials to fulfill the phasematching condition[35]. For instance, for second harmonic generation, the fundamental and second harmonic are made to propagate with different polarization directions, thus with different indices of refraction. In certain cases, such as that illustrated in figure 2.4, the indices for both frequencies match exactly, giving perfect phasematching. While we have ignored polarizations in the theory described so far, it is useful to note at this point that nonlinear coefficients only couple certain field directions depending on the symmetry of the material, and that birefringent phasematching can occur only under these constraints.

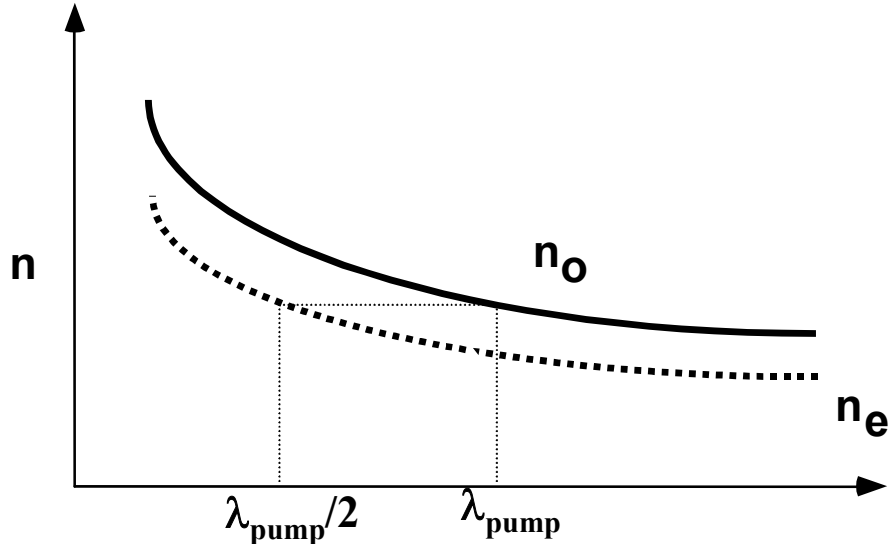


Figure 2.4: Birefringent phasematching in a negative uniaxial material, with fundamental propagating with ordinary index, and second harmonic with extraordinary index.

Unfortunately, birefringent phasematching has many disadvantages. Spatial overlap walk-off can happen when the Poynting vector and the k vector are not collinear, which limits the efficiency of the interaction. Additionally, birefringent phasematching is generally limited to a narrow range of frequencies, thus reducing its usefulness.

The idea of quasi-phasematching was first proposed in 1962[36]. Looking back at the not-phasematched case, it became apparent that if one can somehow reset the phase relationship between the propagating second harmonic wave and the nonlinear polarization generated by the fundamental every coherence length, second harmonic power could continue to build in a semi-quadratic fashion instead of flowing back into the fundamental. After a coherence length of propagation, the phase-mismatch, expressed as $\Delta k \cdot L/2$, is exactly π . If one can bring it back to zero, then we can achieve the phase reset we want. The proposed idea is to flip the sign of the nonlinear coupling coefficient every coherence length, or at least every odd multiple of the coherence length, effectively realizing the π phase-shift needed. Figure 2.5 shows a schematic of a typical QPM device, where the sign of the nonlinear coefficient has been flipped every coherence length.

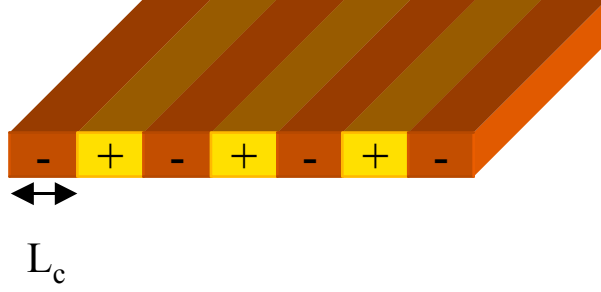


Figure 2.5: A typical QPM bulk device, where the fields propagate through sections of alternating signs for the nonlinear coefficient.

Mathematically, if the sign of the nonlinear coefficient is modulated periodically, we can write the nonlinear coefficient as a function of position in the material:

$$d(z) = d_{eff} \sum_{m=-\infty}^{+\infty} D_m e^{-iK_m z} \quad (2.21)$$

where the grating vector is defined as $K_m = 2\pi m/\Lambda$, and Λ is the period of the modulation. The amplitude of the m th Fourier coefficient is

$$D_m = \frac{2}{m\pi} \sin(m\pi r) \quad (2.22)$$

where r is the duty cycle ($0 < r < 1$) of the period. The maximum efficiency is obtained for first-order QPM ($m = 1$) and 50% duty cycle ($r = 0.5$). This translates into replacing the effective nonlinear coefficient in the conversion efficiency equation 2.19 by the modified QPM nonlinear coefficient:

$$d_{QPM} = \frac{2}{\pi} d_{eff} \quad (2.23)$$

resulting in the efficiency:

$$P_3 = \eta_{QPM} \text{sinc}^2 \left[\frac{(\Delta k - K_1)L}{2} \right] L^2 P_1^2 \quad (2.24)$$

where $\eta_{\text{QPM}} = (2/\pi)^2 \eta$.

The reduction in effective nonlinear coefficient is only a slight detriment, as it is clearly compensated by the longer useful length for conversion. QPM is a very attractive method, because it can be engineered to phasematch interactions of interest, rather than rely on built-in limited birefringence, thus allowing access to most of a material's transparency window for nonlinear optics.

2.4 Difference-frequency generation and parametric oscillation

In this section we expand the results of the previous section to the conversion efficiency of difference-frequency generation (DFG), which is illustrated in figure 1.1. In DFG, a usually high power beam at frequency ω_3 , called the pump, is combined with a beam at frequency ω_1 , such that $\omega_1 < \omega_3$, called the signal, of lower power. Their nonlinear interaction produces photons at frequency $\omega_2 = \omega_3 - \omega_1$, which is called the idler. This is the typical mixing scheme that one would use to generate long wavelength radiation from shorter wavelength pump and signal beams. For instance, one such interaction of interest in this work is the mixing of easily available lasers at 1.3 and 1.55 μm , which give a difference-frequency idler at around 8 μm , a wavelength of interest to spectroscopists.

We can start simply from equation 2.12 (coupled wave equations for three wave mixing), and for simplicity assume the undepleted pump approximation is valid. The conversion efficiency is simply derived from these hypotheses, and we obtain:

$$\begin{aligned}
 P_2 &= \eta \operatorname{sinc}^2\left(\frac{\Delta k L}{2}\right) L^2 P_3 P_1 \\
 \eta &= \frac{2\omega_2^2 d_{\text{eff}}^2}{n_1 n_2 n_3 \epsilon_0 c^3 A_{\text{eff}}} = \frac{8\pi^2 d_{\text{eff}}^2}{n_1 n_2 n_3 \epsilon_0 c_0 \lambda_2^2 A_{\text{eff}}}
 \end{aligned}
 \tag{2.25}$$

This conversion efficiency is very similar to the efficiency for second harmonic generation, and the conclusions from this are similar: the larger the pump and signal

powers and the longer the crystal when phasematched, the higher the idler output intensity will be.

It is to be noted that when difference frequency generation occurs, not only are photons at the idler frequency produced, but the decomposition of the pump photons also produces photons at the signal, thus providing amplification at both signal and idler wavelengths. This is called parametric amplification. The idea to put a material with optical gain into a resonator is of course the basic idea behind the laser, so why not use a nonlinear optical material phasematched for a given interaction, apply the pump to it and put it in a resonator? This is called an optical parametric oscillator (OPO). Following the derivation of the conversion efficiency for DFG, it is easy to derive the parametric gain in a nonlinear optical material:

$$\gamma = \left(8 \frac{\omega_1 \omega_2 d_{eff}^2}{n_1 n_2 n_3 \epsilon_0 c_0^3} I_3 \right) \quad (2.26)$$

Clearly the gain depends on the intensity of the pump, and thus there exists a threshold intensity for which the gain equals the losses in the cavity, similar to laser thresholds. Once threshold is reached, the signal and idler photons that are created from quantum noise fluctuations start getting amplified. The oscillator can be either singly resonant (SRO), where either the signal or the idler are resonant in the cavity, or doubly resonant (DRO), where both signal and idler are resonated. DROs offer much lower threshold intensity, due to the fact that more photons of each frequency are present in the cavity to participate in the DFG process and provide gain at the other frequency. In general though, SROs are inherently more stable and thus are more commonly used, despite larger threshold requirements.

The signal and idler frequencies are of course set by the phasematching conditions. Tuning of the OPO output can be achieved by either angle tuning (birefringent phasematching), or temperature or multiple gratings (QPM). The pump wavelength can also be changed to tune the output.

OPOs are very widely studied tools and are important to many applications. They can provide more power than a simple DFG setup, and they can be built into widely tunable mid-infrared coherent radiation sources of high usefulness.

2.5 Introducing real-life effects: tensor symmetry and loss

So far in our derivations, for simplicity we have considered only interacting plane waves. This is a correct simplification since our goal was to introduce some concepts intuitively, without being bogged down by other factors that only make it more difficult to understand them. Of course, in real nonlinear optical experiments, there are many factors that do come into play. For instance, for interactions in bulk materials, the radiation sources used generally have a gaussian behavior, and thus we need to take into account focusing issues. In this regard, plane wave formalism has much more to do with waveguide interactions, where the propagating fields conserve the same profile over long distances. Both of these cases will be discussed in the following sections. For now, we would like to focus on introducing two important concepts, namely the nonlinear tensor and the effect of optical loss on conversion efficiency.

2.5.1 Nonlinear tensor symmetry and polarization effects

Whereas previously we wrote that the nonlinear coupling happened between any plane waves, when we want to tackle real-life problems, we have to consider how fields propagating with different polarizations are coupled by the second-order nonlinear effect. In general, the nonlinear coupling does not reduce to only a coefficient, but is represented by a third-rank tensor[1]. Materials are grouped in categories corresponding to the various symmetries of the nonlinear tensor. Let us focus on the case of zincblende semiconductors. They are said to belong to the symmetry group $\bar{4}3m$, requiring that d_{14} , d_{25} , and d_{36} be the only nonzero elements of the nonlinear tensor, all with the same value:

$$d = \begin{pmatrix} 0 & 0 & 0 & d_{14} & 0 & 0 \\ 0 & 0 & 0 & 0 & d_{14} & 0 \\ 0 & 0 & 0 & 0 & 0 & d_{14} \end{pmatrix} \quad (2.27)$$

This means that the tensor results only in $E_x \cdot E_y$, $E_x \cdot E_z$, or $E_y \cdot E_z$ types of coupling, where x , y , and z are the crystal axes[1]. This has direct implications in what kinds of polarizations are necessary to be able to obtain any conversion at all. For instance, when trying to do collinear SHG in GaAs, the incoming field must be polarized so that it has projections along two of the crystal axes simultaneously, which can then interact to produce the second harmonic. Since we are using (100) type wafers in our work and we generally have the beam propagating parallel to the surface of the wafer, then the beam must be aligned with [011] direction for a TE wave to get the desired projections, as illustrated in figure 2.6. The E field of the second harmonic is then polarized along the [100] direction, hence is a TM wave.

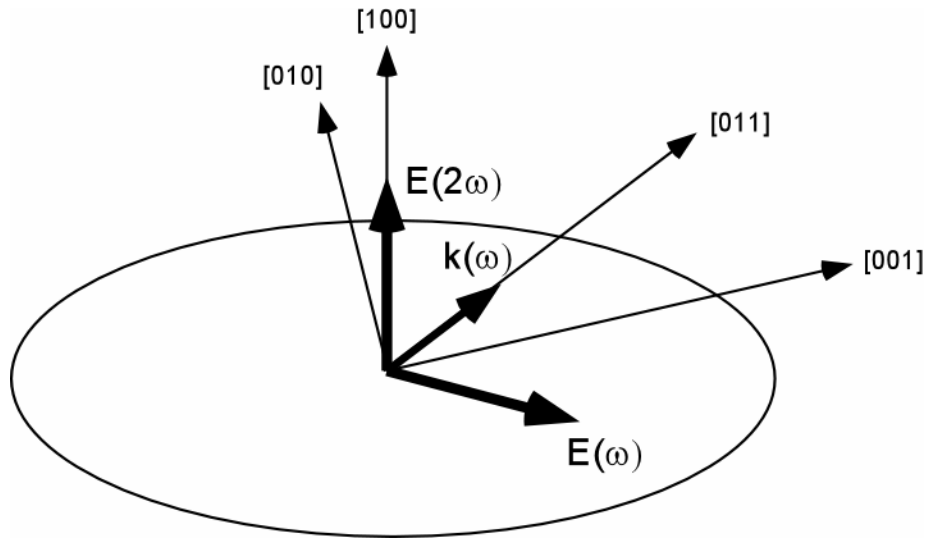


Figure 2.6: Typical polarization configuration for collinear SHG in GaAs.

Taking into account polarization dependence of the nonlinear interactions is critical when designing devices and trying to optimize conversion efficiency.

2.5.2 *Effects of optical loss on conversion efficiency*

Another important factor to consider is optical attenuation. As we will see in the following section for the material we are studying, no material is perfectly transparent,

even in its so called transparency range, for instance because of defects introduced during the fabrication process. In our derivation of the conversion efficiency, we completely ignore the attenuation at any of the frequencies. In fact, as we are going to see, because of the length of the nonlinear interactions, optical loss produces critical non-ideal behavior for nonlinear optical devices. In particular, intuitively, it will reduce the conversion efficiency, but it also modifies the general properties of the radiation and the proper functioning of the device.

As we will see later, optical loss is primarily a problem for waveguide devices, as the loss in bulk GaAs at the wavelengths of interest is generally very low. Considering this, and since plane wave formalism is very similar to waveguide formalism, we will use the plane wave model to study the effects of loss. Considering for instance the case of SHG for simplicity, and assuming attenuation coefficients of α_1 and α_3 for fundamental and second harmonic respectively, we can rewrite the coupled-wave equations as:

$$\begin{aligned}\frac{da_1}{dz} + \alpha_1 a_1 &= -ig a_3 a_1^* e^{-i\Delta k \cdot z} \\ \frac{da_3}{dz} + \alpha_3 a_3 &= -i \frac{g}{2} a_1^2 e^{i\Delta k \cdot z}\end{aligned}\tag{2.28}$$

Even in the undepleted pump approximation (assuming that $a_1(z) = a_1(0)e^{-i\alpha_1 z}$, meaning that photons at ω are lost only through attenuation, and we neglect photons converted to 2ω), solving for the second harmonic field evolution results in a very complicated expression:

$$a_3(z) = -\frac{ig}{2} a_1(0)^2 \left(\frac{e^{(i\Delta k - 2\alpha_1)z} - e^{-\alpha_3 z}}{i\Delta k - (2\alpha_1 - \alpha_3)} \right)\tag{2.29}$$

To compare the result with loss to the result without loss, we define the coefficient $\kappa = P_{\text{lossy}} / P_{\text{lossless}}$. In the phasematched case ($\Delta k = 0$),

$$\kappa = \frac{4e^{-2\alpha_3 L}}{L^2} \left(\frac{e^{-\alpha L} - 1}{\alpha} \right)^2 \quad (2.30)$$

$$\alpha = 2\alpha_1 - \alpha_3$$

It becomes obvious that when loss at all wavelengths exists (which is likely the case), the power output will exhibit a maximum as a function of length, after which the loss renders the remaining length useless, actually even worse than useless: the output power starts to decrease. Optical loss thus limits the useful length for conversion, in the process setting an upper bound on the maximum conversion efficiency.

2.6 Frequency conversion in waveguides

The derivations of the previous sections of course do not correspond to any real interactions, but are simple yet physically correct enough to let us emphasize the points of importance for the rest of this dissertation. During the course of this work, however, we had to build actual nonlinear frequency conversion devices. To be able to predict the performance of such devices requires developing expressions that are accurate for each case. Plane waves thus cannot be used for this purpose. Since we designed and built devices both in waveguide configurations and bulk material, we need to derive the needed expressions for both of these cases.

I will start by expanding the previous results to waves propagating in planar waveguides. Since the modes of a waveguide propagate like plane waves, the equations of this section will be very similar to those derived for plane waves, which is why it is a good idea to tackle waveguides before approaching nonlinear interactions in bulk material.

Once again, the theory of waveguides and of nonlinear optics in them has been well studied and written about historically[37], so I will only present what is relevant to this dissertation. I will begin with the description of waveguides in the terms of their propagation modes. From there, I will derive the conversion efficiency of nonlinear optical interactions in waveguides, clearly showing the similarity to plane waves equations from previous sections.

2.6.1 Waveguide geometry and waveguide modes

For the purpose of this dissertation, we will define a waveguide as follows: an optical waveguide is formed when material of high refractive index (called the core) is imbedded in material of low refractive index (called the cladding). Examples of typical waveguides used currently abound, such as those shown in figure 2.7.

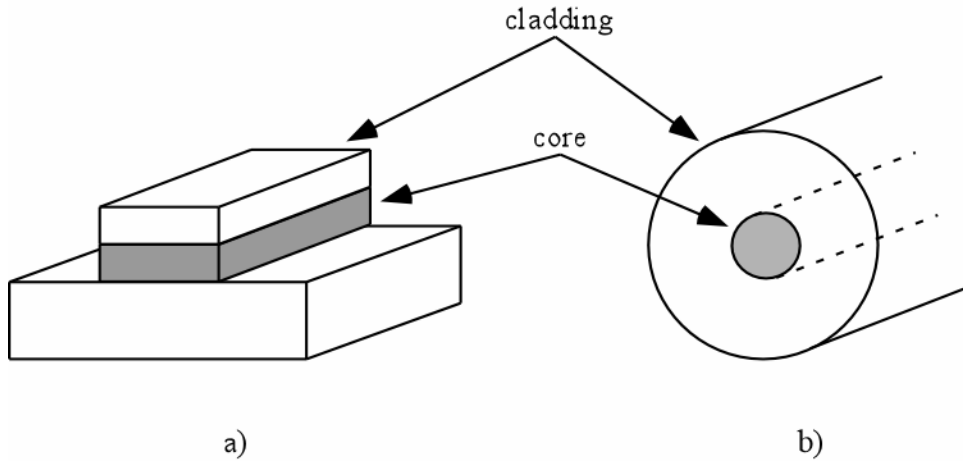


Figure 2.7: Schematic of two common types of waveguides: a) is a ridge waveguide, the type used in this work, while b) is a representation of an optical fiber found in communication networks.

Radiation in the waveguide can be trapped by total internal reflection occurring at the interfaces between core and cladding, and thus can propagate over large distances while not diffracting. Light propagating through the waveguide can thus be tightly confined on dimensions of the order of microns. This is a simple, intuitive way to understand the guiding effect. Of course, to be able to derive useful expressions with respect to the nonlinear optical interactions, one needs to develop an acceptable framework. To this effect, we are going to introduce the modes of a waveguide. Instead of employing the ray-optics idea of light bouncing back and forth between the core-cladding interfaces, which is insufficient to explain a number of important effects, we are going to use waveguide electromagnetic theory.

The modes of a waveguide are defined as the solution of the wave equation, with an index of refraction which is a function of position:

$$\nabla^2 \mathbf{E} - k_0^2 n^2(\mathbf{r}) \mathbf{E} = 0 \quad (2.31)$$

where the field is taken to be monochromatic and with a phase-front normal to the waveguide:

$$\mathbf{E}(r, t) = \mathbf{E}(r) e^{i(\omega t - \beta z)} \quad (2.32)$$

Equation 2.31 is analogous to the problem of an electron in a potential well of arbitrary shape, where the electron wavefunction can be confined, and the well creates a set of discrete energy levels, as well as a continuum above it. Similarly, solving equation 2.31 results in a discrete set of fields that are more or less confined inside the core, corresponding to a set of propagation constants, β , which are the eigenvalues of the problem. These are the guided modes of the structure. The continuum of solutions corresponds to fields that are partly confined, or not confined at all, and these are called the radiation modes of the structure. As the examples of figure 2.7 show, there are many possible geometries for waveguide structures, resulting in many combinations of guided and radiation modes. Designing and fabricating waveguides suited for efficient frequency conversion puts many constraints on the geometry, which will be covered in chapter 5.

Without solving for any particular waveguide at this point, we can make a few general remarks that will be useful to derive nonlinear optics expressions later. First of all, we will only concentrate on the guided modes of a waveguide. It is possible to use radiation modes for frequency conversion[38], but it is beyond the scope of this dissertation, since for this work we have designed waveguides for the collinear interaction of guided modes.

Let us consider a 2-dimensional waveguide index profile $n(x, y)$, with this profile remaining unchanged in the z direction. This is the most general way to treat a waveguide, provided we do not change the geometry of the guide as we go along the z direction. It is a simple case that will allow us to derive the equations we need. In this configuration, we can write the electric field of guided modes as:

$$\mathbf{E}_i(\mathbf{r}, t) = \tilde{\mathbf{E}}_i(x, y) A_i(z) e^{i(\omega t - \beta_i z)} \quad (2.33)$$

where i is used to index the modes, $\beta_i = 2\pi n_i/\lambda$ is the mode propagation constant, and n_i is the corresponding effective index. $\tilde{\mathbf{E}}_i(x, y)$ represents the unchanging mode profile, normalized to carry unity power, while $A_i(z)$ represents the envelope of the field, which can change as the mode propagates along the z direction due to attenuation.

In this work, the waveguides that we design are considered weakly guiding, thus it allows us to neglect any components in the z directions of the electric and magnetic fields. We take the modes to be TE or TM, and consider only the transverse components. In this case, we can reduce our problem to a scalar relationship:

$$\int_{-\infty}^{\infty} \int_{-\infty}^{\infty} \tilde{E}_i(x, y) \tilde{E}_j(x, y) dx dy = \delta_{ij} \quad (2.34)$$

The power carried by the mode is then

$$P_i = \frac{n_i \epsilon_0 c_0}{2} A_i^2 \quad (2.35)$$

We see then that we can simply reduce ourselves to a scalar problem, with simple normalization relationships and an expression for the modes that is very similar to a plane wave. From this, we are now going to derive the conversion efficiency for a nonlinear interaction in an optical waveguide with a constant two-dimensional index profile.

2.6.2 Conversion efficiency

To get the conversion efficiency, we can simply follow the same concepts as in the derivation for plane waves. We write coupled wave equations for the envelopes, A_i , using the slowly-varying approximation for simplicity. We eventually arrive to the following expressions, for SHG and DFG:

$$\begin{aligned}
P_3 &= \eta_{\text{wg}} \operatorname{sinc}^2\left(\frac{\Delta\beta \cdot L}{2}\right) L^2 P_1^2 && \text{SHG} \\
P_2 &= \eta_{\text{wg}} \operatorname{sinc}^2\left(\frac{\Delta\beta \cdot L}{2}\right) L^2 P_3 P_1 && \text{DFG}
\end{aligned} \tag{2.36}$$

where the normalized efficiency is similar to the plane wave case:

$$\begin{aligned}
\eta &= \frac{8\pi^2 d_{\text{eff}}^2}{n_1^2 n_3 \epsilon_0 c_0 \lambda^2 A_{\text{eff}}} && \text{SHG} \\
\eta &= \frac{8\pi^2 d_{\text{eff}}^2}{n_1 n_2 n_3 \epsilon_0 c_0 \lambda_2^2 A_{\text{eff}}} && \text{DFG}
\end{aligned} \tag{2.37}$$

The particularity of waveguide interaction is found in the value of A_{eff} :

$$\begin{aligned}
A_{\text{eff}} &= \left| \int_{-\infty}^{\infty} \int_{-\infty}^{\infty} \tilde{E}_3(x, y) \tilde{E}_1^2(x, y) dx dy \right|^{-2} && \text{SHG} \\
A_{\text{eff}} &= \left| \int_{-\infty}^{\infty} \int_{-\infty}^{\infty} \tilde{E}_2(x, y) \tilde{E}_3(x, y) \tilde{E}_1(x, y) dx dy \right|^{-2} && \text{DFG}
\end{aligned} \tag{2.38}$$

We can easily see that the conversion efficiency is going to be affected by the overlap between the generated field and the nonlinear polarization. This means that careful design of the waveguides is needed to optimize this overlap integral and maximize the efficiency. We will investigate the design considerations of our waveguides in chapter 5.

2.7 Frequency conversion in bulk material

While expressions for waveguide frequency conversion are very simple to derive due to the similarities with plane waves, we will see in this section that the expressions for interactions in bulk material are somewhat more complicated. However, we need to derive these expressions, because frequency conversion in bulk material has some

important advantages over the waveguide configuration that make it more useful for certain applications. In particular, while waveguides give us high efficiencies, the main reason for bulk materials is that the large apertures provide the ability to handle much higher power beams, so it is the only way to build high power sources.

In this section we will first cover how focusing of the gaussian beams generated by laser sources affects second harmonic generation, which is a simpler case than difference-frequency generation, which we will treat later on.

2.6.3 SHG with focused gaussian beams

Intuitively, following the fact that the conversion efficiency derived for plane waves and waveguides is inversely proportional to the square of an effective area, one would think that focusing gaussian beams to very tight spots would result in very large conversion efficiencies in bulk material. Unfortunately, tighter focusing also means larger diffraction and interaction lengths limited by the aperture of the piece used, which drives the efficiency down. Finding the optimal focusing conditions for the various beams involved in the nonlinear mixing process is thus very important to build efficient bulk frequency conversion devices.

Boyd and Klenman[39] have studied the effects of focusing on the conversion efficiency of SHG. For the pump beam of frequency ω with a beam waist w_0 , in a crystal of length L, they define a normalized focusing parameter

$$\xi = \frac{L}{b} \quad (2.39)$$

$$b = k_0 n(\omega) w_0^2$$

where b is the confocal parameter for the pump beam. Using this, they derive the optimum conversion efficiency to be

$$P_3 = \frac{8\pi d_{eff}^2}{n_1^2 n_3 c_0^3 \epsilon_0 \lambda^2} k_1 L P_1^2 h(B, \xi) \quad (2.40)$$

where B is the normalized walk-off length, which is 0 in GaAs for normal incidence interactions since GaAs has an isotropic index of refraction. Note that the optimum conversion efficiency does not always happen at $\Delta k = 0$, in particular in the tight focusing regime. The overall maximum conversion efficiency is found to be for $\xi = 2.84$. The efficiency will not decrease significantly when $b = L$, so one can take the pump beam confocal in the crystal to be a good approximation of the optimum condition. In this weak focusing regime, the phasematching follows the regular sinc^2 behavior, as we have observed experimentally (see chapter 4).

This result shows the significant difference between guided-wave interactions and bulk interactions. Increasing the crystal length and using tighter focusing do not necessarily result in improved performance in the bulk case, and additionally, tight focusing conditions can significantly decrease the SHG beam quality. For our purpose, one has to make sure that the crystal dimensions are such that the confocal pump beam situation can be approximately achieved, which in the case of GaAs QPM crystals grown epitaxially, the goal of this research project, translates into obtaining thick enough films.

2.6.4 DFG with focused gaussian beams

The effects of focusing on DFG interactions have also been extensively studied[40,41]. The detailed results of their studies are beyond the scope of this dissertation. However, we will present here the most important results. Similarly to the SHG case, one can calculate a general conversion efficiency that depends on the focusing parameters ξ_3 and ξ_1 for the pump and signal beams respectively, as well as the walk-off length B , a degeneracy parameter $r = \lambda_2/\lambda_1$, and the phase mismatch $\Delta k L/2$.

$$P_2 \propto P_3 P_1 L h(\xi_3, \xi_1, B, r, \frac{\Delta k L}{2}) \quad (2.41)$$

The absolute maximum of the efficiency is found for $B = 0$, $r = 1$, $\xi_3 = \xi_1 = 2.84$, and $\Delta k L/2 = 3.25$. Of course, these values are not in general typical of the DFG

interactions we are interested in. For one, we usually want the DFG to be non-degenerate, so that r would be greater than 1. As we mentioned for SHG, for normal incidence DFG in GaAs, $B = 0$, which greatly simplifies the problem, as it makes the optimal values of the pump and signal focusing parameters equal. The conversion efficiency has a maximum around the confocal pump/signal configuration, but it is a broad maximum that is not very different from the efficiency in the confocal idler configuration. This slight increase in efficiency has to be balanced with the fact that the quality of the idler beam (as characterized by its M^2 value) worsens as the pump and signal beams are more tightly focused, and that in turn this is made even worse as we get further away from degeneracy. So depending on the application, one has to make a tradeoff between the higher conversion efficiency available with the confocal pump, and the higher beam quality with the confocal idler. This tradeoff has to be seriously investigated when designing a device based on DFG for a particular interaction. We need to keep this in mind when we reach chapter 4, where we describe DFG results in thick orientation-patterned GaAs films.

2.8 Conclusion

In this chapter, we described the various configurations that we use for nonlinear frequency conversion devices in the rest of this work. Based on the expressions derived here, we will be able to predict conversion efficiencies in both waveguide and bulk material. We will also be able to compare experimental results to theory and determine how to improve the performance of these devices.

CHAPTER 3: ALL-EPITAXIAL ORIENTATION-PATTERNING

After going over the theory of nonlinear optical frequency conversion, I will in this chapter describe the technique developed to achieve quasi-phasesmatching in GaAs using an all-epitaxial fabrication process. I will start by describing the lattice inversion that we are trying to achieve, which will lead us into some important features of polar-on-nonpolar epitaxial growth. Then I will briefly describe the epitaxial technique of choice in our work, molecular beam epitaxy. Finally, I will detail the fabrication steps of our orientation template, and show the current limitations of the process, which will help explain the results of the next chapters.

3.1 Lattice inversion in GaAs

The most efficient QPM arrangement is obtained when one uses the modulation of the sign of the nonlinear coefficient, rather than modulation of its amplitude, as was explained in chapter 2. In GaAs, the nonlinearity arises from the asymmetry of the potential that electrons see between Ga and As atoms. The sign of d in turn can be changed then by changing this potential, which essentially comes down to changing the direction of the Ga-As bond. In GaAs, this lattice inversion can be observed by alternatively looking in two orthogonal $\langle 011 \rangle$ directions, as shown in figure 3.1. To summarize, what we want to accomplish when we talk about lattice inversion is a 90° rotation of the crystal around the $\langle 100 \rangle$ direction perpendicular to the two $\langle 011 \rangle$ directions considered. These two orientations are called antiphase, and the junction of two different phases is called antiphase boundaries (APBs), which consist of Ga-Ga or As-As bonds, depending on the plane in which they lie[42].

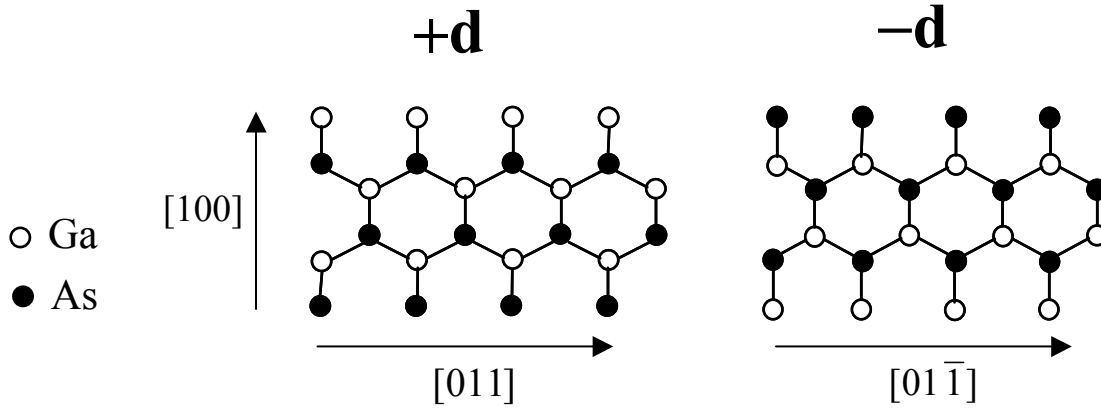


Figure 3.1: The sign of the nonlinear coefficient is changed by inverting the direction of the Ga-As bond in the GaAs lattice, which is equivalent to a 90° rotation of the lattice around the $[100]$ direction.

We want to come up with a scheme that will allow us to perform this lattice inversion using epitaxial growth processes. A simple way to think about it is the following: one needs to insert one, and exactly one, extra plane of atoms (either Ga or As) as we are growing along the $[100]$ direction, and then the crystal inversion is accomplished. This kind of lattice reversal clearly does not happen spontaneously in an epitaxial growth process, since epitaxy conserves the crystal lattice of the substrate and does not allow for extra Ga or As planes.

A more reasonable approach is then to use some kind of intermediate layer that will isolate the two phases of the GaAs lattice, and somehow help us control the orientation of the top layer with respect to that of the underlying substrate. Of course, the material chosen for that intermediate layer has to be closely lattice-matched to GaAs so that we can grow high-quality epitaxial layers. Additionally, a mechanism for controlling the orientation of the lattice must exist. These two conditions reduce the potential candidates greatly.

Ge emerged has the ideal material for this scheme for several reasons. For one, Ge is very closely lattice-matched to GaAs ($< 0.1\%$ mismatch), which allows for the growth of reasonably thick (thousands of angstroms) high quality epitaxial Ge layers. Si can also be used, but its larger lattice mismatch ($\sim 4\%$) limits the critical thickness on GaAs to about 15 \AA , thus making it very hard to use in a practical scheme, even though a group in Japan did have some success with it[31]. The second most important reason is that

extensive research had been done on the integration of III-V materials with Si and Ge, giving us a large background of work to start from. Figure 3.2 illustrates the type of GaAs/Ge/GaAs growth we want to achieve.

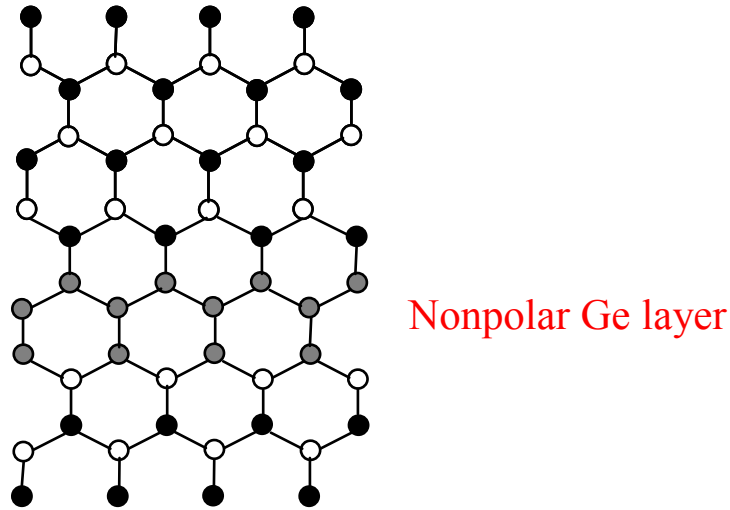


Figure 3.2: The nonpolar Ge layer is used as a buffer to isolate both orientations of the GaAs crystal.

The main problem of the growth of GaAs on Ge is the fact that the higher symmetry surface of Ge can support both GaAs orientations equally well. In fact, if no particular care is taken, both orientations of GaAs nucleate at the same time, leading to highly defective films with many antiphase domains (APDs). Such films are clearly not useful for optical or electrical applications. Fortunately for us, a great deal of research was accomplished on this problem and led us to a viable scheme for overcoming it. The main results that we used to begin our investigation were that single phase GaAs was grown on top of Si or Ge by using substrates misoriented several degrees from the (100) plane plus a combination of suitable growth conditions[43]. It is believed that the misorientation of the Ge surface breaks its symmetry and creates preferential nucleation sites for one of the two GaAs orientations. We should note here that some of the results indicate that single-phase GaAs begins to grow immediately on top of the misoriented Ge surface[44], while others show that single-phase GaAs only happens after a sufficient thickness has been grown and APDs have annihilated[45].

Figure 3.3 illustrates the basic scheme of our approach. By following previous work and establishing that we can grow one single orientation on top of a misoriented Ge

surface, then all we have to do is use a GaAs substrate of the opposite orientation and we then have accomplished our goal.

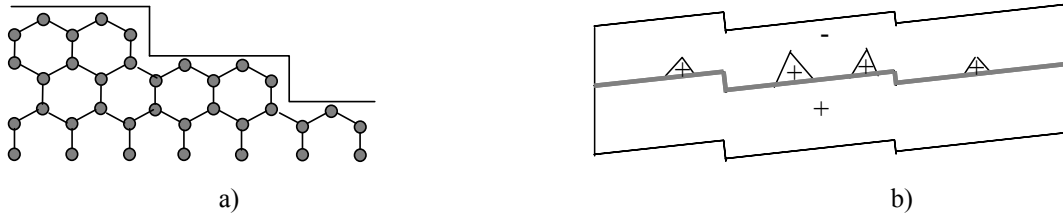


Figure 3.3: To achieve the all-epitaxial inversion, we have to use a misoriented Ge surface, as shown in a), and the right growth conditions to get to b), where single-domain GaAs of opposite orientation to that of the substrate is obtained after APDs have annihilated

I will encourage the reader to refer to previous work[46,47] for a thorough background on the research on polar-on-nonpolar epitaxy and the most important results that we tried to adapt to this work. Now that I have laid out the basic idea behind all-epitaxial inversion, I will in the next section describe the technique we used to grow the inverted GaAs films: molecular beam epitaxy.

3.2 Molecular beam epitaxy

Epitaxial growth is a process in which layers of a material are deposited on a substrate while conserving the substrate's crystalline structure. The development of epitaxial techniques, in semiconductors in particular, has been one of the most important advancements for the electronics and optoelectronics fields. While there exist many types of epitaxial growth techniques for III-V semiconductors, ranging from liquid-phase (LPE) to vapor-phase (MOCVD, HVPE) epitaxy, we have utilized molecular beam epitaxy (MBE), mostly because it is the epitaxial technique farthest from equilibrium and allows the greatest range of growth conditions for orientation control. There exist plenty of references on MBE, so I will only present here what is necessary to understand the fabrication process of our orientation templates.

3.2.1 Basic components of an MBE system

Figure 3.4 illustrates the basic components of an MBE system. The main component of an MBE system is an Ultra-High Vacuum (UHV) vacuum chamber, where background pressure can be as low as 10^{-11} torr. This chamber is pumped down to such low pressures by using various types of pumps, including a cryo pump, an ion pump, and cryo-shrouds filled with liquid nitrogen. A substrate is introduced in the chamber by a complex combination of load lock and UHV transfer tube, so that the MBE chamber itself is always under UHV. The substrate is put on a substrate manipulator and turned towards effusion cells containing elemental source materials. The substrate manipulator can heat up the substrate to the desired growth temperature (up to about 700 °C), and can rotate it to average out the spatial distribution of the sources. The cells produce atomic or molecular beams of elemental material directed at the substrate, where they combine to form the epitaxial layers deposited. Because of the UHV environment, the mean free path of the species in the chamber is much longer than the distance from the source to the substrate, thus allowing the species to remain in a beam form. The type of cell used depends on the material. Effusion cells are used for Al, Ga, Ge, where the beam flux is controlled by the temperature of the cell. A valved-cracker is used for supplying As: the sublimation zone temperature determines the maximum flux, the cracking zone temperature determines the As species, either As_2 or As_4 , and a valve is used to control the actual flux to the substrate. All of the cells also have shutters that are used to turn the molecular beams on or off, thus allowing very sharp (on the atomic scale) interfaces between layers of different compositions.

At typical growth temperatures, As will not incorporate by itself, so the growth rate is entirely determined by the arrival of the group III elements, and we usually grow with an As overpressure. Growth rate and beam flux are usually directly proportional for a given material and cell, depending mostly on the geometry of the system. Once the individual growth rate vs. temperature relationships have been calibrated, it is easy to grow any desired composition, for instance any AlGaAs composition, knowing that the total growth rate is the sum of the Al and Ga growth rates, and the composition is found by the ratios of growth rates.

In our MBE systems, the cell parameters and shutters are computer controlled, and software has been developed that allows us to write scripts for the structures we want to grow. This makes it simple to automate a lot of repetitive tasks such as removing the native oxide layer on the substrate every time we want to grow, and growing periodic structures, for instance.

Other important parts of the system include for instance the ion gauges (not pictured in figure 3.4) used to monitor pressure in the chamber and measure equivalent beam fluxes from the cells. Finally, the UHV system allows for some in-situ monitoring techniques, such as reflection high-energy electron diffraction (RHEED)[48], which is used to observe the surface reconstruction patterns of the layers being grown. This turned out to be instrumental in verifying in-situ that we had achieved lattice inversion[46]. RHEED can also be used to measure growth rate in real-time as well. Another technique we use to calibrate growth rate without breaking vacuum is optical reflectivity measurements, allowing us to back out with high precision the thickness of the grown layers.

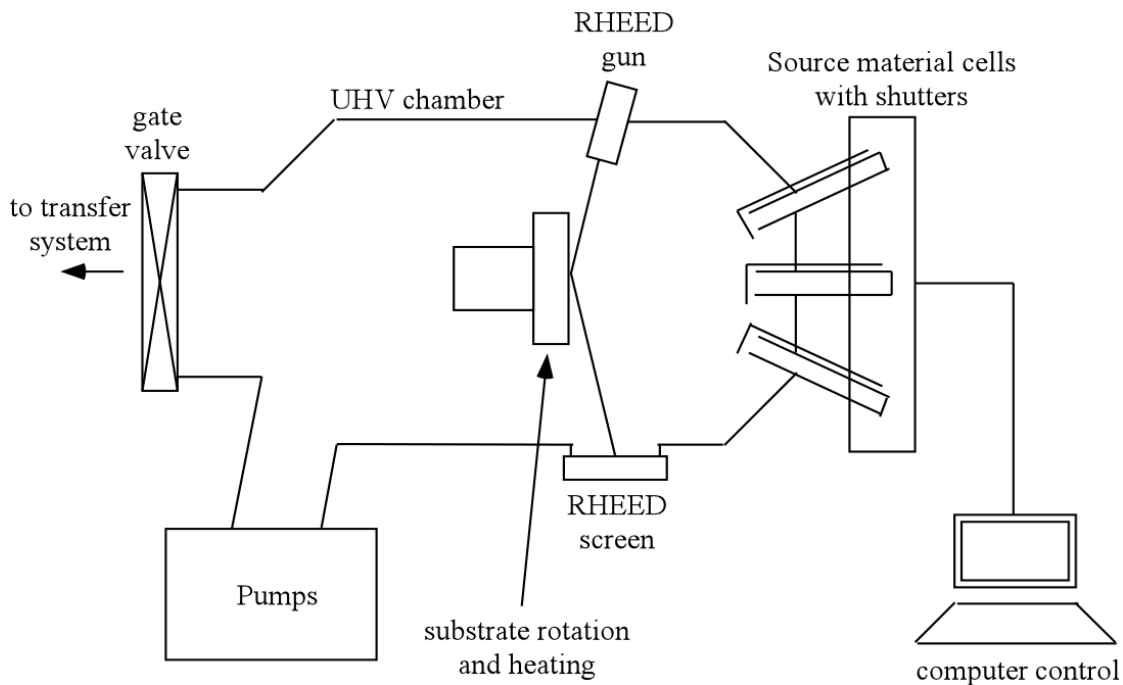


Figure 3.4: Schematic of an MBE system showing the most important parts

3.2.2 MBE growth of GaAs

After describing the basic components of an MBE system, let us look into more details at the growth mechanism of GaAs MBE. The first remark is that growing $\text{Al}_x\text{Ga}_{1-x}\text{As}$ is not significantly different from growing GaAs. Due to the higher reactivity of Al, its migration length is shorter, thus $\text{Al}_x\text{Ga}_{1-x}\text{As}$ is often grown at higher temperatures than GaAs. So in the following, we describe only the mechanisms for GaAs, knowing that $\text{Al}_x\text{Ga}_{1-x}\text{As}$ behaves similarly.

Since at typical growth temperatures, As will not incorporate by itself, the growth mechanism is controlled by the behavior of Ga adatoms impinging on the surface. When a Ga adatom arrives at the surface of the substrate, it can migrate until it finds a suitable nucleation site. The diffusion time is determined by the growth conditions such as substrate temperature, growth rate, and As overpressure. There are two types of growth that can then occur[49]. The first one is called step-flow growth, where Ga adatoms bind only at step edges along the surface (even nominally (100) GaAs wafers are not perfectly atomically flat). The Ga adatoms then react with As to form GaAs with the same structure as the underlying substrate. The step edge is then flowing along the surface as the adatoms keep getting incorporated. This occurs when the step density and Ga diffusion length are large enough so that Ga adatoms have time to reach the step edges.

When these conditions are not met, then Ga adatoms end up reacting with As before reaching the step edges. Subsequent nucleation happens around these adatoms, resulting in islands of GaAs nucleating on the flat regions between the step edges. Eventually, islands will join up and form a new layer and the process will start again. This is called island nucleation. Step-flow growth generally results in films with fewer defects and thus is preferred for high-quality epitaxy[49].

In this work, we intentionally introduced a misorientation of the wafer from the (100) plane by a few degrees towards either the (111)A or (111)B planes. This results in an increased density of step edges, depending on the amount of misorientation. Growth on (111)A misoriented substrates is usually preferred in MBE because of the different types of steps present. In (111)A misoriented substrates, Ga dangling bonds are exposed, while (111)B misoriented substrates have As dangling bonds. These As dangling bonds have higher reactivity and the growth can proceed from any point on the step edge,

resulting in very irregular finger-like projections from the steps. In the end, films grown on (111)B misoriented substrates can be very rough and have lots of defects. On (111)A misoriented substrates, growth occurs mostly at kink sites where As bonds are dangling, resulting in step-flow growth and smooth films. Our process calls for growth of films in both orientations, so we had to find a way to deal with this issue, which we will cover later in this chapter.

To conclude this section on GaAs MBE, I want to mention another technique used in this work: migration enhanced epitaxy (MEE). In MEE, instead of having both Ga and As shutters open at the same time, they are alternatively open, so as to supply Ga and As separately to the substrate. In the brief As-free (or at least low-As overpressure) environment, the Ga diffusion length across the surface is greatly enhanced[50,51]. Typically, we open the Ga shutter long enough to deposit approximately one monolayer, then close the Ga shutter and pause for a few seconds, to let the Ga adatoms migrate to the nucleation sites. Then the As shutter is opened to supply As to grow one monolayer of GaAs. This process is looped many times to grow the desired thickness. In general, this technique is used to smooth out rough surfaces, because it promotes step-flow growth, but has also found applications in very low temperature growth, for instance. Unfortunately, because it is extremely slow and very hard mechanically on the shuttering system, it is only used for very thin films.

3.2.3 MBE growth of Ge

The MBE growth of Ge is much simpler than GaAs, because only one species is involved. However, the growth rate of Ge using an effusion cell similar to those used for Al and Ga ends up being very low because of the low vapor pressure of Ge. We ended up using growth rates on the order of 20 nm/hr at cell temperatures of 1200 °C, close to the maximum temperature allowed by that cell. Typical $\text{Al}_x\text{Ga}_{1-x}\text{As}$ growth rates can be as high as 1 $\mu\text{m/hr}$. Fortunately, we only needed to grow very thin layers of Ge, on the order of a few tens of angstroms, so this was not a problem. We were also fortunate in this project to have two MBE systems connected by a UHV transfer tube, allowing us to keep one system clean of Ge for high-quality III-V growth, while the other system was used to

grow the Ge layers. Ge contamination had to be avoided in the first system because Ge is an amphoteric dopant in GaAs.

3.3 Orientation template fabrication process

For the detailed study of the growth of single-phase inverted GaAs layers, I will refer the reader to the work of Ebert and Eyres[46,47], my predecessors on this project. In this section, I want to describe the fabrication process of the orientation templates we used for the rest of this work. While in no way perfect, these templates proved very successful for the growth of high-quality thick GaAs films for QPM experiments, and still useful to demonstrate guided-wave interactions. I will begin by briefly describing the growth conditions leading to lattice inversion. I will then detail the entire flow of the fabrication process, and finally I will point out the problems with the templates as they now exist.

3.3.1 Lattice inversion

From the earlier studies of Ebert and Eyres[46,47], the lattice inversion was found to rely on the fact that we could control the orientation of the GaAs grown on top of the Ge layer, regardless of the orientation of the underlying substrate. Following this fact, all that was needed was to decide on which orientation to grow on the Ge layer, use a substrate of the opposite orientation and the lattice inversion was achieved.

The orientation of the top layer depends on many different growth parameters: substrate temperature, growth rates, presence of an As or Ga prelayer, prelayer coverage and annealing of the Ge surface[46]. While it is possible with different combinations of these parameters to obtain the different orientations of GaAs, early studies seemed to indicate that lattice inversion and high-quality epitaxy could only be obtained with (111)B misoriented substrates. For this reason, our current templates all use (111)B misoriented substrates. Further studies have shown that using (111)A misoriented substrates is not only possible, but might actually lead to higher quality templates. This remains to be investigated further. In the rest of this dissertation, we only refer to templates grown on (111)B misoriented substrates.

The basic recipe that we used to grow inverted GaAs was as follows:

- Expose the Ge surface to an As₂ flux to create an As prelayer. Since we grew in MBE systems which were used for III-V growth, there was a high As background already present in the machine, thus it is reasonable to think that we could not guarantee that an As prelayer did not exist on every wafer. The As₂ flux only served as an insurance of a full As prelayer.
- Deposition of GaAs at an indicated substrate temperature of 500 °C. The quality of this layer is critical to the process, since this will be the layer on which regrowth will take place. Growth conditions such as growth rate and type of effusion cell used (in particular to decrease the occurrence of oval defects), as well as the Ge surface morphology, determine the density of antiphase domains and how far they propagate through the layer.

For the second step, we tried both standard coevaporation MBE and MEE for the first 100 Å of GaAs, but did not find any apparent difference in the density of APDs and their dimensions. This recipe results in GaAs misoriented towards (111)A when grown on a substrate misoriented towards (111)B. Once we know this, we can go on to the full template fabrication process.

3.3.2 *Template fabrication process*

The fabrication of the template can be divided into three distinct phases: the epitaxial growth of multiple layers including the inverted ones, the etching of the QPM patterns on the wafer, and finally the regrowth of a seed layer for subsequent processing, or, alternatively, the growth of the waveguide structure. Figure 3.7 illustrates these three phases, as well as both types of devices that can be grown on the templates.

We used n+ GaAs substrates misoriented 4° towards (111)B. As mentioned in section 3.2.2, growth on this kind of substrates results in very rough surfaces, so particular care had to be taken, in light of the fact that roughness led to large densities of APDs in previous studies[47]. To solve this problem, we used an AlAs/GaAs superlattice. which can pin impurities and defects at AlAs/GaAs interfaces, thus leading to smoother films[46]. Significant improvements were observed using these buffer layers, and in subsequent growths we have always started with such a superlattice.

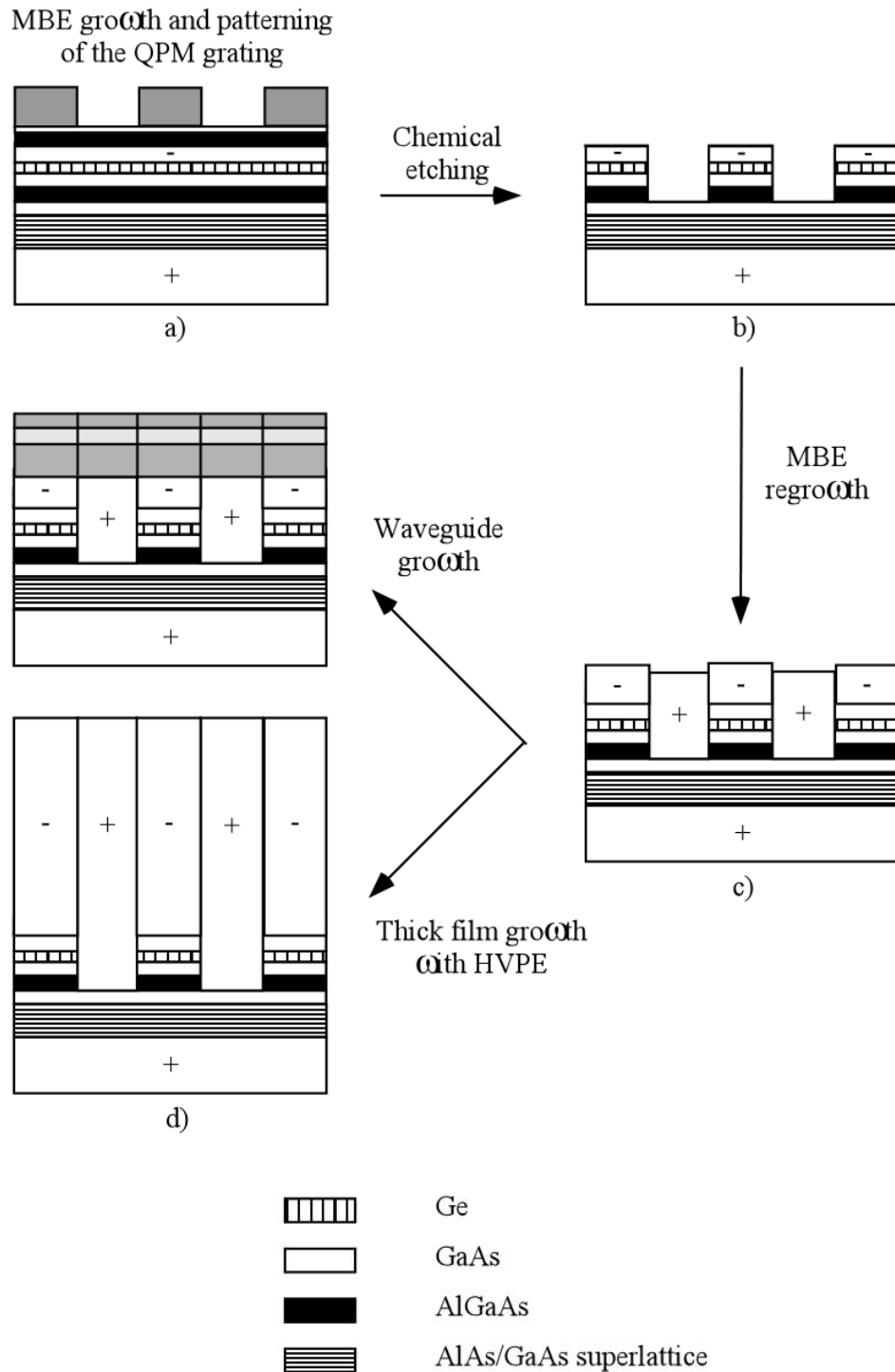


Figure 3.5: Orientation-patterned GaAs fabrication process: a) MBE growth of inverted layers (indicated by + and -) using GaAs/Ge/GaAs heteroepitaxy, followed by patterning of desired QPM grating with photoresist; b) both orientations are exposed with the patterned period after various chemical etching steps; c) the sample is reloaded in the MBE system for regrowth; d) either the waveguide growth follows or the sample is taken out and put in an HVPE system for thick film growth.

The actual buffer used consisted of three sets of 5 repetitions of 450 Å GaAs/50 Å AlAs, separated by 500 Å AlAs marker layers for easier observation with SEM and then finished by 1000 Å of GaAs. The surface of this GaAs will serve as the seed for one of the orientations during the regrowth process. The entire buffer was deposited at our standard growth temperature of 620 °C. The total thickness of the buffer layer was 1 μm.

One of the important design considerations of this template is the corrugation depth, as shown in figure 3.5b. Making it as shallow as possible is desirable, as we will see in the rest of this chapter. For this reason, instead of relying on timed etches, we decided to implement etch-stop layers, which will relax the constraints on the etching and help us control the depth more accurately.

Following the 1000 Å of GaAs, one such etch stop layer was grown, consisting of 200 Å of Al_{0.80}Ga_{0.20}As, also at 620 °C. Finally, the first part of the growth was completed by a 100 Å thick layer of GaAs at the same substrate temperature.

The wafer was then transferred into the second MBE system, where the Ge cell was located, through the UHV transfer tube. The substrate was heated to 350 °C and a thin layer of 30 Å of Ge was grown. The Ge thickness was found not to be critical to the success of the lattice inversion, as long as it was kept between 30 and 100 Å. 30 Å was the chosen thickness to also keep the corrugation as low as possible.

The wafer was then transferred back to the first chamber for the growth of the inverted layers. We followed the recipe outline earlier, depositing first 1000 Å of GaAs at 500 °C after having exposed the wafer to an As₂ flux at 350 °C. We found that 1000 Å was the minimum thickness we could reliably grow that would lead to single phase GaAs. Most of the time, thinner layers resulted in catastrophic failures during the etching steps, in particular large densities of etch pits and lift-off of some parts of the inverted layers. We did manage on occasion to grow successful wafers with a thinner GaAs layer on top of Ge, down to about 100 Å, but inconsistent results forced us to use the thicker layer for more reliability.

This GaAs layer will serve as the seed for the other orientation during the regrowth step, so its surface had to be protected from contaminants such as the photoresist used for patterning the QPM gratings. For that reason, we used another 200 Å

$\text{Al}_{0.80}\text{Ga}_{0.20}\text{As}$ etch-stop layer, followed by a 100 Å GaAs cap to finish the growth. The final structure of the first growth is shown in figure 3.6.

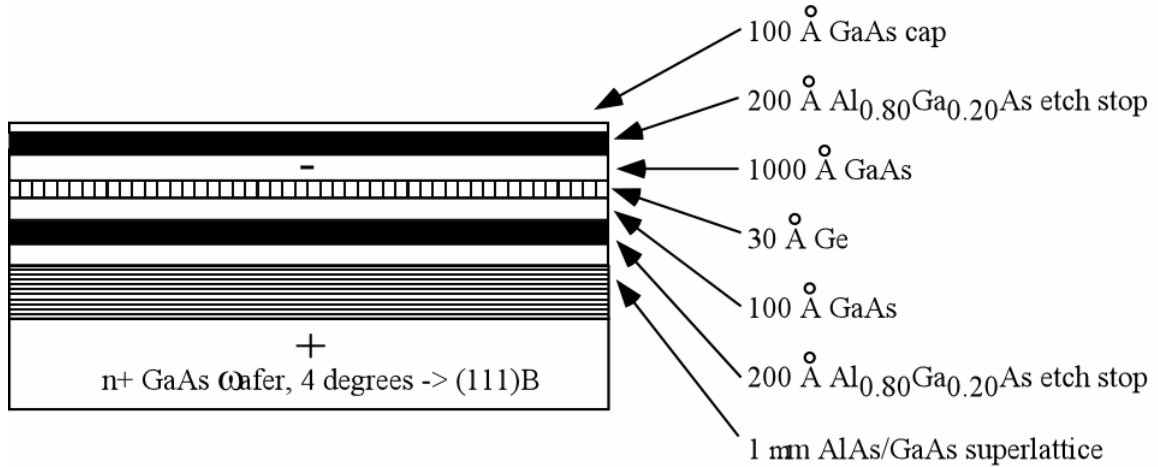


Figure 3.6: Epitaxial structure of the orientation template

In-situ RHEED was used to confirm the orientation rotation, by comparing reconstruction patterns on the original substrate and on the material grown above the Ge layer[46]. Once the wafer was out of the MBE system, we performed a quick optical microscope scan of the surface to reveal the density of imperfections, mostly oval defects.

We then moved on to the next step in the fabrication process: the patterning and etching of the wafer. We patterned photoresist on the wafer with gratings of different periods and shapes. Typically, dimensions ranged from a few microns periods for waveguide devices and 1 μm pumped devices in thick GaAs films, to tens of microns for pumps with longer wavelengths (see chapter 4 and 5 for more details). The patterns were then etched with a series of selective wet chemical etching steps as described in figure 3.7. The mixture of 1:1 hydrochloric acid:water was used to remove any oxides present on the surface and selectively etch high-Al content layers over GaAs. 4:1 citric acid:hydrogen peroxide, on the other hand, selectively etches GaAs over high-Al content layers, and also etches Ge. Figure 3.7 makes it clear how the etch-stop layers help control the corrugation depth as well as protect the GaAs surfaces that will be regrown on from contamination. One problem we encountered was residual Al “blobs” after removing the etch-stop layers. This was taken care of by several short hydrogen peroxide/hydrochloric

acid dips[47]. The use of etch-stop layers allowed us to obtain a reliable, reproducible process. It was very easy to control the etching, because we could see the wafer color changing while the layers were being etched due to the index contrast between GaAs and high-Al content AlGaAs. The final corrugation was approximately 1300 Å.

The wafer was put into the load chamber of the MBE system under vacuum very quickly after the final etch and rinse, so as to minimize contamination and prevent oxide formation on the surface. We found that there was no need for the typical oxide blow-off step usually taken for commercial wafers loaded into the system, which means that our quick-loading technique worked well. We then proceeded with the last part of the template fabrication: the regrowth on the patterned substrate.

After raising the substrate temperature to 500 °C, the deposition was initiated with MEE of GaAs, to try to smooth out the corrugated substrate and fill in the trenches of the patterns. We tried different thicknesses, with varying success and results can be found in the next section. We then grew a buffer layer exactly similar to the superlattice described earlier, for the same reasons: smoothing out the growth on top of the (111)B misoriented domains. After that, either we deposited 4 to 5 μm of GaAs to serve as a seed for the thick film growth, or we grew our waveguide structure directly, as shown in figure 3.5d.

In the next section, we focus on the templates for thick film growth, knowing that similar observations can be made for the waveguide films grown on the patterned substrates.

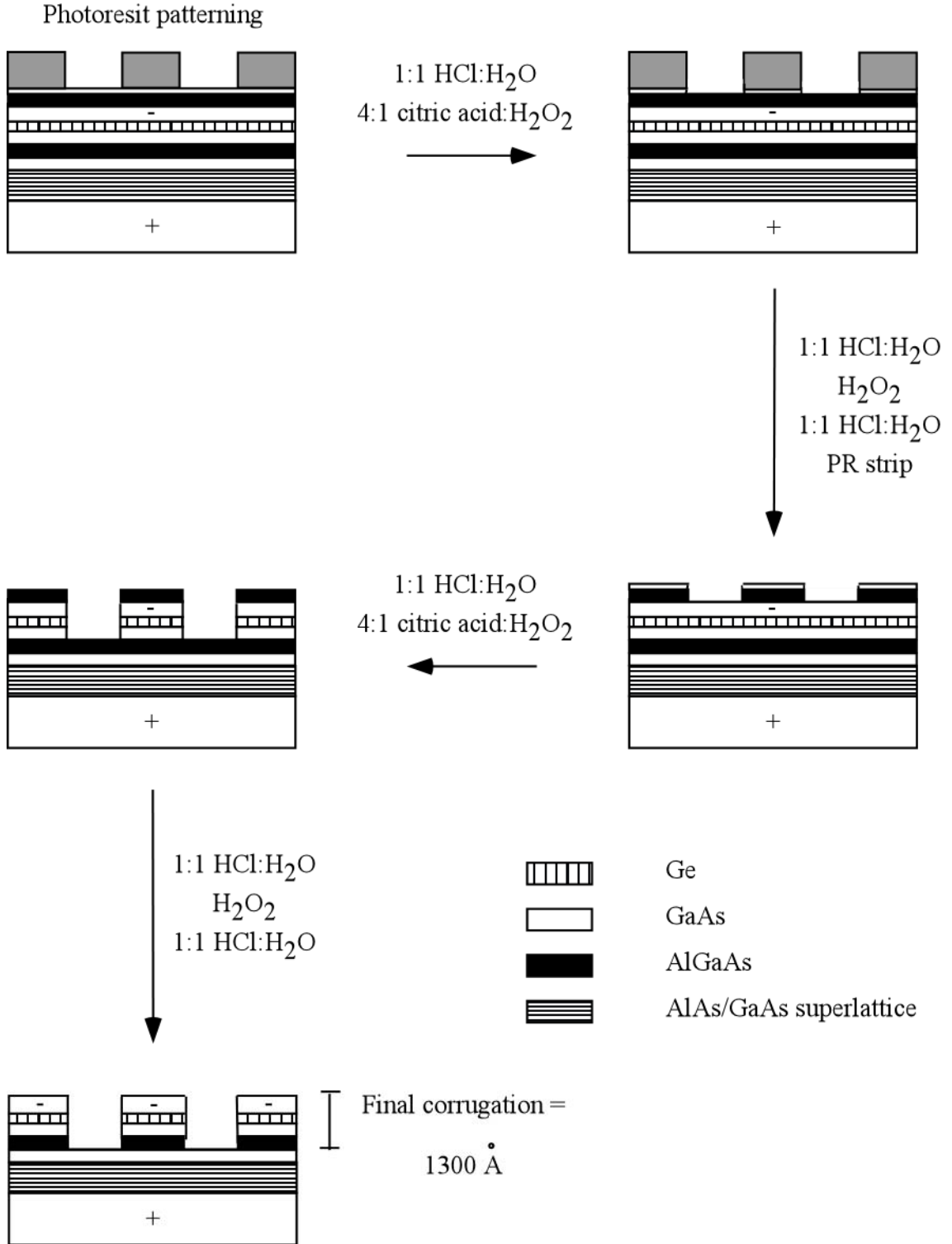


Figure 3.7: The wet-etching steps for the template fabrication involve using selective etchants to control the corrugation depth. The etch-stop layers are also used to isolate the GaAs surface that will be regrown on from contamination such as the photoresist.

3.3.3 MBE regrowth results

Under all the MBE conditions tried for regrowth, the APBs ended up propagating vertically, such as what is shown in figure 3.8. For very short periods, the duty cycle ends up not being close to 50% because of pronounced undercut during the wet chemical etching. With the MBE regrowth, we observed aspect ratios of up to 10:1 (domain height:domain width). We also demonstrated periods short enough to phasematch any interaction in the transparency range of $\text{Al}_x\text{Ga}_{1-x}\text{As}$.

Unfortunately, while MBE regrowth does conserve the domain orientation as the film propagates vertically, it is not an ideal regrowth technique, and leaves the templates far from perfect. First, the thickness of the MEE layer deposition plays a crucial role in determining the quality of the final template, as shown in figure 3.9: a 60 μm period grating where growth was initiated with only 500 \AA of MEE clearly looks worse than the same grating where growth was initiated with 1000 \AA of MEE. In particular, a SEM picture of the very defective grating (figure 3.9a) shows that the defects are actually pits forming at the APBs.

The other problem comes with the change in regrowth quality with grating period. Figure 3.10 shows a comparison of the top surface of the final template after 4 μm of GaAs have been grown as a seed layer. While the 60 μm grating shows very few defects at the APBs following 1000 \AA of MEE, the 8 μm period grating looks very rough in comparison, with clearly less than 50% duty cycle. This is most likely due to worsening lithography and etching quality as the period decreases. Not only would this lead in general to a reduced efficiency because of the less-than-ideal duty cycle, we will see that it makes growing thick films with short periods very difficult. Note also that on the 60 μm period, one orientation is clearly rougher than the other: this is the (111)B misoriented material.

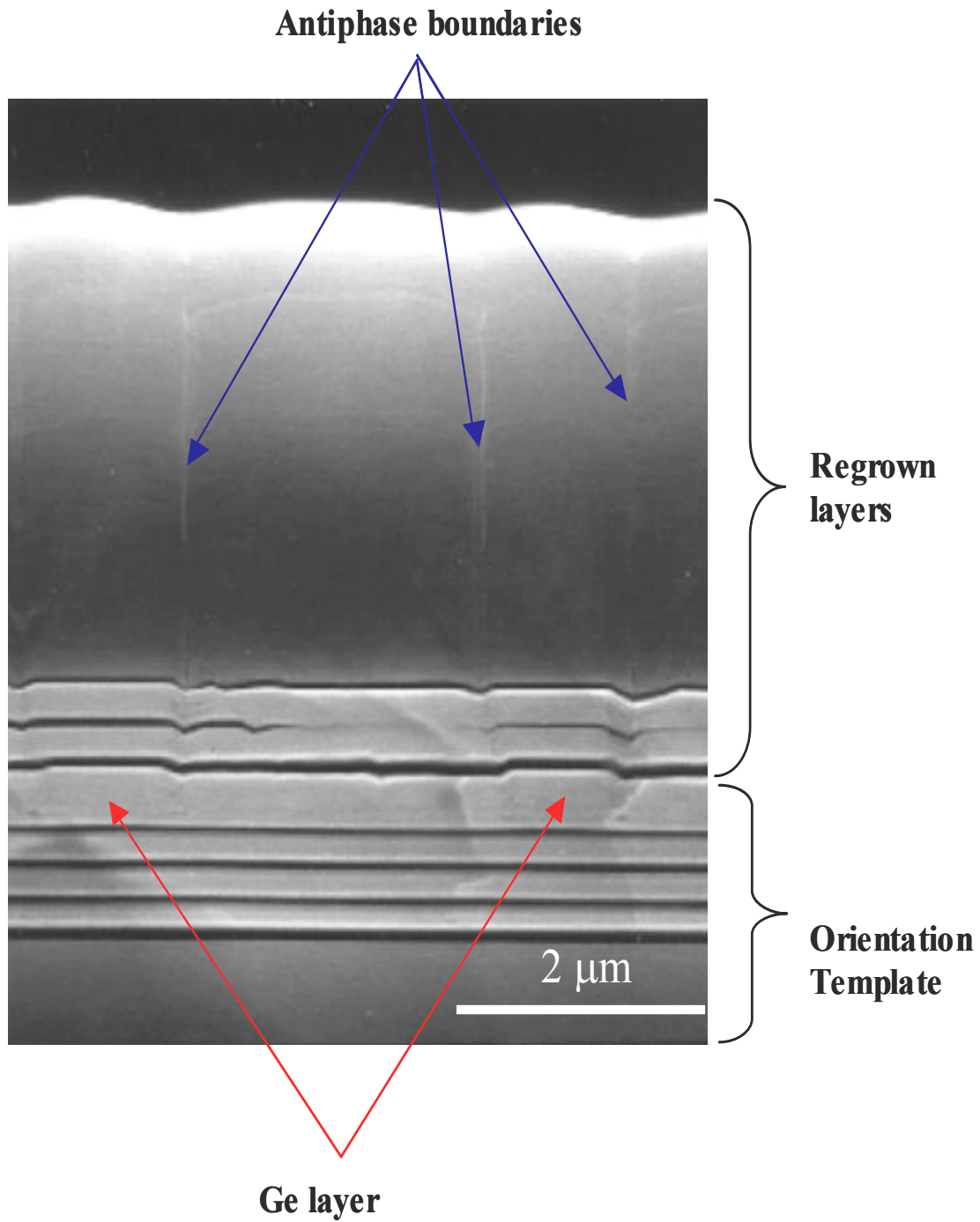


Figure 3.8: SEM cross-section of MBE-regrown orientation-patterned film, showing clearly the APBs propagating vertically. One can also see the AIAs marker layers in both the original epitaxial growth and the subsequent regrowth[30].

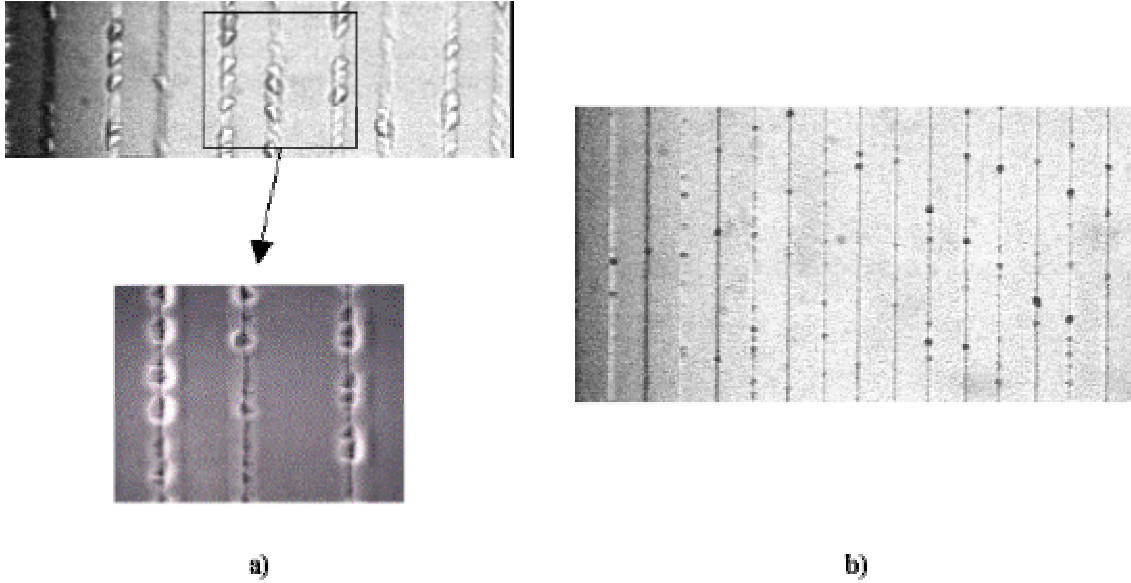


Figure 3.9: A 60 μm grating top surface viewed through an optical microscope shows a) a lot of defects accumulating at the APBs for only 500 \AA of MEE, and b) a better quality film when 1000 \AA of MEE is used. An SEM close-up of the defects reveals that they are pits forming during the epitaxial regrowth.

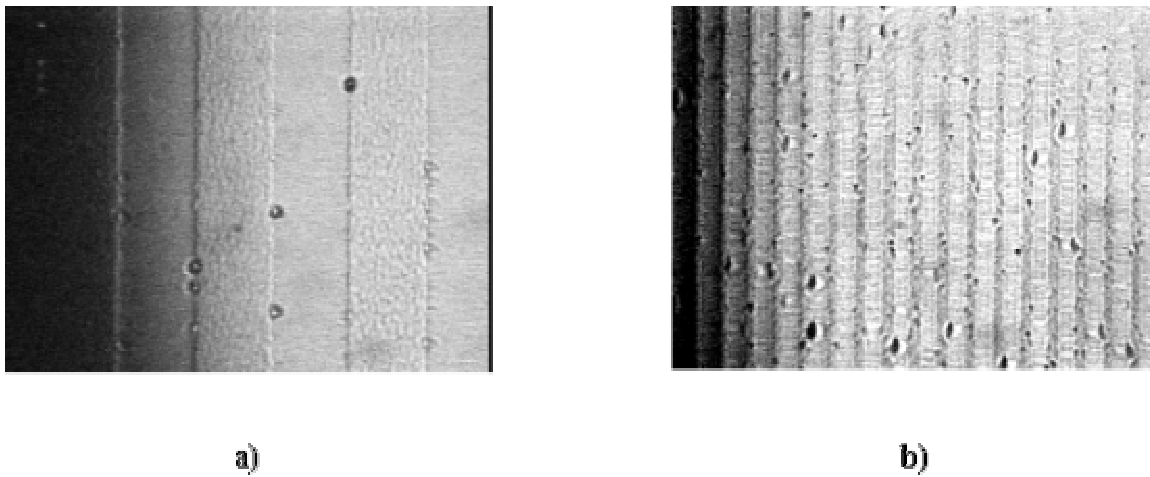


Figure 3.10: Optical microscope view of template top surface for a) 60 microns period, and b) 8 microns period. Defects tend to accumulate at the boundaries between the domains of different orientations, and the density of defects as well as the roughness of the surface visibly increases as the domain period is reduced.

3.4 Conclusion

In this section we described how we fabricated our orientation-patterned templates for our QPM devices. These templates are clearly not ideal, since they have over 1000 Å of corrugation before regrowth. While the MEE initiated regrowth and the slight difference in growth rates between the two orientations might help reduce this, we are still left with a large corrugation after regrowth. For very short period, this is compounded by (and likely related to) the worsening quality of the epitaxial layers and the template in general. Even though these templates are not ideal, they use very simple processing steps, they produce well-controlled corrugation, and because of this, we can fabricate them with a high degree of reliability. We will see in the next two sections how the shortcomings of the templates affect the growth and performance of the thick films and waveguide devices.

Other ways of fabricating the template can be investigated, in order to obtain zero corrugation and very smooth surfaces for all grating periods. The first possibility would be to use dry-etching techniques instead of wet etching, so that the etching pits and undercutting observed would be reduced or eliminated. If so, we could use a much thinner GaAs layer on top of the Ge, as long as it is mostly single-phase, and considerable reduce the corrugation. A primary reason for using wet etching was that the dry etching equipment here was often out of order, but there is no fundamental reason why it should not be used if reliable equipment can be found.

Another approach is the following: one can think of patterning the original substrate, and back-etching it, with the appropriate QPM period, then grow inside the trenches the template structure finishing with the inverted layer, with the exact depth of the trenches as the total thickness. Of course, this would require a way to lift off the material deposited on top of the wafer in the non-etched region. Using dielectric layers as a mask for selective area regrowth has been investigated[47], but requires strained layers to help with the lift-off process. A similar idea would use a strained epitaxial layer instead of a dielectric, or maybe one could use a similar process to that used in releasing a micromechanical membrane for tunable vertical cavity devices[52]. These would all generate close to zero corrugation, but one would still have to overcome the issue of the quality of regrowth on very short periods. Using dry etching techniques instead of wet

etching, to obtain vertical etching profiles and little to no undercut seems to be a possible solution to this problem.

Either way, growing thin inverted layers and reducing the density and size of the APDs also needs to be investigated. Analysis of older results seems to indicate that a different growth recipe might be a step in that direction[47]. This would be beneficial no matter what type of fabrication process one chooses to use.

CHAPTER 4: GROWTH AND CHARACTERIZATION OF THICK FILMS OF ORIENTATION-PATTERNED GAAS

Once we have the ability to grow all-epitaxial templates of reasonably high-quality, we can start thinking of what to do with them and what kinds of devices to grow on them. Growing thick films on the orientation templates, as shown in figure 4.1, with thickness on the order of a few hundreds of microns to a few millimeters, would allow us to perform bulk-like optics, by focusing beams through the aperture, instead of having to deal with coupling light into waveguides, for instance. Additionally, large apertures are better suited to high-power handling and device performance is not going to be affected by the corrugation at the template or the quality of fabrication processes as in waveguides.

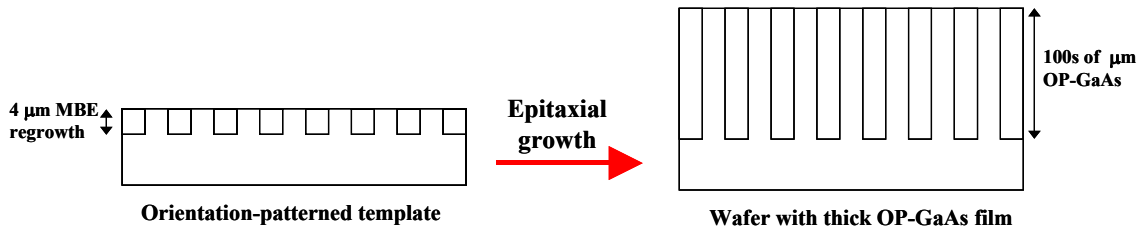


Figure 4.1: Schematic describing the idea behind the growth of thick films on the orientation templates. We hope that the template can serve as a seed and that the epitaxial process used to grow the thick layers can let the domains grow vertically without closing.

In this chapter, I will first describe the epitaxial technique chosen to grow the thick films on top of our orientation template, then show the results of the growth of thick GaAs layers, focusing on the characteristic defects of these films and how they relate to the quality of the template as described in the previous chapter. Finally, I will discuss the optical properties of these films, starting with linear properties, then concluding with various nonlinear optical experiments performed in them, confirming that OP-GaAs is already fulfilling its promise as a nonlinear material of choice for mid-IR applications.

4.1 Hydride vapor phase epitaxy

There exists several epitaxial techniques capable of growing thick films of GaAs, such as metal-organic chemical vapor deposition (MOCVD)[53], chloride vapor phase epitaxy (chloride-VPE)[54], and close-space vapor transport (CSVTE)[55]. Any of these techniques could be investigated for the purpose of growing on our templates. In fact, MOCVD has proven to be able to grow at least thin films of orientation-patterned AlGaAs on diffusion-bonded templates[28]. MOCVD would be a good solution to investigate, due to the current popularity of this technique. We decided to try and use another epitaxial technique, called hydride vapor phase epitaxy (HVPE), due to the success of a French group in growing thick films of GaAs on a diffusion-bonded template using this technique[56]. We entered a collaboration with this French group at the central research laboratory of Thales (formerly Thomson), sending them our templates, and getting back thick films of orientation-patterned GaAs from their grower, Bruno Gerard.

The HVPE process uses arsine (AsH_3) and HCl/Ga as the sources of material, with H_2 as the carrier gas. The sample is placed in a hot-walled horizontal quartz reactor. The reactor has two inlets, one for the flow of $\text{HCl}+\text{H}_2$ over the 7N Ga source (providing GaCl gaseous molecules in the vapor phase) and the other bypassing the source for AsH_3 , main H_2 carrier flow and additional HCl , for additional control of the vapor composition over the wafer. The GaCl and AsH_3 then enter the reactor, and AsH_3 gets decomposed into a combination of H_2 , As_2 and As_4 . The As compounds then react with GaCl and H_2 over the surface of the substrate to form GaAs and extra HCl . In this particular reactor, the growth was done at atmospheric pressure and the temperatures of the Ga source and of the GaAs substrate were kept at 850°C and 750°C respectively.

The vapor composition determines the growth of GaAs. For this reason, HVPE is superior to chloride-VPE because the As and Ga supplies are completely independent, thus allow extensive control over the growth parameters, and this is probably why HVPE turned out to be a good choice for this application. The various growth regimes of HVPE have been widely studied, in particular the growth rates on various crystal planes of GaAs[57]. HVPE is capable of high growth rates, up to $50\ \mu\text{m}/\text{hr}$, and has been shown to produce GaAs films with very low background doping, which is also important for our purpose.

In the case of the samples discussed later, Bruno Gerard used growth conditions that limited the growth rate to about 20 $\mu\text{m/hr}$, but designed to make the antiphase domains propagate vertically. Recent results on growth morphology, from a group including our collaborator, will help interpret the results I am going to show in the next sections.

4.2 Growth of 0.5 mm thick films of OP-GaAs

In this section we will describe the results of the growth of 0.5 mm thick OP-GaAs films by HVPE on our MBE-grown orientation templates, focusing on the propagation of the antiphase domains throughout the films and the types of defects present, as well as possible reasons for them. Finally, we will try to show that the behavior of the antiphase domains can be explained by results of selective area growth experiments performed by the HVPE growers.

4.2.1 Antiphase domain propagation and film quality

We grew templates as described in the previous chapter, with a 4 μm seed layer of GaAs, then sent them to the group in Thales for them to grow on. The first runs of growth consisted of growing only 200 μm thick films and determine if this process was going to work at all on our templates. More details on the first HVPE growth runs can be found in Eyres[47]. Since these experiments turned out successful, while limited in scope, we decided to design a mask with QPM gratings for useful and interesting interactions, and asked the grower to deposit 500 μm films on them. Because the first runs had shown that gratings with k vector oriented along the wafer misorientation direction did not produce good quality thick films[47], we limited ourselves to gratings oriented in the perpendicular direction, as shown in figure 4.2.

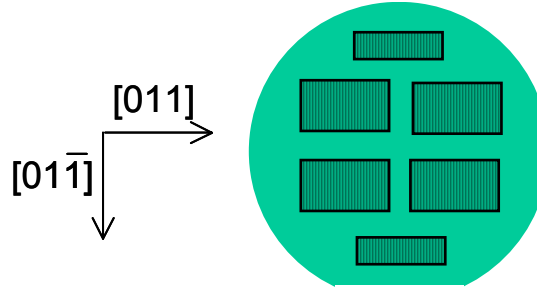


Figure 4.2: Orientation of the gratings on the template. All the QPM gratings were placed with their k vector in the $[011]$ direction, since those in the other directions did not produce good quality films.

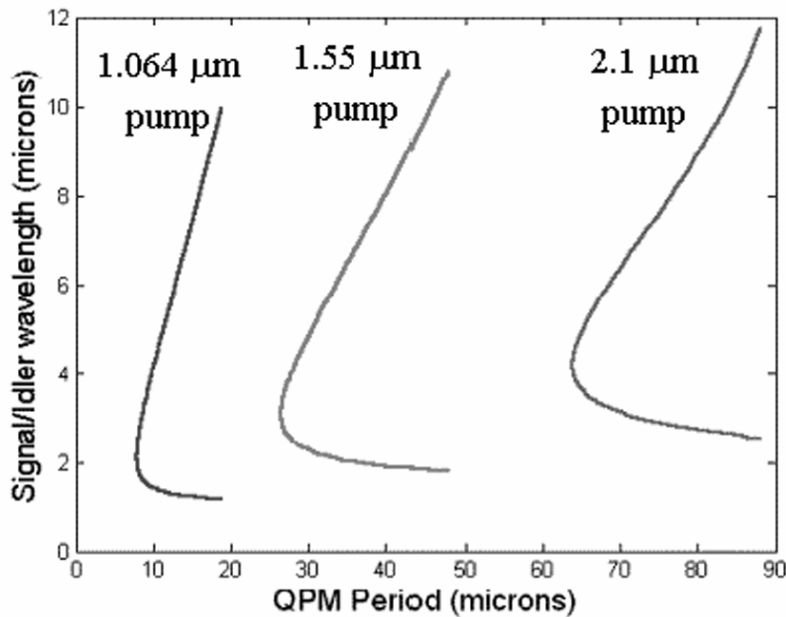


Figure 4.3: Signal/idler wavelength vs. QPM period for nonlinear interactions pumped at 1.064, 1.55 and 2.1 μm . The QPM period gets shorter with shorter pump wavelength.

On the templates used for the 500 μm growth, grating periods ranged from 8 μm (short enough for 1 μm -pumped devices) to above 60 μm (2 μm -pumped devices). Figure 4.3 shows the signal and idler wavelength versus QPM period for DFG or OPO types of interactions with pumps at 1.064, 1.55 and 2.1 μm . The different gratings we put on the mask provide enough data points to quantitatively describe the growth results as a function of domain width. These gratings were either 1 or 2 cm long, and 5mm wide, so

that beams can be easily focused through them and that the conversion efficiencies are sufficient to possibly obtain parametric oscillation.

After the thick growth, the wafers were diced into individual grating samples and some of them had one of their sides polished so that we could observe the propagation of the domains throughout the films. Polishing was not enough to reveal the structure of the films, so we had to use a stain-etching process to clearly show the domains of opposite orientation. We used 1:1:100 $\text{NH}_3\text{OH}:\text{H}_2\text{O}_2:\text{H}_2\text{O}$, because it etches different orientations of GaAs at different rates, thus creating a corrugation on the sidewalls that can be seen in the optical microscope.

Figure 4.4 shows complete cross-sections obtained by the method described above, for 1 cm long gratings with 60, 15.4 and 8.6 μm periods. The best results are obtained for the sample with a 60 μm period, shown in 4.4a. In this picture, we can see that most of the domains grow completely vertically throughout the film, with no change in duty cycle. Figure 4.5 is a close-up of the same cross-section, confirming that the domain boundaries do not have significant deviations from the vertical direction.

On this sample, the average thickness is 471 μm , close to the 500 we wanted. The top surface appears very rough on the long cross-section picture (4.4a), but this is damage caused by the polishing process and the close-up in 4.5 shows what the top surface morphology really looks like. Another important fact to note here is that there are no apparent effects of growth interruptions, even though the grower stopped the growth and took the sample out at least three times for observation and reloading of the Ga source.

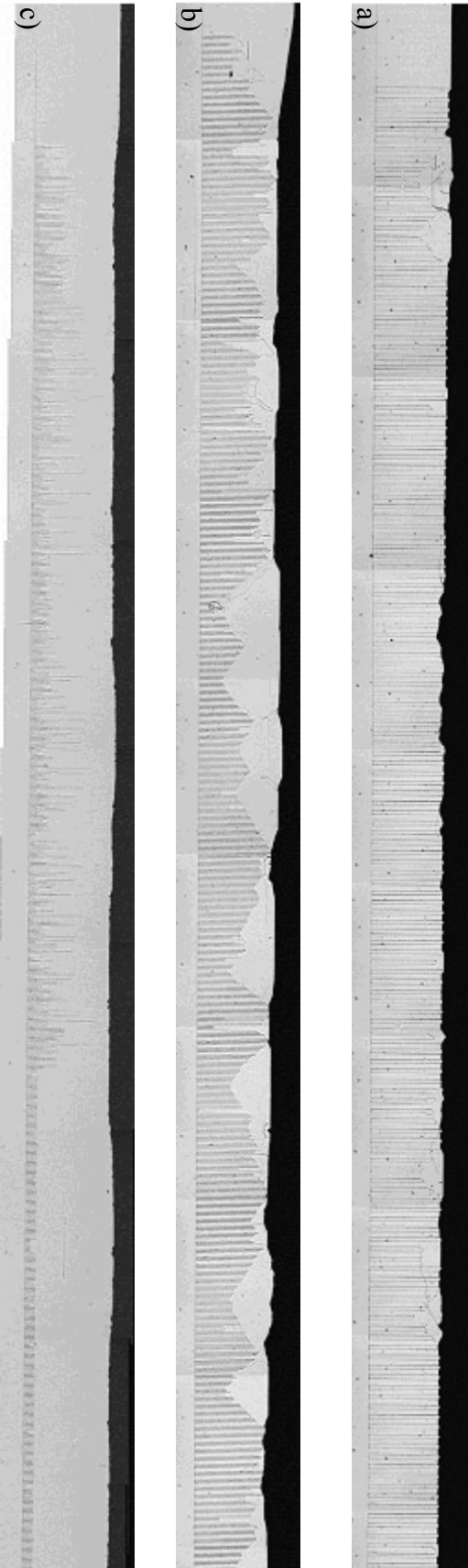


Figure 4.4: Stain-etched cross sections of thick OP-GaAs films, for a) 60 μm period, b) 15.4 μm period, and c) 8.6 μm period. The vertical propagation of the antiphase domains clearly gets worse as the period is reduced, which is correlated to worsening quality of the orientation template with decreasing QPM period.

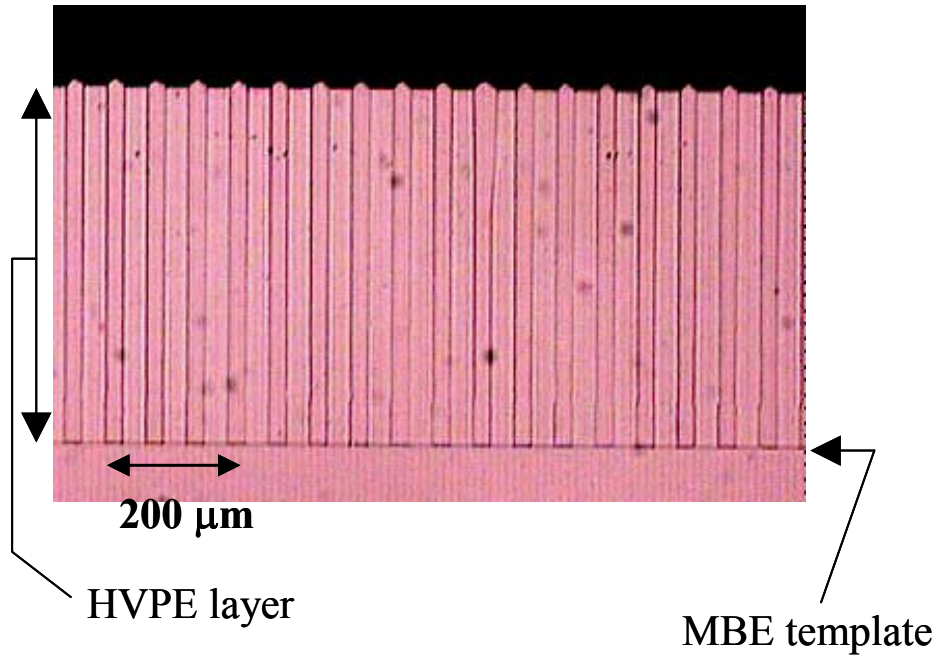


Figure 4.5: Close-up of the stain-etched cross section of the QPM grating with 60 μm period.

Figures 4.4b and 4.4c clearly show that as the domain width decreases, more and more domains do not propagate all the way to the surface. In the sample with 15.4 μm period, the average height is 379 μm , with still many domains propagating all the way to the top, as confirmed in figure 4.6a. In the sample with 8.6 μm domain period, the average domain height is 105 μm , with none of the inverted domains making it to the top of the layer (see also figure 4.6b). Figure 4.4b shows evidence that a growth interruption might have had an effect on the epitaxial process, as most domains seem to propagate at least a third of the way through the layer before any closes over. In figure 4.4c, however, the height distribution seems very random and no apparent effect of growths interruptions is visible.

From these observations, it seems that there is a clear relationship between template quality and vertical domain propagation in HVPE. As we saw in chapter 3, when the domain width decreases, the density of pits along the boundaries between domains increases on the template, along with a general grating quality worsening. Consequently, the height of inverted domains decreases in the HVPE grown material.

Additionally, it seems as if an uninterrupted growth would reduce the domain interruptions occurrence, at least for domain period down to $15.4\ \mu\text{m}$.

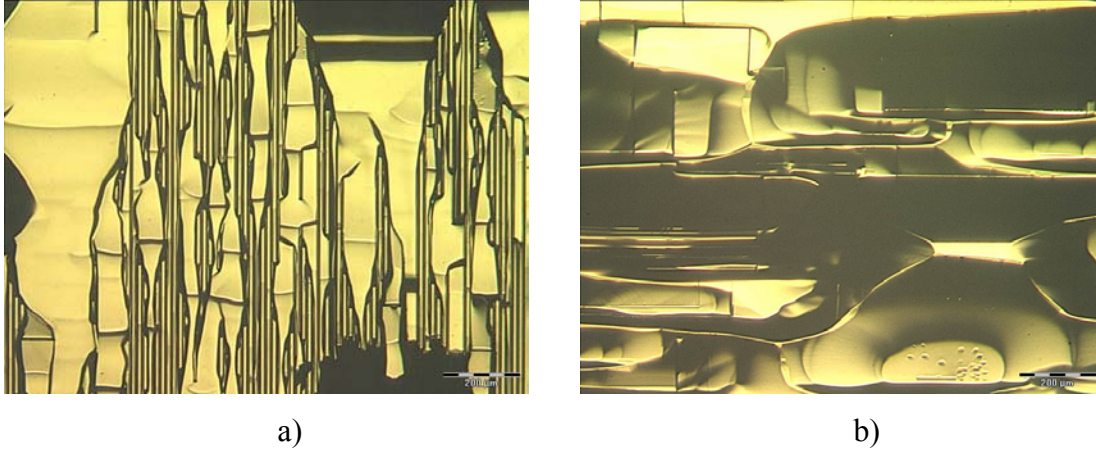


Figure 4.6: Optical microscope pictures of the top of the samples with a) 15.4 and b) $8.6\ \mu\text{m}$ periods. Some domains still propagate all the way to the top in a), while almost none make it in b).

Following these remarks, I will focus now of the sample with $60\ \mu\text{m}$ period, because we can say that the original template was good enough that the results on this sample are really characteristic the HVPE growth process, rather than be completely dependent on the quality of the template. First, we can say that the growth conditions chosen for the HVPE growth clearly favor the vertical propagation of the antiphase domains and the conservation of the QPM grating. We will see later how we can relate this to recent results by the French grower.

Let us now take a look at the top surface of this sample. Figure 4.7 shows the entire surface of the $1\ \text{cm} \times 5\ \text{mm}$ grating through an optical microscope. From this view, we can classify two different types of defects. The first one is the single domain interruption, which we observed in our previous growth try[47,58], and originates at the template, likely from a lithographic defect, a defect in the MBE-grown film, or contamination during the chemical processing. The second type of defect is a pyramidal-shaped nucleation occurring at apparently random depths, since all have different sizes on the top surface. Additionally, these 3-D pyramidal shapes also appear in the unpatterned areas outside of the gratings. The reason for these random defects is not understood at

this time, but it seems to be connected to the HVPE growth process itself rather than a problem with the templates.

The coverage of the surface with intact QPM grating is about 80%, which means an even higher percentage of domains is intact in the middle of the layer, making this sample very useful for actual nonlinear optical experiments. In samples with shorter pitch gratings, the coverage is lower, however, even down to $15.4\ \mu\text{m}$ domain period, the cross-section reveals that if beams are focused in the lower half of the layer, a large percentage of the domains will be useful for nonlinear optics. We should mention here that less than perfect coverage is not a catastrophic problem, only resulting in slightly reduced conversion efficiency.

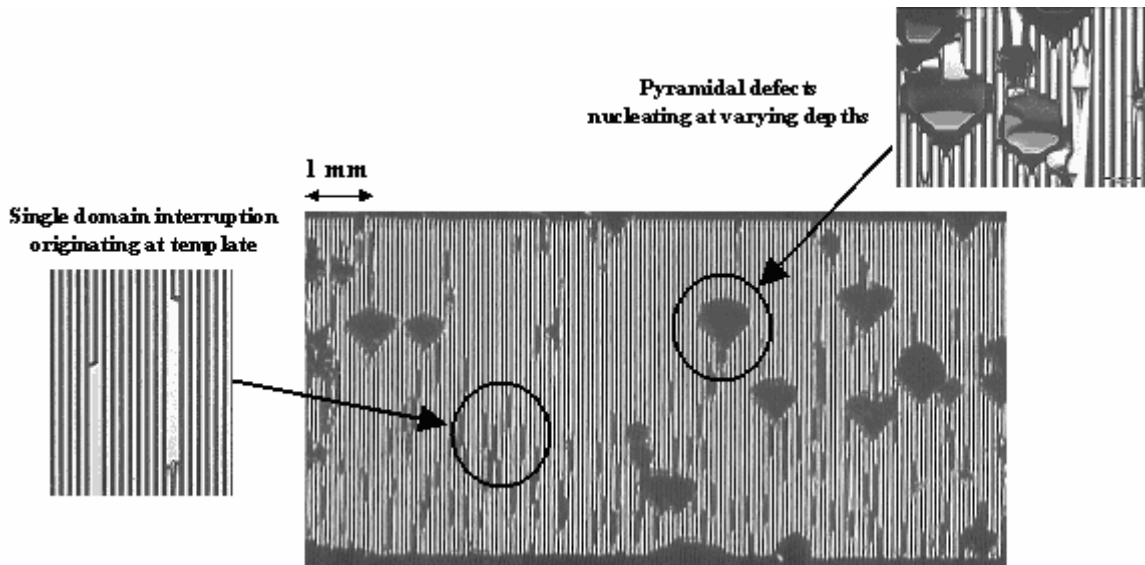


Figure 4.7: Top view of the $60\ \mu\text{m}$ period sample, showing both types of defects appearing on the HVPE grown thick films: single domain interruptions, and random pyramidal growths.

4.2.2 *Selective area growth results applied to antiphase domain behavior*

It is useful to examine more closely the morphology of the thick films to try to understand the growth process that conserves the QPM period and makes the domain boundaries propagate vertically. As mentioned earlier, recent experiments on selective-area HVPE growth of GaAs can help interpret observations of the OP-GaAs films[59]. In these experiments, under various growth conditions (in particular III-V ratio) the

morphology of stripes grown along both $[011]$ and $[01\bar{1}]$ is explained by the hierarchy of growth rates on different crystal planes. In the growth conditions used for the thick films studied in this paper, the distribution of crystal planes, from highest growth rate to lowest, is as follows: $(111)_{\text{Ga}} > (100) > (011) > (111)_{\text{As}}$. Figure 4.8 illustrates the kinds of morphologies observed in this case. We want to compare this with the results of the HVPE growth on our orientation template.

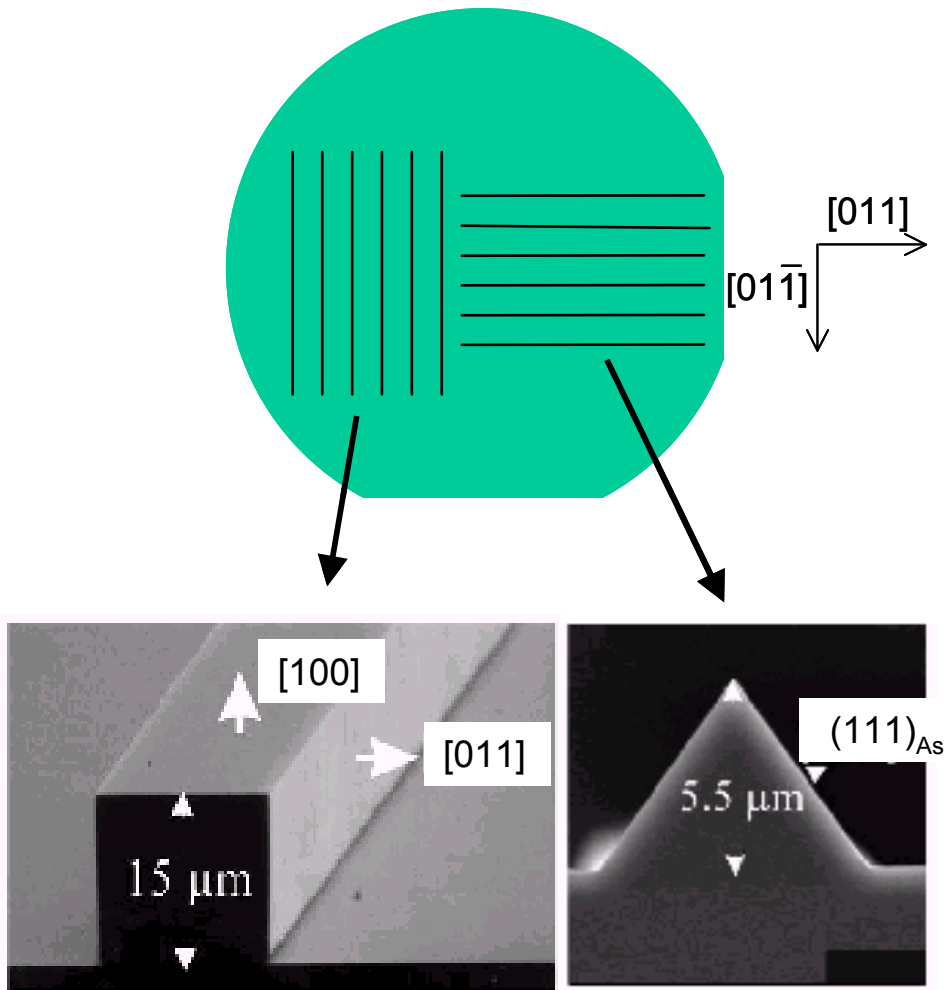


Figure 4.8: Morphologies of selective area growth with HVPE on stripes opened in a silicon nitride mask, using similar growth conditions to those used for our thick OP-GaAs films[59].

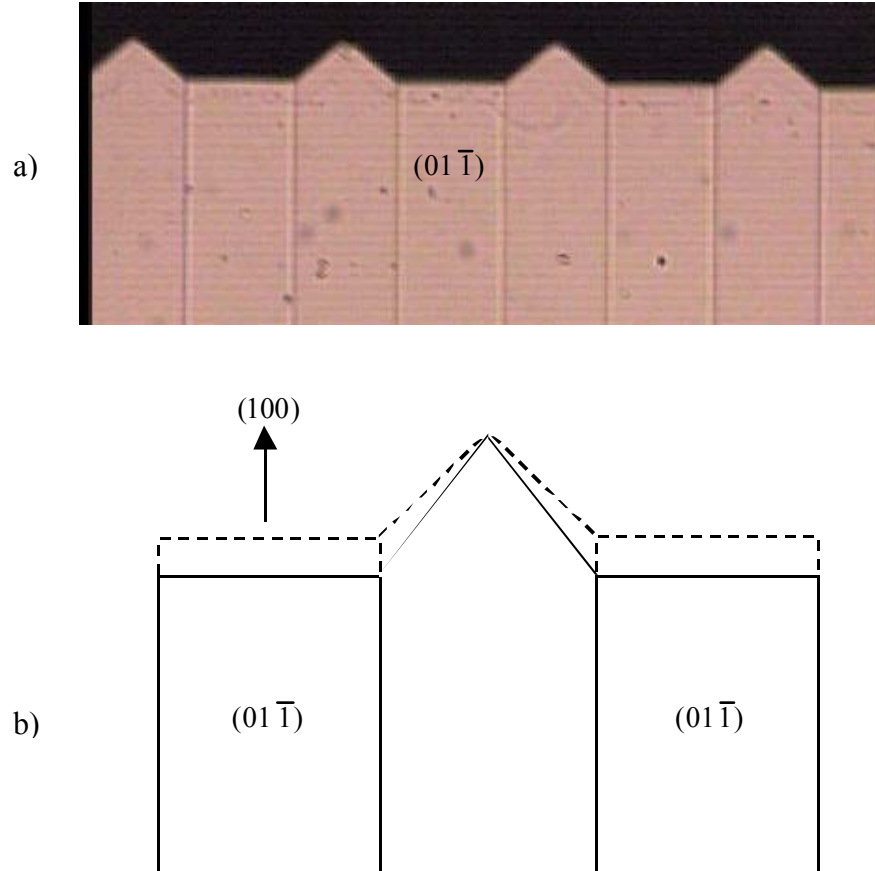


Figure 4.9: The morphology of the surface of the thick OP-GaAs film can help understand the growth mechanism. a) shows a close-up optical microscope view of the top surface of the 60 μm period QPM grating, with clear evidence of two different types of surface behavior depending on the domain orientation. b) is an attempted explanation of the growth mechanism, where the growth rate is coupled in both domain orientation across the antiphase boundaries.

Figure 4.9a shows a close up optical microscope picture of the top of the thick film for a 60 μm period QPM grating. Flat surfaces characterize the domains with the substrate orientation ($[01\bar{1}]$ oriented stripes), while the domains with rotated orientation ($[011]$ oriented stripes) have angled facets at the surface of the film. This seems to correspond very well to the observations in [59]. However, the authors observed a large difference in growth rates between the two perpendicular directions, which is not accounted for in our samples. This suggests a mechanism such as the one described in figure 4.9b. As the (100) surface grows in the $[01\bar{1}]$ oriented stripes, the domain next to it is lagging behind. We propose that additional nucleation sites appear on the side (011)

walls of these stripes, leading to enhanced growth up the angled slopes of the [011] oriented stripes. This results in a coupling of the growth rates across the antiphase boundaries for domains of both orientations. Large disruptions at the antiphase boundaries on the template likely disrupt this process and in particular result in short period gratings of very bad quality.

4.3 Attenuation coefficient measurements in thick OP-GaAs films

After looking at the thick films qualitatively and determining their morphology and defects, we moved on to characterize their optical properties. The first thing to do was to look at linear optical properties, such as attenuation at different wavelengths. This is very important to know as it influences greatly the design of nonlinear optical devices, in particular the choice of pump wavelength and the final performance (for instance if one can reach OPO threshold or not). For a detailed study of these concerns, I refer the reader to Eyres[47].

Optical loss in GaAs comes from multiple sources, coming into play at different wavelengths[60]. At short wavelengths right above the bandgap, the intrinsic Urbach edge, resulting from phonon-assisted interband absorption, falls exponentially with decreasing photon energy. At long wavelengths, the main absorption mechanisms are free-carrier and intraband absorption. In between these two extremes, the loss is created by impurities and defects in the crystal.

In commercially available GaAs, such as the Czochralski- or VGF-grown epi-wafers used for this work, typical losses at short wavelengths above the bandgap in the near-IR are on the order of 1 cm^{-1} . The Urbach edge absorption calculated at room temperature predicts an attenuation coefficient of about 10^{-7} cm^{-1} at $1 \text{ }\mu\text{m}$ [61]. Clearly, the absorption in GaAs at near-IR wavelengths is dominated by defects and impurities. We were hoping that HVPE grown material would have much lower attenuation due the improved material purity from this epitaxial technique.

We proceeded to measure attenuation in a 2 cm long piece of the thick OP-GaAs material with a $26.3 \text{ }\mu\text{m}$ period because this period is close to what would be needed for a device pumped at $1.319 \text{ }\mu\text{m}$, and it was of apparently good quality, with most domains

propagating all the way to the top of the film. This sample also had an unpatterned area next to the QPM grating for comparison to the patterned area, to determine if the antiphase boundaries had any effect on the attenuation. Figure 4.10 shows a top view of the sample with a $1.064\ \mu\text{m}$ beam focused through the patterned area.

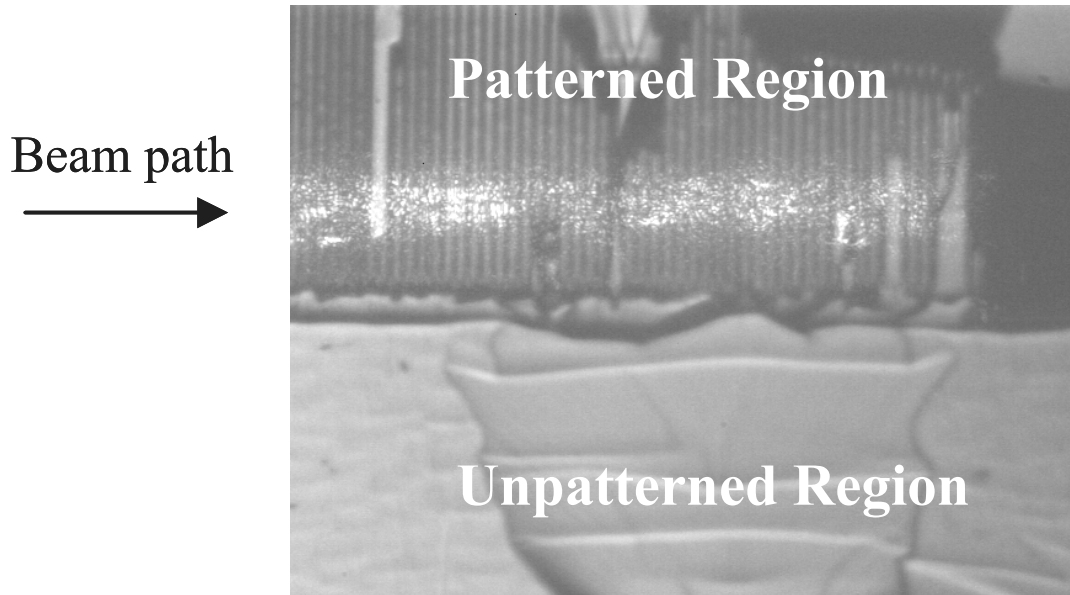


Figure 4.10: Top view of the sample for transmission measurements. The figure shows the $1.064\ \mu\text{m}$ beam focused through the patterned region with a $26.3\ \mu\text{m}$ period. We also used the unpatterned region next to it for comparison.

We also focused beams through the sample at 1.319 and $1.56\ \mu\text{m}$, to get a nice set of near-IR measurements. We corrected the transmission measurements by taking into account multiple Fresnel reflections at normal incidence based on a well-known dispersion model for GaAs[62], then repeated the experiments with end facets polished not to be parallel, so as to eliminate this problem, and found similar results. Table 1 summarizes the attenuation coefficients for both patterned and unpatterned areas as a function of wavelength.

Wavelength (μm)	Attenuation coefficient in patterned region (cm^{-1})	Attenuation coefficient in unpatterned region (cm^{-1})
1.064	0.114	0.071, 0.025
1.319	0.058	0.033
1.56	0.034	0.02

Table 4.1: Attenuation coefficient in patterned and unpatterned regions of the 2 cm long piece with 26.3 μm period QPM grating, at three near-IR wavelengths. The value of 0.025 cm^{-1} for 1.064 μm was inserted as a comparison, and is taken from [47], where attenuation was measured in a 4 mm long, 200 μm thick piece with 212 μm period, which we considered to be unpatterned compared to the sample considered here.

The first remark is that the attenuation coefficient is at least one order of magnitude lower than the 1 cm^{-1} mentioned earlier. This is what we were expecting and is most likely due to the high purity of the epitaxially grown HVPE material. However, the attenuation in the patterned region is consistently higher than in the unpatterned region. At this point, we cannot conclude what the mechanism is for this observation, as it is consistent with either absorption, or scattering from the antiphase boundaries. Further experiments are needed to determine this.

Either way, the attenuation coefficient is already very low and we can use the values measured here for device modeling, at least for devices pumped at 1.32 μm and higher. Pumping at 1.064 μm will require much shorter periods and if indeed the increased loss observed in the patterned region is due to an intrinsic property of the antiphase boundaries, then the attenuation at 1.064 μm for a device designed for that wavelength could be much higher.

We also need to measure losses at longer wavelength to be able to completely determine the performance of the devices built in OP-GaAs. So far, the only measurement we have was done in a 200 μm thick, 4 mm long, sample with a 212 μm period which was designed for CO_2 frequency doubling. This measurement had a lot of uncertainty and gave an upper bound for the loss at 10.6 μm of 0.3 cm^{-1} [47]. Obviously, one will have to more systematically investigate the losses throughout the mid-IR region.

Even though there still remains a lot to improve in the characterization of the linear properties of the material and the samples measured here were from only the third set of thick growth runs on our orientation templates, we can already say that OP-GaAs has very good properties for building devices in thick films, in particular due to the improvement over commercially available bulk GaAs.

4.4 Material characterization using second-harmonic generation

Now that we have studied some linear optical properties of the HVPE-grown OP-GaAs thick films, we decided to move on to performing some nonlinear optical experiments, in particular to determine if OP-GaAs behaves as expected as regards to phasematching and conversion efficiency. One simple way to investigate the nonlinear properties of a material is to use second-harmonic generation, since we only need to focus one beam through the film. In this section, I will report results of second-harmonic generation in some of our thick samples, in particular showing that they have good long-range homogeneity. I will also report results comparing the nonlinear coefficient of GaAs to that of LiNbO₃, which is well known and can be used as a good reference.

4.4.1 SHG setup

None of the gratings on the mask used for the thick HVPE growth were designed originally for SHG experiments. However, it turns out that a set of samples with periods around 60 μm phasematched second harmonic generation from radiation close to 4 μm . Since we did not have a tunable 4 μm source available at Stanford, we started a collaboration with Dr. K. Vodopyanov at Blue Leaf Networks, who let us use his light source.

Figure 4.11 shows the basic setup for the SHG experiments. The light source was a tunable (4-10 μm) ZGP OPO pumped by a 2.8 μm Er,Cr:YSGG laser, at a repetition rate 25 Hz. The OPO signal was tuned around 4 μm to achieve quasi-phasematched SHG. The OPO linewidth at 4 μm was 5.6 nm, the pulse energy ~ 100 mJ, and pulse duration 63 ns. The pulse-to-pulse OPO energy fluctuations were typically 20% and our measurements were generally averaged over 1000 pulses per data point. The signal

polarization was in the plane of the wafer, giving a harmonic polarization perpendicular to the wafer. We used InAs (F1 on figure 4.11) and sapphire (F2) substrates, both at the Brewster angle, to block the unwanted laser (2.8 μm) and OPO idler (8-9 μm) wavelengths respectively.

The OPO beam was close to Gaussian in the far zone. It was focused into a sample by a $f = 50 \text{ mm}$ BaF_2 lens, to get a waist of $w_0 = 48 \pm 2 \mu\text{m}$. A pyroelectric energy meter Moletron J4-09 was used to measured the SHG energy. A thick BK-7 glass substrate (F3) was used to block the fundamental beam (attenuation $>10^4$).

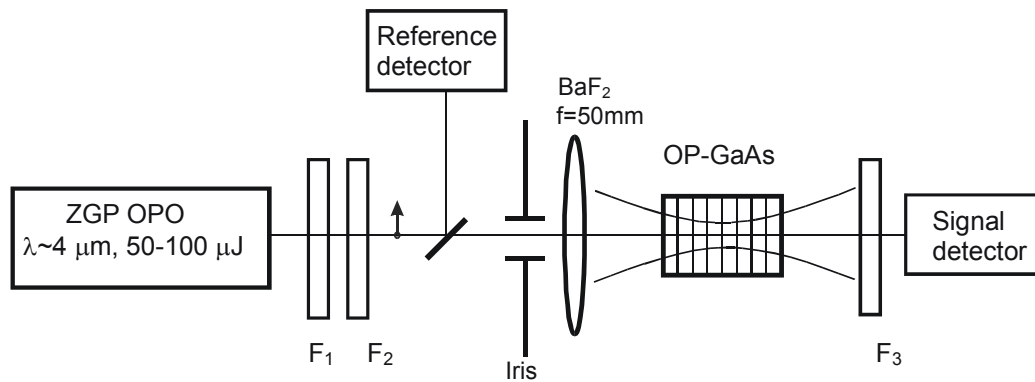


Figure 4.11: Experimental setup for SHG at 4 μm

4.4.2 SHG measurements

We placed samples with three different periods in the setup, and proceeded to measure tuning curves by scanning the signal wavelength of the OPO around 4 μm . The samples we used had periods of 58.8, 59.4, and 61.2 μm respectively, and were either 1 or 2 cm long. We found that all samples produced very good tuning curves. For instance, figure 4.12 shows a typical tuning curve obtained with a 1 cm long piece of the 61.2 μm QPM grating.

For all the samples, the agreement between experiment (dots in figure 4.12) and theory (line) were just as good as that shown in figure 4.12. In particular, the tuning curve width agreed almost perfectly, which means that the QPM gratings have excellent long-range homogeneity, or else we would see a broadening of the curve.

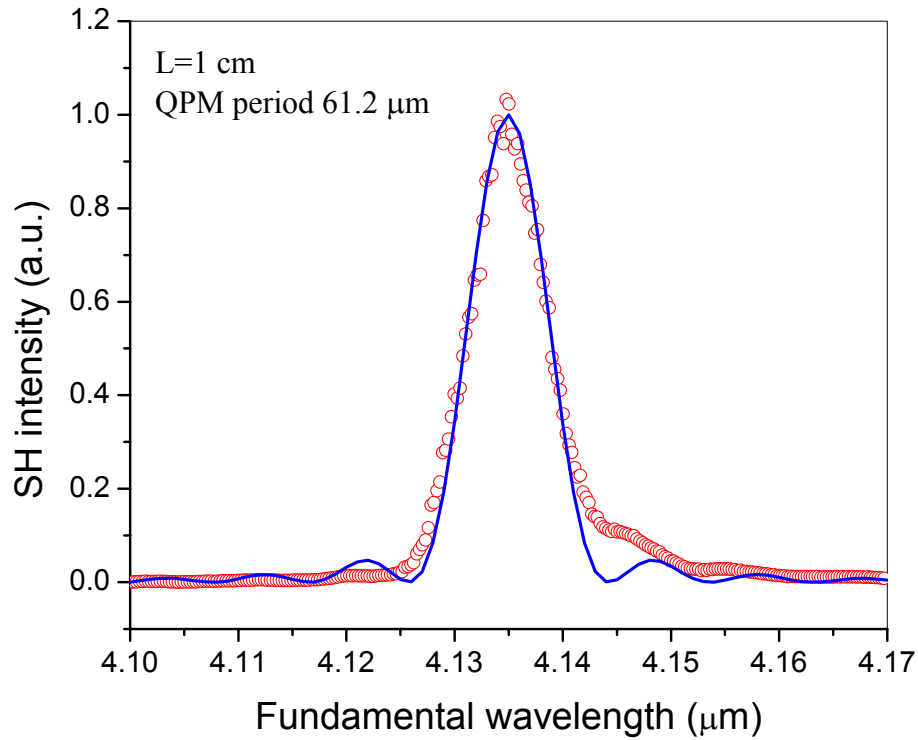


Figure 4.12: Tuning curve for the 4 μm SHG obtained with a 1 cm long, 61.2 μm period grating. The circles are the experimental data, and the line is the theoretical tuning curve based on a well-known dispersion model[62].

Additionally, the positions of the phasematching peak also agree very well with theory, as shown in figure 4.13. One of the concerns when designing the mask was being sure that we were using the right periods for the interactions of interest. If the dispersion model we used[62] was not correct, then we could end up looking for a phasematching peak that does not exist with that particular QPM grating.

It turns out that Pikhtin[62] proposed two different equations for the dispersion modeling of GaAs, but that only one of them matches our data very well, at least for the SHG from 4 μm radiation. Unfortunately, we will see that neither one of his expressions works as well for difference frequency generation.

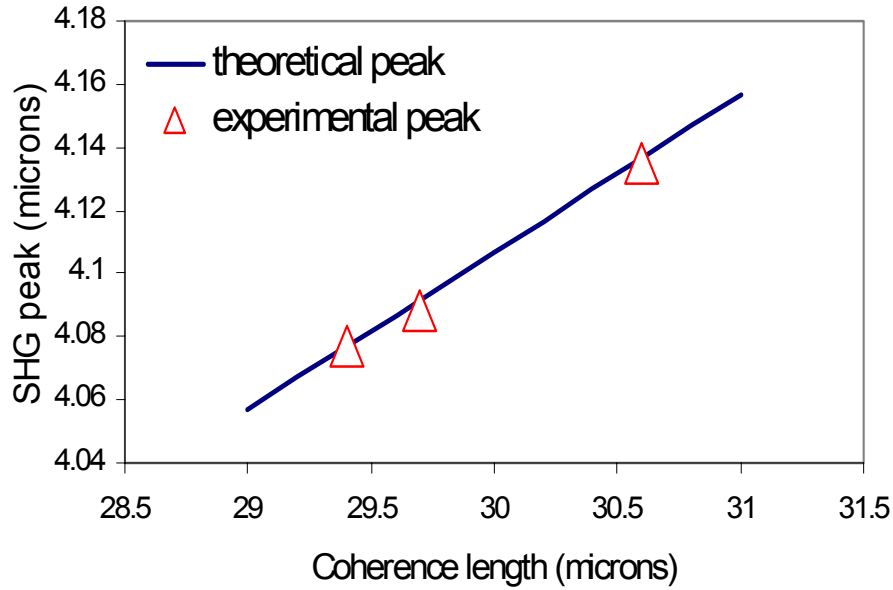


Figure 4.13: Comparison of the SHG phasematching wavelength between experiment and theory, based on Pikhtin[62], for three different grating periods.

From this set of experiments, we can conclude that the thick films of OP-GaAs seem to be close to ideal as far as grating quality and homogeneity of the material. In the next section, I describe how the same setup was used to compare the nonlinear coefficients of GaAs and LiNbO₃, thus allowing us to get a measurement of d_{14} of GaAs.

4.4.3 Measurement of d_{14} of GaAs using SHG at 4 μm

Nonlinear properties of materials are often hard to measure and GaAs is no exception. For instance, the value of d_{14} has been reported with many different results, for various types of interactions[63,64]. Even taking into account Miller's rule for the dispersion of d_{14} , there is a large variation and we would like to get a more accurate measurement of the nonlinear coefficient of GaAs for better device performance prediction.

We decided to compare the nonlinear coefficient of GaAs to that of LiNbO₃, which is known with much better accuracy, by putting in the SHG setup a piece of PPLN with the right period (28 μm) to phasematch SHG at close to the same wavelength as the OP-GaAs sample with 61.2 μm QPM period. Additionally, the PPLN grating length of $L=6.2$ mm was chosen in such a way that $(L/n)_{\text{PPLN}}=(L/n)_{\text{GaAs}}$ (the length of the OP-

GaAs sample was 1 cm), where n is the refractive index. In this manner, the pump fluence distribution was the same inside both crystals, as long as the pump beam waist was in the middle of the respective crystals. We could then compare directly the second harmonic powers, or equivalently, the conversion efficiencies, to extract value of $d_{14}(\text{GaAs})$ as a function of $d_{33}(\text{PPLN})$. We had to slightly temperature tune both crystals to make their phasematching wavelength match.

Figure 4.14 shows our measurement of the external conversion efficiencies for OP-GaAs and PPLN samples in the low conversion limit at a phasematching wavelength of $4.135 \mu\text{m}$. The ratio of the conversion efficiencies was found to be 8.5, with a measurement to measurement error of at most 10 %.

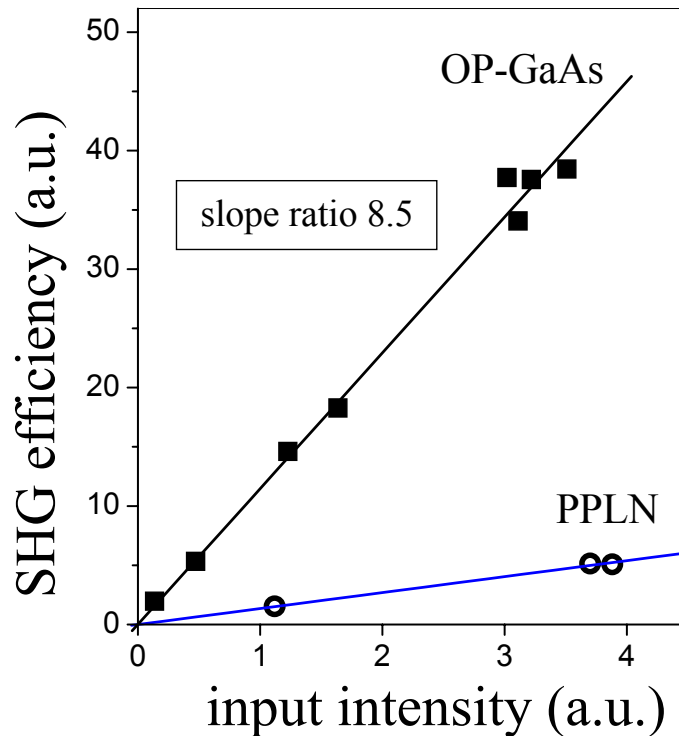


Figure 4.14: SHG efficiency in the low conversion limit vs. pump intensity for OP-GaAs ($L = 1 \text{ cm}$) and PPLN ($L = 6.2 \text{ mm}$) at the phasematching wavelength of $4.135 \mu\text{m}$, with fitted straight lines.

From these measurements, we can back out the ratio of d^2/n^3 for both materials, knowing what corrections have to be applied for various issues such as: different crystal

lengths, different losses at fundamental and harmonic, fraction of missing domains, and the finite linewidth of the OPO signal. Following these corrections, we obtain a ratio of $(d^2/n^3)_{\text{GaAs}} / (d^2/n^3)_{\text{PPLN}} = 6.22 \pm 0.6$. From known dispersion relations[62,65], we can back out $d_{14}(\text{GaAs})/d_{33}(\text{PPLN}) = 5.01 \pm 0.3$ for SHG at about 4.1 μm . Using the widely accepted value of $d_{33}(\text{PPLN}) = 27 \text{ pm/V}$ at 1.06 μm [66] and scaling it, via Miller's rule, to get 18.7 pm/V at 4.1 μm , we obtain a value of the GaAs nonlinear coefficient $d_{14} = 94 \pm 10 \text{ pm/V}$ at 4.1 μm . This result is completely consistent with a frequency doubling experiment performed in a 200 μm thick sample from a previous HVPE growth run with a CO_2 laser. The value extracted from that experiment, $d_{14} = 86 \text{ pm/V}$ at 10.6 μm , scaled with Miller's rule, gives $d_{14} = 92 \text{ pm/V}$ at 4.1 μm , within the measurement error of our result.

The measurement of d_{14} using SHG at 4 μm was carefully executed and we believe that the value we obtained can be used confidently as a reference for device design and performance evaluation. Through the SHG experiments, we managed to learn a lot about the quality of our samples for nonlinear frequency conversion, and can now try to do other experiments with reliable data on the behavior of OP-GaAs.

4.5 Generation of mid-IR radiation by difference-frequency mixing

While SHG certainly was useful in characterizing thick films of OP-GaAs, one of the goals of this project was to show that OP-GaAs can be used in a system designed to generate mid-IR radiation, preferably beyond what PPLN devices are capable of producing. The orientation templates we made have many QPM gratings on them to accomplish just that. Unfortunately, any grating designed for pumping below 1.3 μm was not of good enough quality after the thick growth (see section 4.2).

Even though we were limited in this regard, plenty of samples were left for us to test. In this section, we report the generation of close to 8 μm radiation by difference-frequency generation from two near-IR sources at 1.3 and 1.55 μm . Current efforts are directed at other interactions with the remaining samples and should hopefully see other difference-frequency mixing and OPO experimental results soon.

The sample used for the DFG experiment was the same as that used in the attenuation measurements, in section 4.3. On the top surface, a fraction of the domains (about 10 %) is missing, due to the two types of defects discussed in section 4.2. No significant deviation from the ideal 50% duty cycle of the QPM period was observed in the sample.

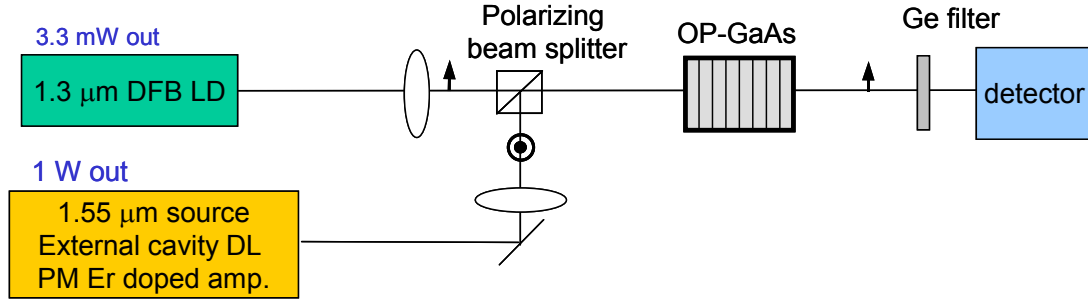


Figure 4.15: Difference-frequency mixing setup for generation of mid-IR radiation

Figure 4.15 shows the experimental setup for the DFG experiment. All the lasers mentioned here are CW. The pump wavelength was provided by a fiber coupled distributed feedback laser, whose output was tuned by temperature from 1306 to 1314 nm. Its power varied with wavelength between about 1.5 and 3.3 mW. The signal beam came from an external cavity diode laser, tunable between 1510 and 1580 nm. It was injected into a polarization-maintaining Erbium-doped fiber amplifier to obtain 1 W of radiation tunable between 1535 and 1570 nm. The pump beam was polarized parallel to the sample surface, the signal perpendicular. We can note here that due to the symmetry to the nonlinear tensor of GaAs, the signal beam did not need to be polarized in any particular direction, and that a randomly polarized signal beam should in theory result in the same conversion efficiency and idler output power. That being said, in our experimental configuration, the idler will end up being polarized in the same direction as the pump beam.

Both pump and signal were focused through lenses to have their waist in the middle of the sample and they were combined with a polarizing beam splitter. Their waists were measured to be $w_0 = 130 \pm 5$ and $290 \pm 5 \mu\text{m}$ for the pump and signal

respectively. The generated idler was collected by ZnSe lenses and measured by an MCT detector. A Ge plate was used to filter out the near-IR beams.

Figure 4.16 shows the normalized tuning curve measured by setting the pump wavelength at 1307 nm and scanning the signal wavelength. The theoretical calculation, using the dispersion model by Pikhtin[62], has been shifted to make the theoretical and experimental phasematching peaks coincide. Phasematching occurs at a signal wavelength of 1567 nm, resulting in an idler of 7.905 μm . Even though the phasematching does not agree with theory, the tuning curve width is in very good agreement with calculations, once again showing the good homogeneity of the material.

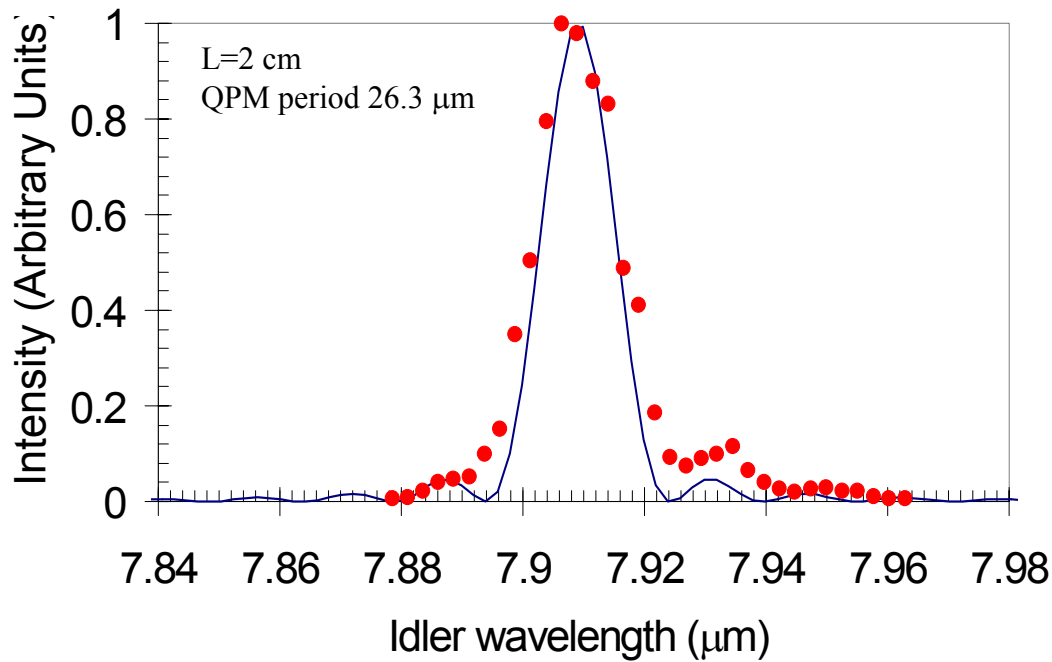


Figure 4.16: Normalized tuning curve for the generation of mid-IR generation by difference-frequency mixing from a pump at 1307 nm and tunable signal around 1560 nm. The points indicate the experimental data, and the curve is a theoretical calculation whose peak has been shifted to match the measurement.

We measured the peak idler power, at phasematching, to be 38 nW. This is definitely very low and unusable for real-life applications, but it is completely due to the low powers available at the input wavelengths and was sufficient for this demonstration. The idler power scales linearly with the pump and signal power, so one can easily think of obtaining much higher idler power with more pump and signal power. Taking into

account many other effects such as Fresnel reflections at the sample facets and missing domains, and using the value of d_{14} obtained in section 4.4 scaled with Miller's rule, the measured value is still close to a factor of 3 less than theoretically predicted. Many reasons can be found for this discrepancy, including less than ideal focusing conditions, higher-than-predicted losses from all the optics in the paths of the various beams, but for such an unoptimized experiment, being within an order of magnitude of expected power is definitely a good result.

The disagreement in the position of the phasematching peak is worrisome though and has led us to currently investigate the existing GaAs dispersion models and try to come up with a better model, or at least empirical expression, which will better match our observations and help design devices in the future. Recent results [71] appear to rectify the problems with Pikhtin's dispersion data.

4.6 Conclusion

In this chapter we showed that it is possible to fabricate high-quality thick OP-GaAs films suitable for nonlinear frequency conversion applications using an all-epitaxial approach. Even though this technology is still in its early stages, it is already capable of producing films with large enough apertures (0.5 mm), very low attenuation and with good enough homogeneity that they can compare favorably to current PPLN crystals.

We used second harmonic generation to show the good quality of the films in a nonlinear optical frequency conversion setting, and also to measure the nonlinear coefficient of GaAs accurately.

Finally, we demonstrated generation of close to 8 μm radiation by difference-frequency mixing of two near-IR sources. This represents the first demonstration of mid-IR generation from all-epitaxially grown OP-GaAs, and as such, should be seen as just a stepping stone towards building real systems with this material. The good agreement between expected theoretical behavior and performance of these devices and actual experimental results shows that already in its early stage, OP-GaAs is close to fulfilling its promise as a very attractive choice as a mid-IR nonlinear material compared to other nonlinear materials such as ZnGeP_2 and AgGaSe_2 .

There still remain of course many improvements to make, in particular in the direction of improving the orientation template so that we can get thick films with periods short enough for 1- μm -pumped devices. Also, increasing the thickness to 1 mm would be desirable for high-power applications. Current work is ongoing to try to solve these issues and demonstrate other nonlinear interactions.

CHAPTER 5: QPM AlGaAs WAVEGUIDE DEVICES FOR COMMUNICATION APPLICATIONS

While the previous chapter focused on thick films of HVPE-grown GaAs for bulk-like optics, we also are interested in another family of devices, using a waveguide configuration. These each address different applications. For instance, the thick-film devices are more suited to high power, while waveguides will usually provide very high conversion efficiencies, but with lower powers. Waveguide devices can be designed for many types of interactions, since the AlGaAs transparency range goes from the visible to the mid-IR. Originally, this project started with the idea of making highly efficient frequency converters in waveguides to generate mid-IR from near-IR sources. However, it turns out that building a waveguide device for long wavelengths makes it highly multimoded for the near-IR wavelengths. Coupling into the fundamental modes for these short wavelengths is a very difficult issue to solve in the AlGaAs system with epitaxial techniques. While we are still interested in making such a device, we decided to investigate waveguide devices for communication applications first, where the wavelengths of interest are all in the near-IR, making the design easier. First, I will start by describing the type of device we want to build and the kind of nonlinear interaction in which we are interested, then I will discuss the design restrictions that we adopted and the tool we used to model our waveguides. Finally, I will go over the fabrication issues, show some nonlinear optical results, and discuss the current issues with the guides as well as ways to overcome them.

5.1 AlGaAs waveguides for optical communication applications

Over recent years, with the explosion of data traffic over communication networks, has come the introduction of newer technologies to deal with this increase. Current networks are using more and more channels in a wavelength-division multiplexing (WDM) scheme, and/or increasing the data rate of individual channels. In either case, dynamic control of the data flow (routing, channel shifting, bandwidth monitoring and utilization)

is becoming more and more of an issue, because so far all, of this has been accomplished by optical to electrical to optical conversion. If one was able to rely on all-optical devices for these operations, there could be a potential release of this bottleneck and great improvement in how the networks operate.

Frequency converters could be one such device, because they allow many functions all-optically. For instance, they can shift one channel to another through difference-frequency mixing, they can be used in TDM systems as all-optical gates, or they can also be used as dispersion compensation devices because difference-frequency mixing generates the complex conjugate field from the input signal (figure 5.1).

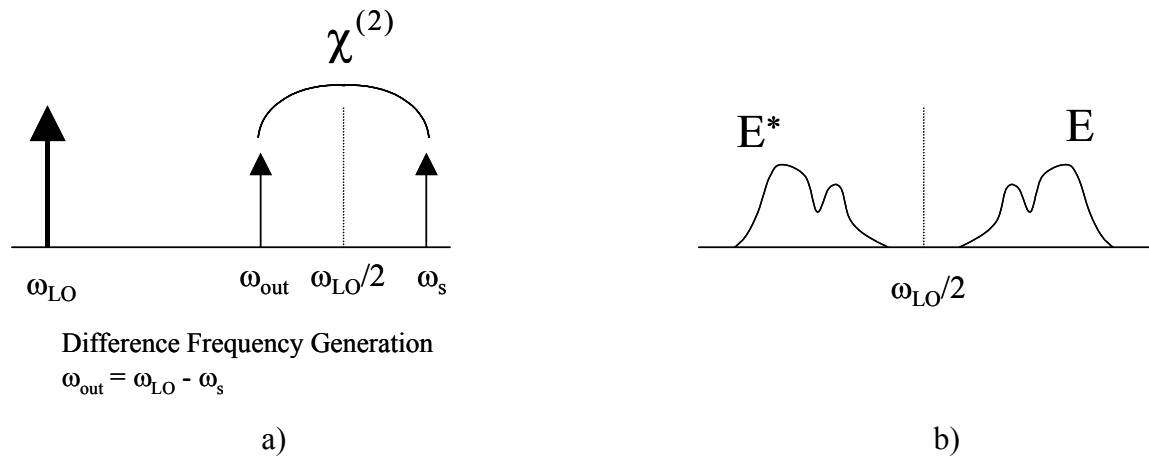


Figure 5.1: Configuration used in frequency converters for optical communication applications. a) shows how such a device could be used for channel shifting, where ω_s is the frequency for a WDM channel around 1550 nm, ω_{LO} is the pump frequency around 775 nm, and the output by difference-frequency mixing is ω_{out} , another WDM channel. b) shows that the difference-frequency mixing output field is the complex conjugate of the input one, which could be useful in dispersion compensation.

Such devices have already been successfully demonstrated in PPLN waveguides. Examples of recent results include all-optical WDM channel shifting[14], dispersion compensation by mid-span spectral inversion[16], and time-division multiplexing[67]. Why would we want to use semiconductor waveguides instead of PPLN, knowing the success this material has already had? For one, because of the higher nonlinear coefficient of AlGaAs, devices built with this material could potentially function with much lower pump powers, more suitable for current communication components than

PPLN. The other interesting thing about AlGaAs is that due to the symmetry of the nonlinear tensor, if the pump polarization is chosen carefully, then the device performance becomes completely independent of the polarization of the incoming signal[68].

Such waveguide devices have been fabricated before, using MOCVD regrowth on a diffusion-bonded orientation template. Both SHG[28] and DFG[69] experiments were performed, despite less than ideal performance. While the waveguides we built and will be discussing in this chapter do not for now improve on these results, there is reason to believe that our technology of all-epitaxial fabrication has the potential to overcome these problems and make these devices very competitive with the PPLN devices.

5.2 Waveguide design and fabrication

In this section I will be discussing the many design considerations and trade-offs we had to make. I will first describe the main goals we wanted to achieve when we set off to design these devices, then I will show the tools we used to model the waveguides, as well as report many parametric studies used in the design process. Finally, I will discuss the fabrication of the waveguides.

5.2.1 Design considerations

Previous work on fabricating waveguides on our orientation templates[46,47], led to very inconclusive results about what the issues were with those waveguides, in particular because they used a design taken from earlier literature[28], without examining its strengths and weaknesses. For this work, we decided to start from scratch and develop our own design, with a few considerations in mind.

First of all, because we used MBE for the growth, we could not use a buried waveguide design, as Yoo and coworkers eventually used[28]. This led us to use a ridge waveguide design. The basic features of the waveguides are shown in figure 5.2.

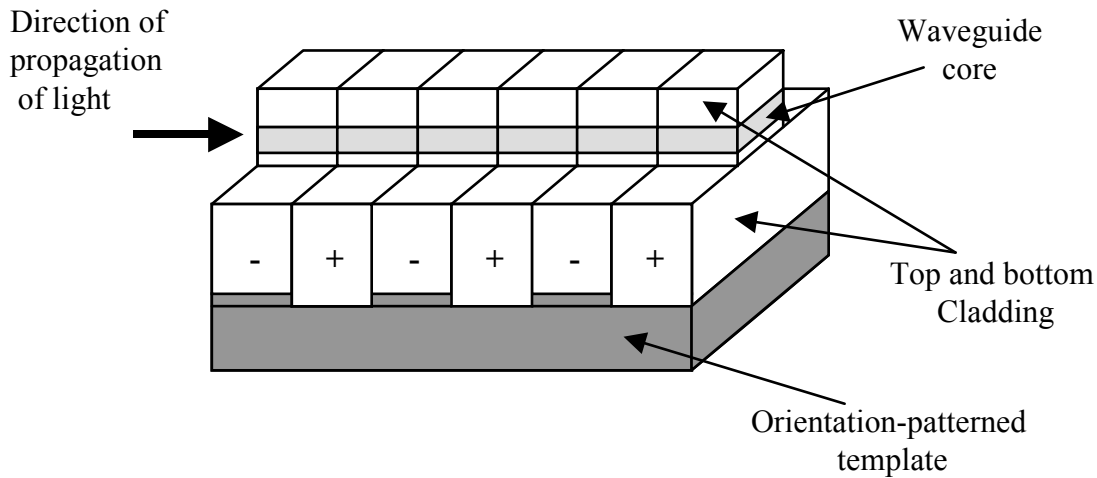


Figure 5.2: Schematic of the basic structure of our AlGaAs waveguides.

The waveguides obviously had to be transparent at the pump wavelength, around 775 nm, which means that we had to use at least 50 % Al in our AlGaAs layers. Too high of an Al composition makes AlGaAs susceptible to oxidation in air and lack of stability, so we decided to limit ourselves to about 70 % Al. For high conversion efficiencies, the waveguides also had to be single mode at 1550 nm, and have low losses. Another important factor was that we could easily launch a mode in the waveguide and so we had to try making it symmetrical. Finally, the last design consideration had to be ease of fabrication, so that we would not introduce extra errors and make our devices miss the phasematching conditions we wanted.

Instead of just trying to get the highest possible conversion efficiency, we decided to try and make our waveguides very robust in terms of all the possible variations during the fabrication process. This would guarantee that we would observe frequency conversion close to where we expected the phasematching to occur. The types of fabrication miscues we expected were, for instance, variation of the waveguide width along its length, variations in the composition of the layers due to MBE uniformity problems, both of which would lead to a change in the phasematching conditions.

Considering all these factors, we had to find a tool that we could use to calculate the modes of the waveguides and study the behavior of the phasematching condition and conversion efficiency as a function of the changes in the parameters described above.

5.2.3 *Waveguide mode solver*

Instead of relying on commercial software for solving for the modes of our waveguides, we decided to instead develop our own code, so that we could modify it at will and in particular get it to perform parametric studies. Since our guides are very simple, we did not require very advanced mode solvers. We settled on a technique described in a paper by Stern[70], using the finite-difference method to solve for the modes of the waveguide.

In this approach, we solve for quasi-TE and quasi-TM modes, transforming a vectorial problem into a scalar problem. For this reason, this approach is called semi-vectorial polarized difference method. Once we have written a scalar equation for each polarization, we take the usual five-point difference scheme to convert the differential equation into an algebraic eigenvalue problem. We implemented this code using Matlab, which possesses very powerful tools for solving this type of eigenvalue problem.

Our code was compared to commercial software such as Fimmwave, from Photon Design Inc., and our results for effective mode indices matched those of Fimmwave to a precision of 10^{-4} , which we deemed very satisfying, considering that uncertainty in the fabrication process corresponds to a larger value than that.

We started with a basic version of the mode solver, where an input file contained the list of layers present in the structure, the width and the depth of the ridge. The basic structure that the code solves for is shown in figure 5.3. Additionally, the input file also contains the definition of the mesh for the finite difference method. The code allows for straight, sloped or curved sidewalls, with the resolution limited by that of the mesh. The user then inputs the wavelength, what type of mode to solve for (TE or TM) and what kinds of boundary conditions to use on the edge of the mesh.

The code then generates an index mesh, such as that shown in figure 5.4 and uses that to create the matrix for the eigenvalue problem. Matlab can solve for this and give as many solutions as wanted. The code is capable of displaying the mode profiles, as shown in the examples in figure 5.5.

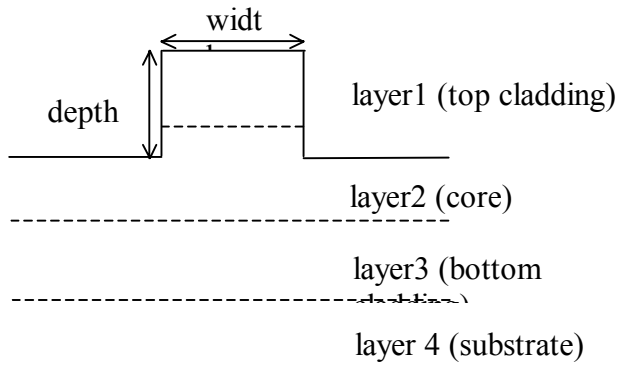


Figure 5.3: Basic ridge waveguide structure input into the waveguide mode solver

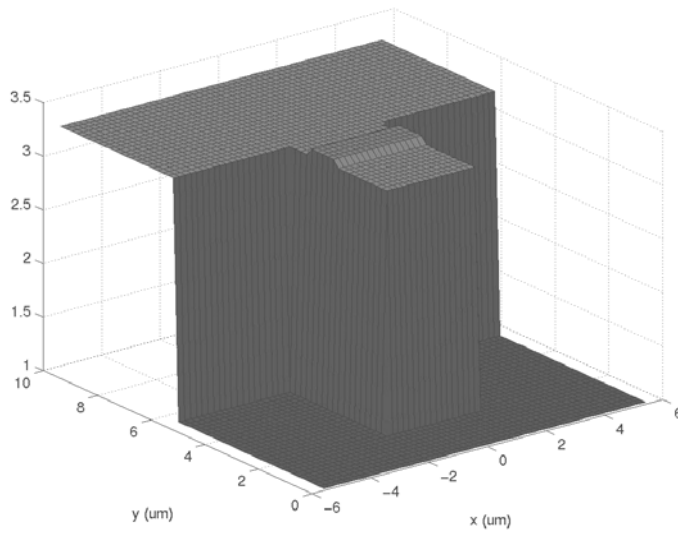


Figure 5.4: Index mesh generated by the mode solver.

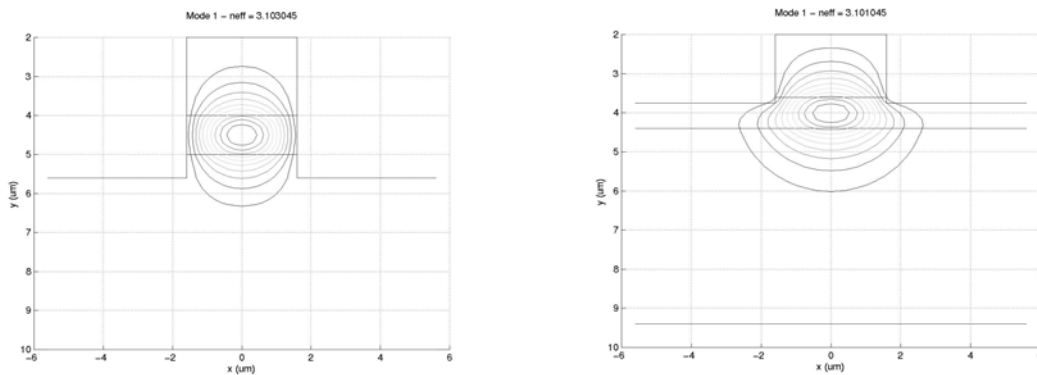


Figure 5.5: Examples of mode profiles obtained with the mode solver from earlier tests.

The results of the solver can be used to calculate coupling efficiency from a known beam or overlap integrals for conversion efficiency, as well as, of course, the phasematching condition using the effective indices.

While this first version of the code is very helpful, we used the vector and matrix handling capabilities of Matlab to develop a second version where multiple calculations can be performed in a row as a function of a given parameter. In the following section, I discuss the various parameters used for the optimization and show the final design we settled on as a result of the many trade-offs we had to face.

5.2.4 Parametric analysis of waveguide design

We had to choose a set of parameters to optimize to get a reasonable design. We decided to use the following values:

- The normalized effective index of the first supported mode, defined as follows:

$$b_1 = \frac{n_1^2 - n_s^2}{n_f^2 - n_s^2} \quad (5.1)$$

where n_1 is the effective index of the first supported mode and n_s and n_f are respectively the lower cladding and core refractive index (at the wavelength of interest). b_1 is always smaller than 1, and a negative value indicates a non-guided mode. So, in general, it has to be as high as possible.

- The normalized effective index of the second supported mode, given by:

$$b_2 = \frac{n_s^2 - n_2^2}{n_s^2} \quad (5.2)$$

and b_2 is defined in a slightly different way because we usually want single-mode waveguides, which means $n_2 < n_s$. If b_2 were defined in the same way as b_1 , it would be most of the times a negative number. Defining it in this way, we will always deal with positive numbers, smaller than one. Moreover, we wish values of both b_1 and b_2 as high as possible (that means first mode more guided and second mode more “unguided”) and negative values represent undesired cases (no supported modes or multi-mode waveguides). We point out that the normalized effective indexes are figures of interest only for the 1550 nm wave.

- The overlap integral between the modes. To simplify our study, we will focus only on SHG from a 1550 nm beam, and so only the overlap integral of the 1550 nm and 775 nm modes is necessary.

- The aspect ratio of the first supported mode:

$$shape = \frac{w_x}{w_y} \quad (5.3)$$

where the w_x and w_y are the widths of the electric field at $1/e$ of its peak value in the x and y directions. This value gives an indication of the ellipticity of the mode and is useful in determining if we will be able to efficiently couple into the waveguide.

Now that we have chosen some values to optimize, we decided to try and run parametric simulations as a function of waveguide width, because this is an important parameter that we can control easily during fabrication. However it can also lead to missing the phasematching condition. Trying to optimize these values as a function of the width is what we are going to try to do, and the following is a summary of our studies. Keep in mind that the parameter space we explore is very vast and that there might be other combinations that will give similar or superior performance.

We started with a design similar to that used in Eyres[47], with 60% Al claddings and a 1 μm thick 50% Al core, with a 1 μm high ridge. The first thing we had to settle was the composition of the waveguide layers. Any Al composition between 50 and 70 % is possible. Additionally, the index contrast between the core and cladding is also an important issue. From figure 5.6, we see that only the difference Δx in Al composition is important, apart from the fact that a higher Al composition apparently gives a larger overlap integral, thus higher conversion efficiency. So we just set the cladding composition to 70 % and varied the core composition.

When Δx is too large, only the 6 μm wide guides are single mode. While they provide higher efficiencies, they are also more difficult to fabricate, so we settled on a core Al composition of 67 % and a nominal width of 8 μm .

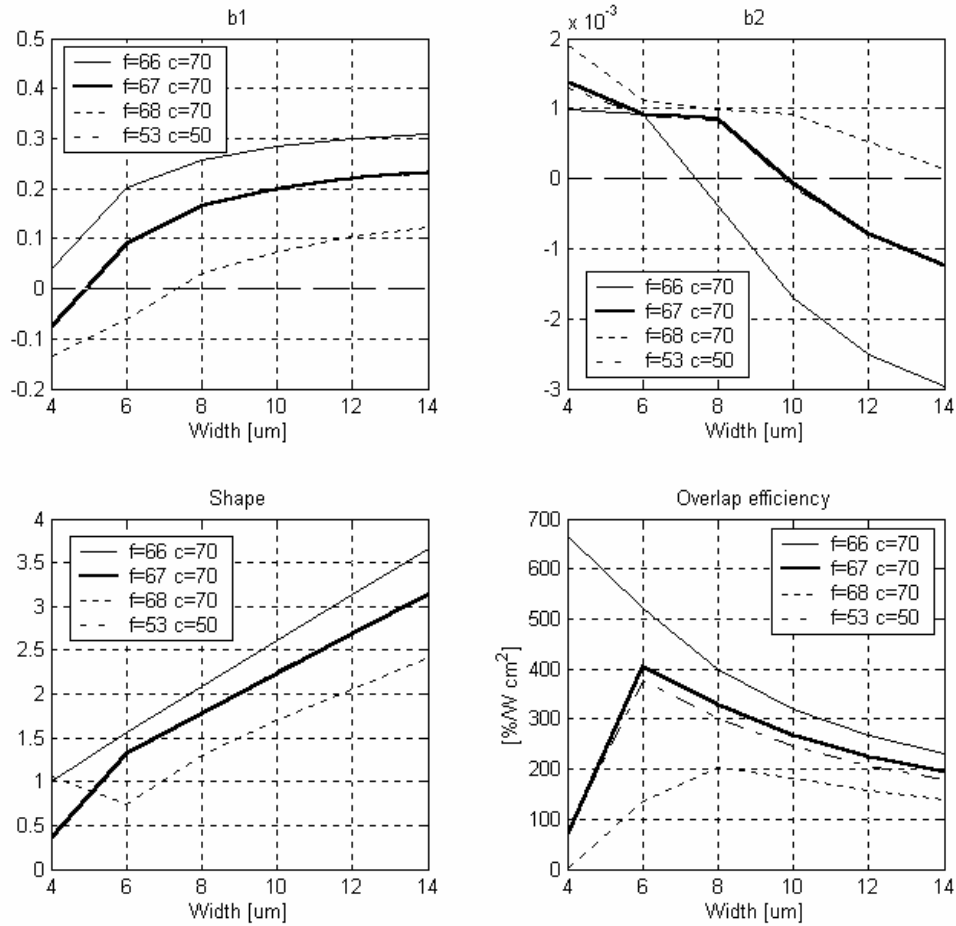


Figure 5.6: Parameter analysis as function of width for an almost symmetrical waveguide with 1 μm core, for different core/cladding composition combinations.

Once we start changing the core/cladding compositions, we also have to look at the core thickness to make sure that it is optimal. In fact, if the core is too thick, it would allow other modes to be supported and when too thin, it would suppress also the fundamental mode, due to the fact that our guides are not completely symmetrical in the vertical direction, which results in the existence of a cutoff thickness[37]. We can see in figure 5.7 that slightly changing the core thickness forces the first and second modes to be guided or unguided at a certain width. So, to keep wide waveguides single-mode, we must reduce y_f , the core thickness, unfortunately also reducing the efficiency. We also see that the aspect ratio does not change substantially and the efficiency increases with the

thickness, because of better confinement. As a result of this analysis, we settled for 1.1 μm core thickness.

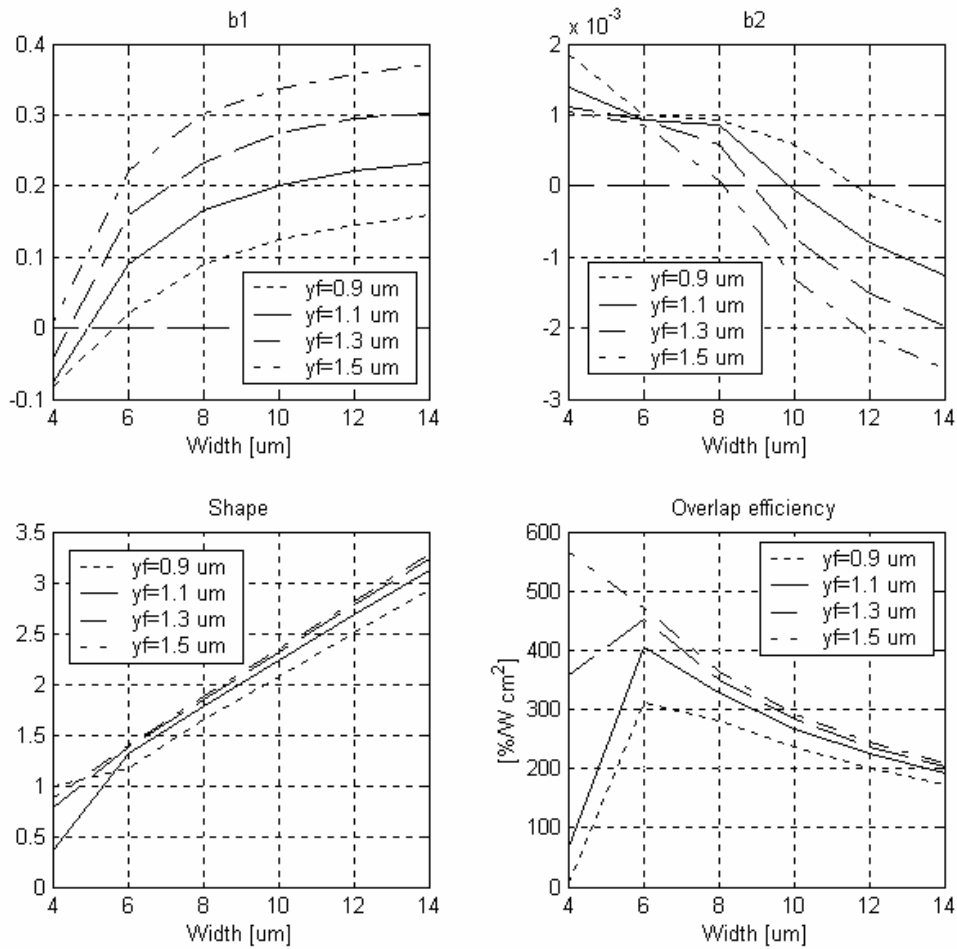


Figure 5.7: Parameter analysis as function of width for an almost symmetrical waveguide, for different values of the core thickness.

The cladding layers do not have an optimal thickness, rather, the thicker they are, the better. For one, it will make the modes more symmetrical and with this we will get better coupling into the guide. The upper cladding thickness will only be limited by how much we can etch, so we settled on a 2 μm thickness. Secondly, the lower cladding layer thickness controls how much of the mode leaks into the substrate, which is comprised of higher index GaAs. Figure 5.8 shows the loss due to substrate leakage as a function of

bottom cladding thickness, calculated using an approximation of a simple planar waveguide. For all the simulations above, we used a 10 microns thick bottom cladding and no GaAs layer to remove any complications in the numerical modeling, since our code could not have handled complex propagation constants.

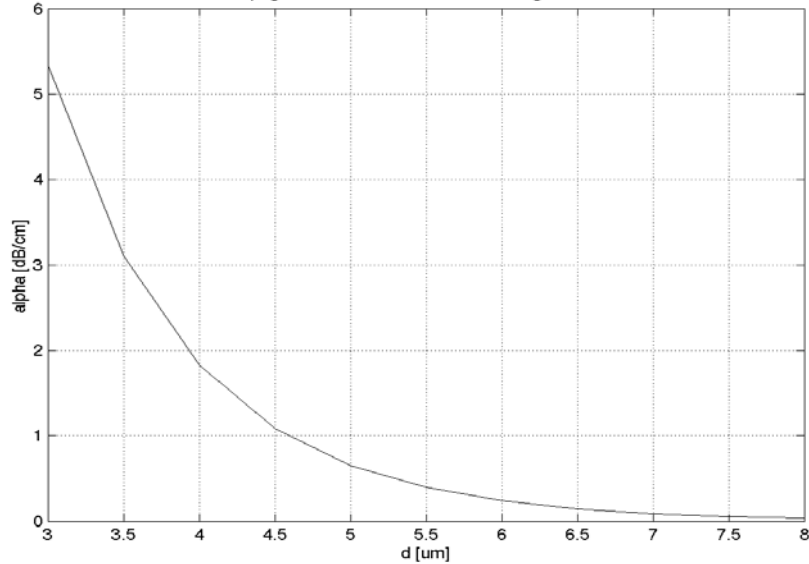


Figure 5.8: Loss due to leakage in the substrate as a function of bottom cladding thickness.

The next step we had to go over was to take care of fabrication tolerances. Errors in the fabrication process can manifest themselves in changes in the effective indices, and in particular in $\Delta n_{\text{eff}} = n_{2\omega} - n_{\omega}$, which sets the phasematching condition. Thus, trying to find conditions in which Δn_{eff} changes as little as possible with changing fabrication parameters is our goal.

Usually, composition and layer thicknesses are not too big of a problem, as long as the MBE system is well calibrated. We will focus here on fabrication errors, in particular lithography issues regarding waveguide width and etch depth control. Let us begin with etch depth control. If we could find an etch depth where the derivative of Δn_{eff} with respect to depth is close to 0, then we would have a good choice. Figure 5.9 shows calculation of Δn_{eff} vs. width of the waveguide for multiple different etch depths. The structure used for this analysis was a 1 μm upper cladding, 1 μm core and 5 μm bottom cladding. The figure clearly shows that as we get to about 2 μm depth, the etch depth

becomes not so critically important. In fact, this means that as long as we etch all the way through the core, the etch depth is not critical. In conclusion, as long as the etch depth is completely independent of the waveguide width (not always guaranteed depending on the etch method), then the etch depth can be made noncritical.

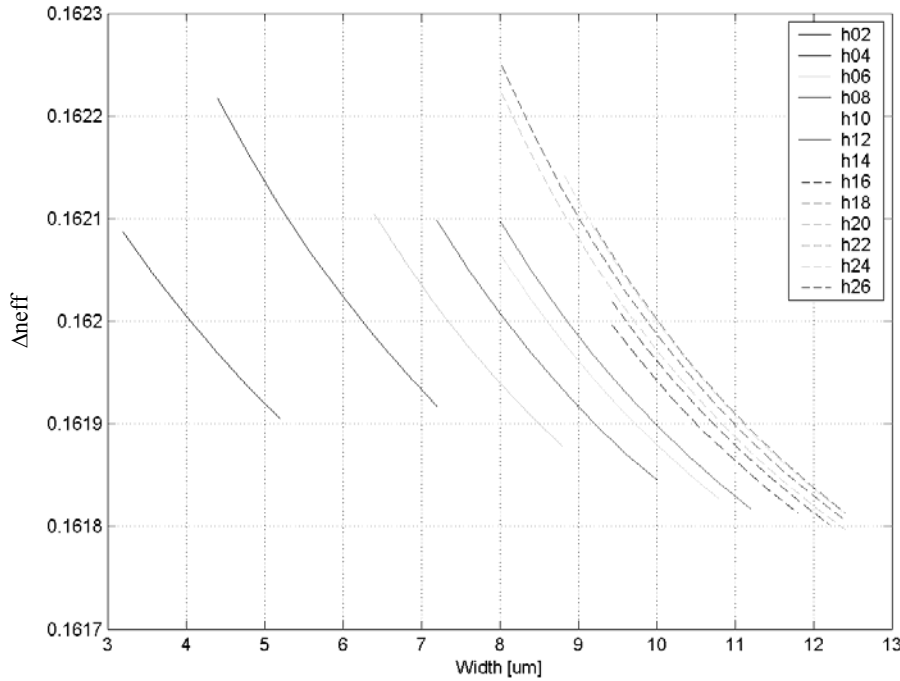


Figure 5.9: Δn_{eff} as a function of waveguide width for varying ridge height. As the core gets completely etched (2 μm deep in this case), the etch depth becomes noncritical. The values next to the h in the legend represent the etch depth in hundreds of nanometers.

The waveguide width can vary along the length of the waveguide as a result of imperfect lithography, photoresist treatment and etching. Unfortunately, there is no optimal value of the width where the derivative of Δn_{eff} with respect to the width is 0, as shown in figure 5.10. In fact, Δn_{eff} decreases monotonically towards 0 with increasing width, which just means that we want to use the widest guides possible. It intuitively makes sense, since a variation in the waveguide width is relatively smaller as the nominal width increases. Since we also want the guides to remain single mode at 1550 nm, the choice of 8 μm as the nominal width of our design is reinforced.

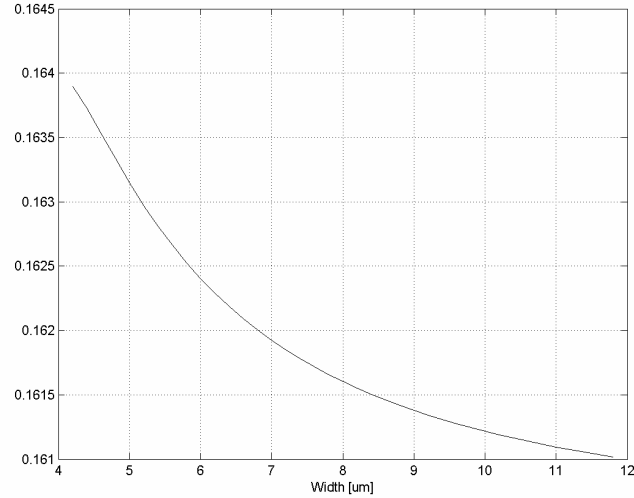


Figure 5.10: Δn_{eff} as a function of waveguide width for the same structure as in figure 5.9, with a 2 μm etch depth. Δn_{eff} does not have an optimum as a function of etch depth, so we just have to use the widest possible guides.

To conclude this section on the design of the waveguides, we also have to mention that by using a widely tunable laser, such as the external cavity diode laser, similar to the one mentioned in section 4.5, we can compensate for all the problems mentioned above. After our optimization, not having a very good fabrication process will not result in our missing the phasematching condition; rather it will lead to a broadening of the tuning curve and a reduction in overall conversion efficiency.

The final design that we adopted is shown in figure 5.11. It consists of a bottom cladding of 5.5 μm of $\text{Al}_{0.70}\text{Ga}_{0.30}\text{As}$, a core made of 1.1 μm of $\text{Al}_{0.67}\text{Ga}_{0.33}\text{As}$, and a top cladding made of 2 μm of $\text{Al}_{0.70}\text{Ga}_{0.30}\text{As}$. The nominal width of the ridge is 8 μm . To insure that we have etched all the way through the core, the targeted etch depth is 3.5 μm . This leads to a fairly symmetrical mode (the TE fundamental mode at 1550 nm is also shown in figure 5.11), and we calculated that we could achieve over 80% of power launching into the fundamental mode at 1550nm.

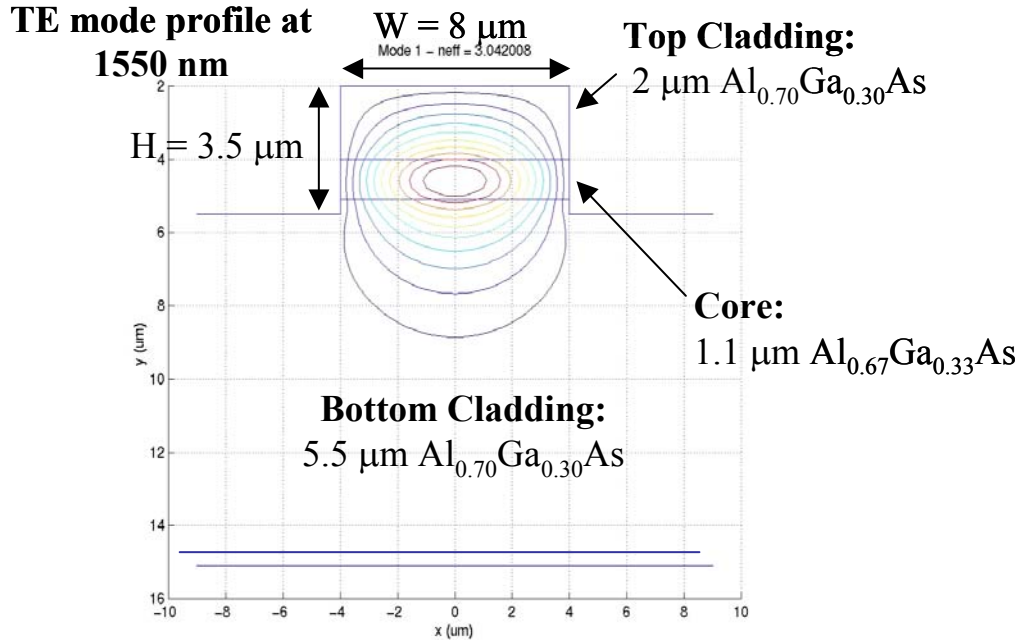


Figure 5.11: Final waveguide structure, with the profile of the fundamental TE mode at 1550 nm.

5.2.5 Waveguide fabrication

The waveguide structure described above was then grown on one of our orientation templates. In addition to the nominal QPM period of $4.8 \mu\text{m}$, we also included periods of 4.7 and $4.9 \mu\text{m}$, for additional insurance that we would find the phasematching peak. Then we patterned the ridges on the regrown wafer, and for testing they included widths of 6 , 8 , 10 , 12 , and $14 \mu\text{m}$.

The lithography, photoresist treatment and etching steps were the most crucial in reducing the propagation loss in the waveguides. We had to resort to a loop that consisted of growing a waveguide structure, pattern ridges, treat photoresist in different ways, then etch it with different techniques, and finally measure propagation losses. We had to iterate many times before we had a satisfying process.

One of the particularly difficult points was the choice between wet or dry etching techniques. The smoothness of the sidewalls of the ridges is critical to the propagation loss. Wet etching techniques such as a diffusion-limited etch provide the advantage of having a built-in smoothing mechanism. Unfortunately, they are hard to control, in particular because of undercut, which leads to uncertainty in the ridge width as we etch

more and more. On the other hand, dry etching in general results in vertical sidewalls, but they can be rough because they replicate the photoresist roughness itself. In the end, we decided to use a combination of photoresist treatment (baking at high temperature to induce reflowing to smooth it, then expose to UV light to harden the thin edges to resist the etching step), dry etching to etch vertical ridges, followed by a quick dip in a diffusion-limited etch solution to provide a final smoothing touch. With this process, we got very nice sidewalls with very little roughness, as shown in figure 5.12.

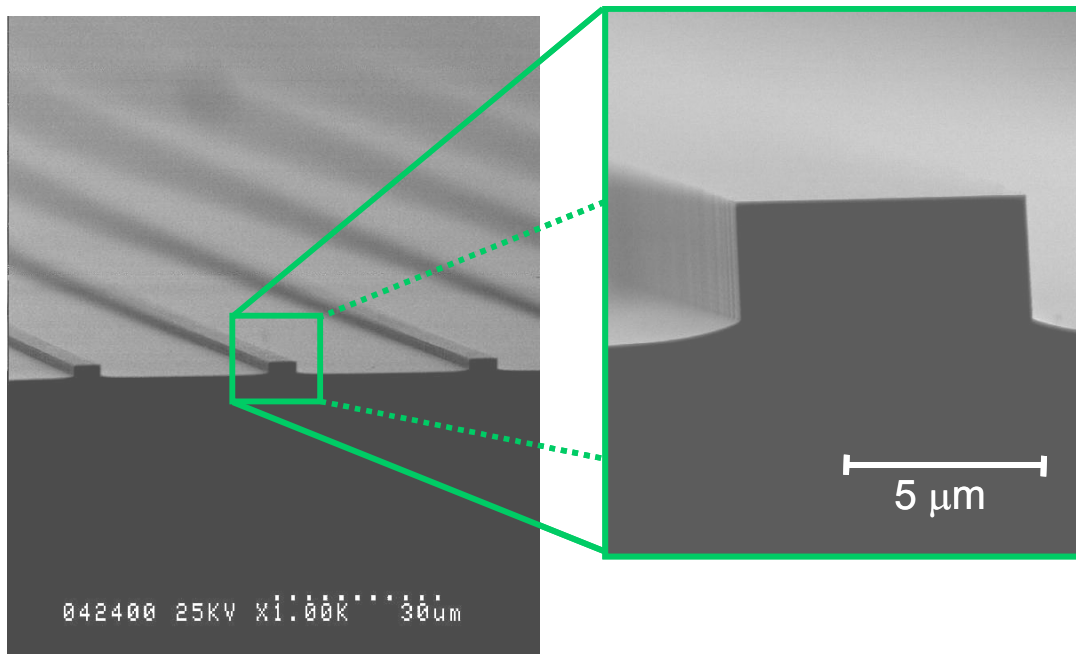


Figure 5.12: SEM of ridges etched with the Plasmaquest ECR-RIE dry etching system, followed by a dip in a diffusion-limited etching solution. The close-up shows an 8 μm wide ridge, with very smooth sidewalls.

To evaluate how well our process performed, we grew waveguides on unpatterned wafers, and then we compared their propagation losses at 1550 nm for the various combinations. To do so, we used a technique called the Fabry-Perot technique, which is very useful because it is insensitive to coupling efficiency into the waveguide. When we want to test a waveguide, we cleave two end facets and launch light into it. The facets act as mirrors, creating a Fabry-Perot cavity. The transmission of the light then has some peaks and valleys, as shown in figure 5.13.

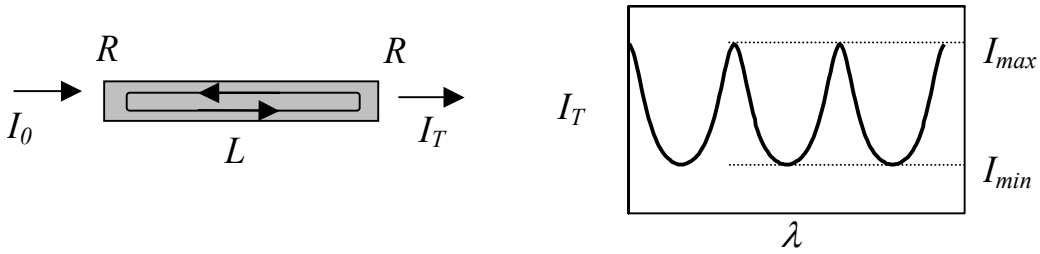


Figure 5.13: The end facets of a waveguide act as mirrors, thus creating a Fabry-Perot cavity. The transmission then shows peaks and valleys.

From the contrast between the peaks and valleys, knowing approximately the reflectivity of the facets and the length of the guide, it is possible to back out the value of the attenuation coefficient:

$$\alpha \approx \frac{4.34}{L} (\ln R + \ln 2 - \ln K) \tag{5.4}$$

$$K = \frac{I_{\max} - I_{\min}}{I_{\max} + I_{\min}}$$

This is valid only for relatively low loss waveguides, and long enough waveguides, so that the sensitivity is not too bad. Using this method, we measured an extensive set of waveguides, and found that for wide array of processing parameters, we could reduce the losses in the guides to as low as 3 dB/cm (figure 5.14).

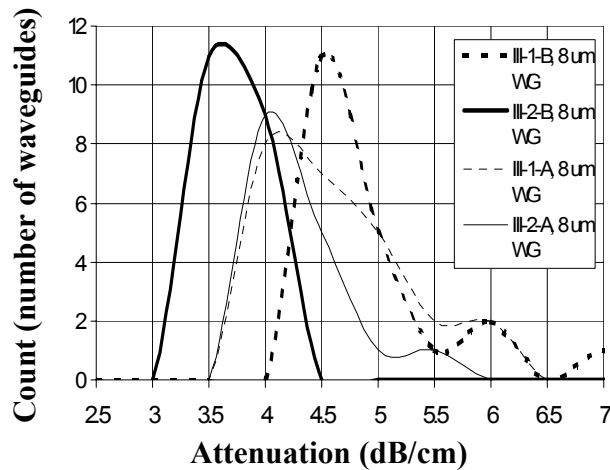


Figure 5.14: Measurement of losses for samples processed with varying parameters, showing that we have been able to fabricate unpatterned waveguides with loss as low as 3-4 dB/cm.

An additional remark is that these measurements were made on samples with a bottom cladding thickness of only 3.5 μm , which we made before completing our analysis of the design. For this cladding thickness, a loss of 2 dB/cm is predicted. Consequently, with a thicker bottom cladding we should get losses as low as 1 dB/cm in unpatterned waveguides.

5.3 Waveguide testing using SHG

Once we were satisfied with the design and fabrication process, we grew some waveguides on our orientation templates with the aforementioned periods. In this section we characterize these devices first with linear optical measurements, and then using second harmonic generation as a tool to demonstrate the robustness of our design.

5.3.1 Loss measurements in patterned waveguides

We first decided to measure propagation losses at 1550 nm before trying to perform second harmonic generation. Unfortunately, for these devices, we did not need (and in fact could not) use the Fabry-Perot technique, because the loss was too large. Thus we had to use very short samples (a few mm long) just to see light coming out of the guides.

We ended up measuring approximate losses of up to 50 dB/cm on various waveguides. What went wrong for these devices? For one, in waveguides regrown on the unpatterned regions of the template, we measured losses of 8 to 10 dB/cm at 1550 nm, already much larger than those grown on standard (100) wafers without the whole regrowth preparation. The next important factor to consider is that we started the regrowth on a corrugated substrate, as discussed in chapter 3. The starting corrugation was about 1300 \AA . If this is somewhat conserved as the film grows, then the core/cladding interfaces also have a fairly large corrugation. This means that there is a built-in diffraction grating in the waveguide, which can create large attenuation, of course.

In fact, we decided to try and see how much loss such a corrugation can introduce. To model this, we used a simple planar waveguide model taken from Marcuse.

Coupled-mode theory is used to derive the attenuation associated with the coupling between a guided mode and a radiation mode created by the periodic deformation of the core/cladding interfaces. Even if this is not an exact model, in the sense that it will not predict exactly for what period the attenuation is the highest, it can still give a qualitative idea of the kind of attenuation numbers we can be expecting because of this effect. To make it more relevant, we modeled a 1D planar waveguide which gave the same effective index for the fundamental mode as our simulations did for our 2D waveguide. Figure 5.15 shows the results for a corrugation of 1500 Å.

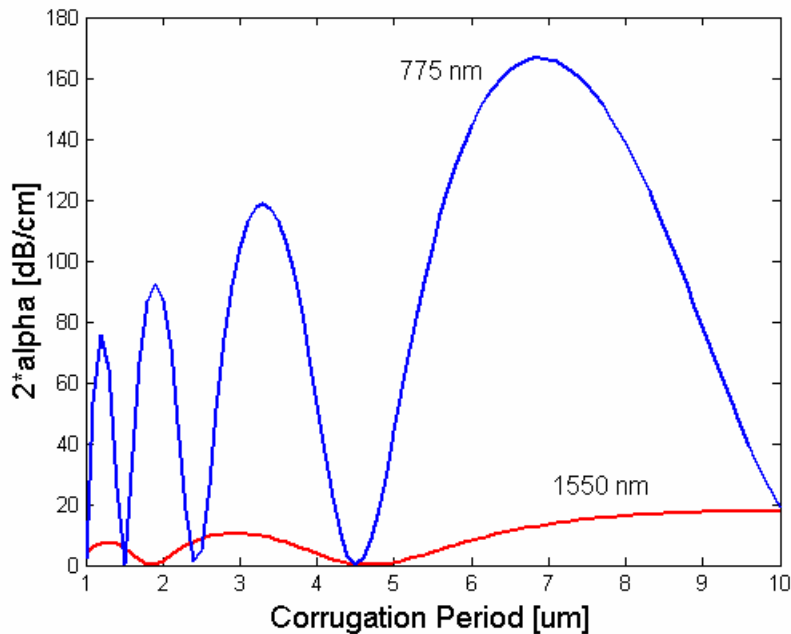


Figure 5.15: Attenuation from corrugated core/cladding interface calculated using coupled-mode theory for a planar waveguide with 1500 Å corrugation at both fundamental and second harmonic wavelengths.

The order of magnitude of the attenuation given by this model is consistent with what we observed in our waveguides. One important note is that the attenuation at a given period scales with the square of the corrugation. If we could reduce the corrugation to the 200 to 300 Å level, as we have already been able to do on occasion, then the attenuation would drop to less than 10 dB/cm, which would certainly be much more manageable. Also, another point to make is that there might exist regions of parameter space where the period of the QPM grating corresponds to a minimum in the attenuation

for both 1550 and 780 nm, as for instance around a period of $4.5 \mu\text{m}$ in figure 5.15. This suggests that careful design of the waveguide might be able to completely get rid of this problem, even when the corrugation is not zero. Of course, this might require too many compromises and a zero-corrugation template is preferable.

5.3.2 Second harmonic generation setup

Even though the guides had huge losses, we decided to try and verify the quality and robustness of our design by performing second harmonic generation. If we can see a phasematching peak at the position we expect, then that means that we have done a good job at designing these waveguides.

Figure 5.16 shows the experimental setup for this experiment. The source is an external cavity tunable laser (the same as that used in chapter 4), fiber coupled into an erbium-doped fiber amplifier. The polarization of the output of the amplifier is controlled by a wave-plate and a polarizer. Using these components, the power incident on the sample was about 20 mW, focused on the sample through an input objective serving as an input coupler.

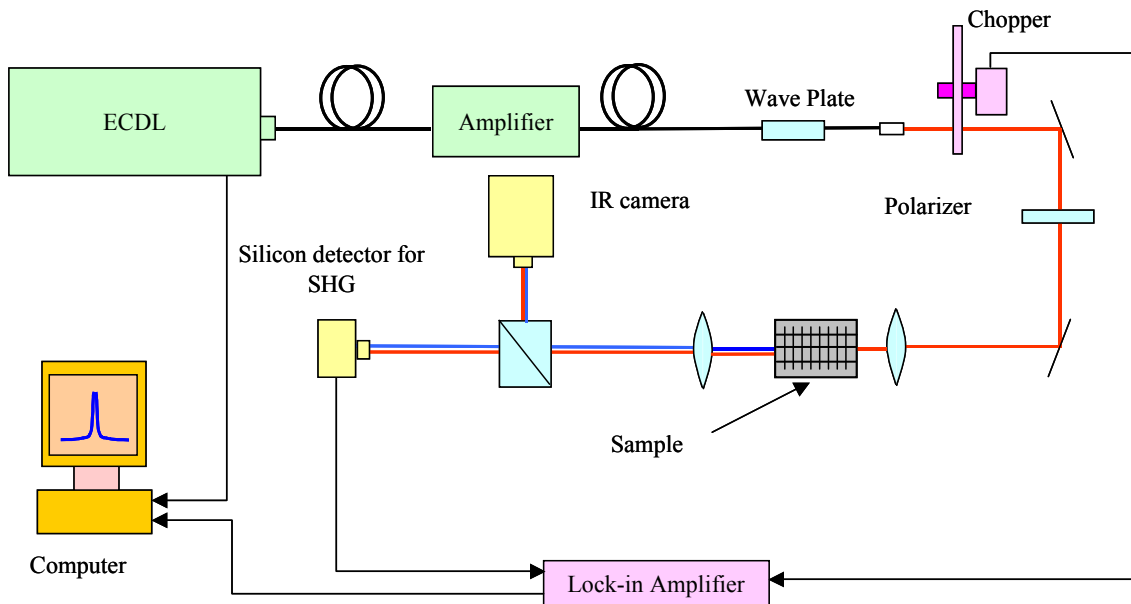


Figure 5.16: Waveguide SHG setup

The light coming out of the sample was collected by another objective and imaged onto either a silicon detector for measurement of the SHG power, or an IR camera to monitor the behavior of the guides at 1550 nm. The sample and both input and output objectives were mounted on their respective three-axes stages to facilitate optimum launching into the waveguides.

Rough estimates taking into account experimental conditions and the measured attenuations put the SHG power on the order of a few nW, necessitating the use of the lock-in amplifier. The silicon detector, plugged in directly into the lock-in, would produce a few 100s of pA with this kind of signal power, compared to a background noise of less than 10 pA. Once we were satisfied that we could actually measure the expected signal, we proceeded with the experiment.

5.3.3 SHG measurements

Even with such lossy waveguides, we were able to observe second harmonic generation. We used 4 mm long waveguides, but could test only the 8 μm wide guides, because the 6 μm guides were too lossy for us to manage to launch light in them. Figure 5.17 shows two tuning curves taken in these samples with respective QPM period of 4.7 and 4.8 μm . The waveguides with 4.9 μm period turned out to have a phasematching peak outside of the range of our tunable source.

The original predictions from our mode solver gave the phasematching peak at 1552.5 nm for the 4.8 μm period grating. Our measurement put the phasematching peak at 1563.9 nm. The shift of the phasematching peak between 4.8 and 4.7 μm period matches very well, though (9.9 nm experimental versus 9.5 nm theoretically). Explaining such a large shift in phasematching is difficult with just fabrication issues such as the 8 μm nominal width actually being slight smaller. We were able to match the position and width of the tuning curves very well, however (figure 5.17), by changing the composition of the layers to $\text{Al}_{0.67}\text{Ga}_{0.33}\text{As}/\text{Al}_{0.64}\text{Ga}_{0.36}\text{As}$ for the cladding/core and a ridge width of 7 μm . While it is unexpected, it is possible that the MBE system was not well calibrated and led to this discrepancy.

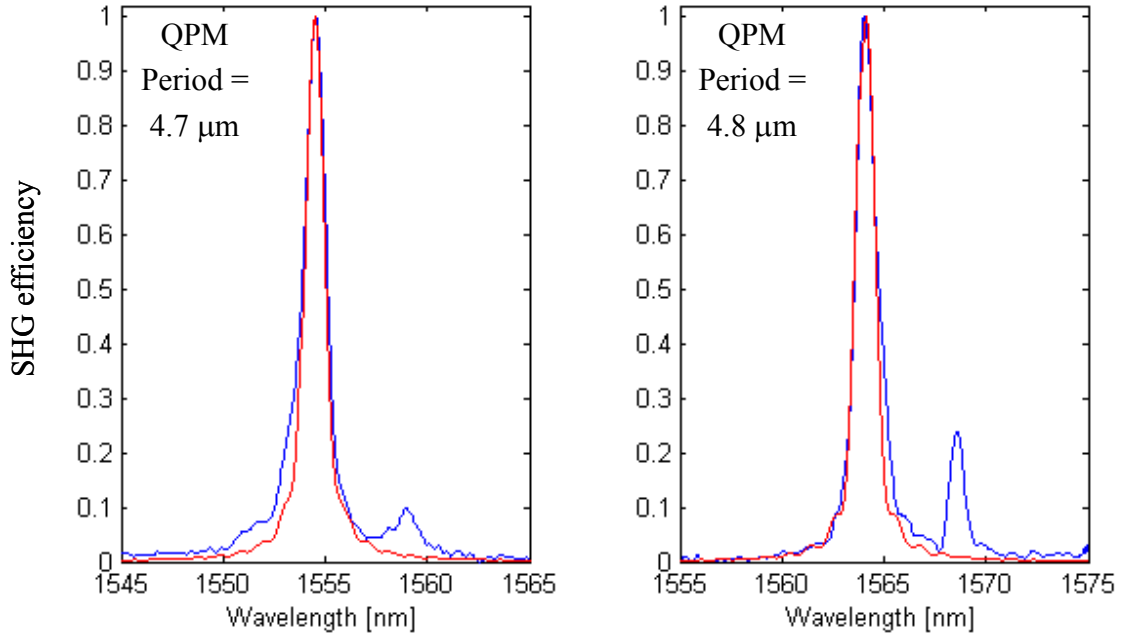


Figure 5.17: Tuning curves for 4 mm long, 8 μm wide waveguides, with QPM periods of 4.7 and 4.8 μm , overlaid with theoretical calculations.

We were able to match the width of the tuning curves by using 50 dB/cm as the fundamental propagation loss, then using the second harmonic attenuation as a fitting parameter. Using this method, we obtained the second harmonic attenuation coefficient to be 55 dB/cm, which is a reasonable value considering figure 5.15.

We also measured SHG tuning curves in three waveguides located side by side with the same width on the same samples, for the two different periods, to compare their phasematching peak and width and verify the homogeneity of the sample. The fact that the curves all look very similar confirms this. These tuning curves are shown in figure 5.18.

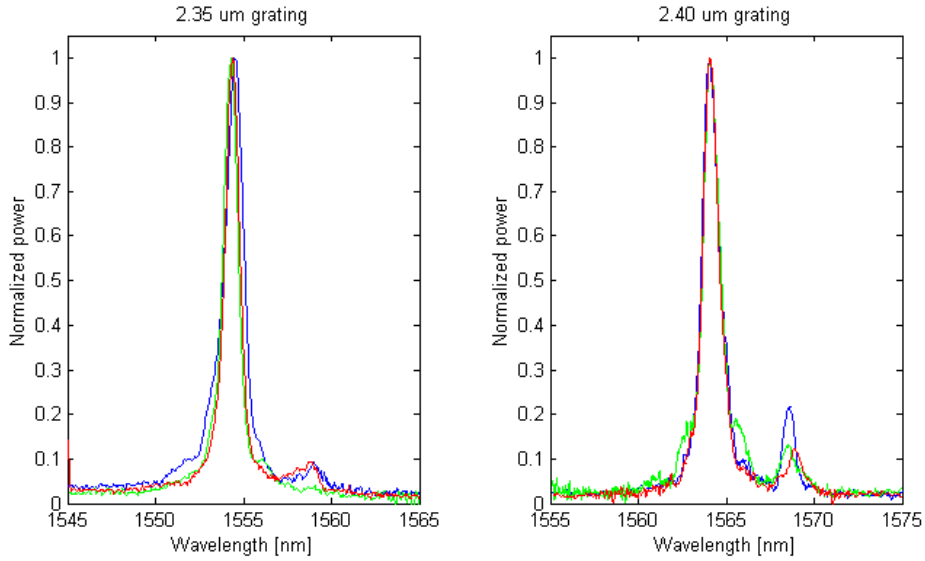


Figure 5.18: Tuning curves of three waveguides located side by side for two different QPM periods, to verify the local homogeneity of the samples.

The maximum output power we measured was approximately 2 nW. Using the expressions calculated in chapter 2 (equations 2.36, 2.37 and 2.38) and knowing how loss changes the conversion efficiency (equation 2.30), we can make an estimate of the theoretically expected power by calculating the overlap from the results of the mode solver. Such a calculation gives a value of approximately 20 nW, assuming a launching efficiency of 86%. Being within an order of magnitude of the expected value is very good, considering all the uncertainties in the experiment (exact attenuation values, launching efficiency, for instance).

We should also note that the tuning curves show a secondary peak at a slightly longer wavelength than the primary phasematching peak, shifted by about 4.5 nm. There are multiple possible reasons for the existence of this peak.

Due to the symmetry of the non-linear tensor of AlGaAs, fundamental TE modes may generate only SHG TM modes. However, a mix of TE and TM modes at the fundamental wavelength, due to a non-perfect polarizer, could generate a second harmonic TE mode, phasematched at the shifted wavelength. This hypothesis revealed to be wrong because the peak wavelength shift for such modes would not be so large. Moreover, careful experiments with the polarizer, involving only TE modes at the fundamental wavelength, excluded the presence of SHG TE modes.

Another hypothesis could be the phasematching of the fundamental mode with a higher order SHG odd mode (even modes would cancel out the overlap integral). Unfortunately this explanation must be wrong as well, simply because the wavelength shift would be in the opposite direction.

Another possible explanation could be phasematching between a fundamental “leaky mode” and the first SHG mode. Non-guided modes effective indexes, issued by simulations, indicate that they could phasematch a SHG mode at the shifted wavelength. Moreover, the simulated leaky mode shape has a lobe exactly in the waveguide core, so it could efficiently overlap the first SHG mode. This leaky mode would quickly vanish, but it may generate enough SHG power in the short guides we tested to be detected.

The reason for this second peak remains to be investigated, but we suspect that the last explanation is probably correct and that if we were able to build low-loss waveguides, we would not see this peak appear in longer devices.

5.4 Conclusion

While the waveguides we fabricated ended up not performing better than earlier tries, we believe that we have come up with a better design, more robust and reliable. We were able to demonstrate second harmonic generation and explain most of the experimental observations we made. Clearly, taking into account the corrugations in the design from the start could result in lower loss devices, but the best way to go about this is to work at the template level and try to reduce or completely get rid of the corrugation. When we can do this, then the orientation-patterned AlGaAs waveguides can be studied more extensively and their performance compared to that of PPLN waveguides.

CHAPTER 6: CONCLUSION

When work on this project started, we established that existing materials for nonlinear frequency conversion in the mid-IR were limited by many issues. For this reason, we started investigating semiconductors, and GaAs in particular, because of their excellent properties and mature growth and fabrication technologies, which made them ideal candidates for these applications.

Unfortunately, because of their optical isotropy, it had been very hard to make them useful for nonlinear frequency conversion because of the lack of a phasematching technique. However, the potential of these materials for high performance in the applications of interest led to the invention of the all-epitaxial orientation-patterning technique for GaAs, which appears to be so far the best way to tackle this issue.

The work presented here continues the efforts of previous graduate students[46,47] in the development of this technique. To summarize it, I will first present the accomplishments described here. Then I will discuss what the possible avenues for future work are, hoping that this work has brought all-epitaxial orientation patterning a little closer to fulfilling the promise that led to its invention.

6.1 Accomplishments

The accomplishments of this work can be divided in two categories. We will start by covering the materials research side of this project by summarizing the results of the epitaxial growth of orientation-patterned GaAs by both MBE and HVPE. In the second part we will go over the optical results, in particular the nonlinear frequency conversion experiments.

6.1.1 Materials research

The most important part of this project has always been the materials side of it. From the early work on lattice inversion with MBE[46] to the results presented here on the 0.5 mm thick films of HVPE-grown GaAs, this part of the work was the driving force. There of

course remains quite a lot to do, but we can already look back at the accomplishments and marvel at the fact that even though we did not have that many growth runs of either MBE or HVPE, the results are already quite impressive.

The MBE growth of the orientation template is well developed and very reliably produces the templates discussed in chapter 3. Occasionally, we can even get templates with much lower corrugations, which clearly means that it is possible to achieve and that it is only a question of time before this goal is reached as well. The domains achieved on the MBE templates are already short enough to phasematch any interaction in the transparency range of AlGaAs. The waveguides grown with MBE also showed some promise and their shortcomings are completely due to the quality of the templates.

The major success of this work was to show that 0.5 mm thick films of GaAs could be grown on the orientation templates and that the quality of the QPM gratings in these films is almost entirely determined by the quality of the original substrate. In fact, these results suggest that given the right HVPE conditions, the antiphase domains propagate straight up through the film and that thicker films are not out of the question provided higher quality templates can be fabricated. In this work, we fabricated these thick films with sufficient quality to be used in nonlinear frequency conversion down to 26.3 μm periods, over lengths of 1 to 2 cm.

6.1.2 Nonlinear frequency conversion

The success we enjoyed with the materials development made possible the results in frequency conversion presented in this dissertation, in particular in the thick films. These films had very low losses, which allowed us to demonstrate second harmonic generation and measure the nonlinear coefficient of GaAs with good accuracy. The SHG experiments also showed the high quality achievable with our technique.

This was confirmed by the first experimental demonstration of generation of mid-IR by difference-frequency mixing of two near-IR beams in all-epitaxially grown OP-GaAs films. Since this was one of the original goals of the project, this is a very satisfying accomplishment, especially knowing that it already is being used in a spectroscopy experiment. More experiments are under way to try and show other

nonlinear interactions, and hopefully demonstrate parametric amplification and oscillation.

In the waveguide devices, we were able to design a very robust device that performed as expected, being very tolerant of fabrication errors. The performance of the device was not very good due to the high propagation losses. Once again, though, this will be solved when a better template emerges.

6.2 Future work

As work continues on this project, new efforts will have to focus on several different areas. The most important improvements should be made on the template fabrication. We have seen that the large corrugations needed to ensure that we have single domain inverted GaAs are the main reason for multiple problems, ranging from the bad quality of the short period gratings in the thick films, to the high losses in the waveguide devices. A review of early results in the study of MBE growth for lattice inversion has suggested that template quality would improve if wafers misoriented towards (111)A were used instead of the current opposite misorientation[47]. Some occurrence of low corrugation templates have also been observed on (111)B misoriented substrates and this deserves to be investigated as well. The MBE regrowth also appears to be less than ideal at this point, as exemplified by the quality of the templates for short periods and the loss of waveguides regrown on unpatterned areas of the templates. This needs to be improved.

On the thick film side, there does not seem to be any fundamental limitations and thicker films will probably be grown soon. This work was done mostly because of the goodwill of the French group, and while we appreciated their help, such a project requires a more reliable thick film growth partner. This will in fact come true as a group is building and testing an HVPE reactor at Hanscom Air Force Base to participate in this project. With the steady supply of material coming from them, this project will undoubtedly be able to progress faster and in more directions than before. For instance, growth defects will probably disappear and many more types of devices will be tested, simply because of the availability of the material. It will also allow for a more systematic study of the properties of the HVPE material, such as loss and dispersion, which are

necessary for device design. In fact, some efforts are currently under way to get a better dispersion model and temperature dependence of the refractive index for GaAs so that the QPM periods can be calculated more accurately.

For waveguide devices, everything comes down to the improvements in the templates. The current fabrication process has proven to be able to produce low-loss waveguides on unpatterned substrates. Once the QPM devices are low-loss as well, then many experiments will be done, going from simple channel shifting through DFG, to others like dispersion compensation. One problem that remains to be solved is how to efficiently couple the pump beam at around 780 nm into the fundamental mode of the waveguide. Mode filters, adiabatic tapers and couplers have been developed in PPLN devices, but remain much harder to make for AlGaAs. Some effort will have to be expended to make these devices useful.

Finally, in the long term, this technique could be adapted to other materials. First, by maybe using the GaAs orientation template to grow orientation-patterned ZnSe on top of it. A second possibility is using a similar approach with the GaP/Si system, since GaP and Si are also closely lattice-matched. The dispersion properties of GaP make it a very interesting material for nonlinear optics.

6.3 Conclusion

All-epitaxial orientation-patterning of GaAs is a very promising technology for fabricating high-performance frequency conversion devices for a variety of applications in the infrared. While there still remain some obstacles to achieving the performance predicted from the material properties of GaAs, such as improving the orientation templates and succeeding in growing thicker films, it is already close to being usable and certainly will become superior in many ways to other approaches. Hopefully, this technique will be extended to other semiconductors to create a family of engineerable materials for nonlinear frequency conversion.

BIBLIOGRAPHY

1. Y. R. Shen, *The Principles of Nonlinear Optics*, (J. Wiley, New York, 1984).
2. G. E. Keiser, "A review of WDM technology and applications," *Opt. Fib. Technol. : Mat. Devi. Sys.* **5**, p.3 (1999).
3. R. J. McNichols and G. L. Cote, "Optical glucose sensing in biological fluids: an overview," *J. Biomed. Opt.* **5**, p.5 (2000).
4. L. A. Coldren and S. W. Corzine, *Diode lasers and photonic integrated circuits*, (Wiley, New York, 1995).
5. M. C. Larson, C. W. Coldren, S. G. Spruytte, H. E. Petersen, and J. S. Harris, Jr., "Room temperature continuous-wave operation of GaInNAs long wavelength VCSELs," *58th DRC. Device Research Conference* p.117 (2000).
6. S. M. Sze, *Physics of semiconductor devices*, (Wiley, New York, 1981).
7. M. Tacke, "Lead-salt lasers," *Philosophical Transactions of the Royal Society London, Series A* **359**, p.547 (2001).
8. J. Faist, F. Capasso, D. L. Sivco, C. Sirtori, A. L. Hutchinson, and A. Y. Cho, "Quantum cascade laser," *Science* **264**, p.553 (1994).
9. D. Hofstetter, M. Beck, T. Aellen, and J. Faist, "High-temperature operation of distributed feedback quantum-cascade lasers at 5.3 μ m," *Appl. Phys. Lett.* **78**, p.396 (2001).
10. Proceedings of the Conference on Lasers and Electro-Optics, p.324-326 (2001).

11. F. K. Tittel, D. G. Lancaster, and D. Richter, "Compact high power mid-IR spectroscopic source based on difference frequency generation in PPLN," *Topical Meeting on Advanced Solid-State Lasers (ASSL 2000)* p.271 (2000).
12. C. Da-Wun and K. Masters, "Continuous-wave 4.3- μ m intracavity difference frequency generation in an optical parametric oscillator," *Opt. Lett.* **26**, p.25 (2001).
13. F. Rotermund, V. Petrov, and F. Noack, "Difference-frequency generation of intense femtosecond pulses in the mid-IR (4-12 μ m) using HgGa_2S_4 and AgGaS_2 ," *Opt. Comm.* **185**, p.177 (2000).
14. M. H. Chou, J. Hauden, M. A. Arbore, and M. M. Fejer, "1.5- μ m-band wavelength conversion based on difference-frequency generation in LiNbO_3 waveguides," *Opt. Lett.* **23**, p.1004 (1998).
15. M. H. Chou, I. Brener, M. M. Fejer, E. E. Chaban, and S. B. Christman, "1.5- μ m-band wavelength conversion based on cascaded second-order nonlinear susceptibility in LiNbO_3 ," *IEEE Photon. Technol. Lett.* **11**, (1999).
16. M. H. Chou, I. Brener, G. Lenz, R. Scotti, E. E. Chaban, J. Shmulovich, D. Philen, S. Kosinski, K. R. Parameswaran, and M. M. Fejer, "Efficient wide-band and tunable midspan spectral inverted using cascaded nonlinearities in LiNbO_3 waveguides," *IEEE Photon. Technol. Lett.* **12**, p.82 (2000).
17. I. Brener, M. H. Chou, E. E. Chaban, K. R. Parameswaran, M. M. Fejer, S. Kosinski, and D. L. Pruitt, "Polarization-insensitive wavelength converter based on cascaded nonlinearities in LiNbO_3 waveguides," *Electron. Lett.* **36**, p.66 (2000).
18. G. D. Miller, R. G. Batchko, W. M. Tulloch, D. R. Weise, M. M. Fejer, and R. L. Byer, "42%-efficient single-pass CW second-harmonic generation in periodically-poled lithium niobate," *Opt. Lett.* **22**, p.1834 (1997).

19. D. Mazzotti, P. De Natale, G. Giusfredi, C. Fort, J. A. Mitchell, and L. W. Hollberg, "Difference-frequency generation in PPLN at 4.25 μm : an analysis of sensitivity limits for DFG spectrometers," *Appl. Phys. B, Lasers Opt.* **B70**, p.747 (2000).
20. K. L. Vodopyanov, F. Ganikhanov, J. P. Maffetone, I. Zwieback, and W. Ruderman, "ZGP OPO with a 3.8-12.4 μm tunability," *TOPS* **39**, p.7 (2000).
21. F. Ganikhanov, T. Caughey, and K. L. Vodopyanov, "Narrow-linewidth middle-infrared ZnGeP₂ optical parametric oscillator," *J. Opt. Soc. Am. B* **18**, p.818 (2001).
22. P. A. Budni, L. A. Pomeranz, M. L. Lemons, C. A. Miller, J. R. Mosto, and E. P. Chicklis, "Efficient mid-infrared laser using 1.9- μm -pumped Ho:YAG and ZnGeP₂ optical parametric oscillators," *J. Opt. Soc. Am. B* **17**, p.723 (2000).
23. Leo, G., Berger, V., De Rossi, A., Calligaro, M., Marcadet, X., Fiore, A., and Nagle, J. Parametric processes in GaAs/Al₂O₃ structures. 3928, p.94-107. 2000. Proceedings of the SPIE; Nonlinear Materials, Devices, and Applications, 24-25 Jan. 2000, San Jose, CA, USA.
24. A. Fiore, S. Janz, L. Delobel, P. Van der Meer, P. Bravetti, V. Berger, E. Rosencher, and J. Nagle, "Second harmonic generation at $\lambda=1.6\ \mu\text{m}$ in AlGaAs/Al₂O₃ waveguides using birefringent phase matching," *Appl. Phys. Lett.* **72**, p.2942 (1998).
25. A. Fiore, V. Berger, E. Rosencher, P. Bravetti, N. Laurent, and J. Nagle, "Phase-matched mid-infrared difference frequency generation in GaAs-based waveguides," *Appl. Phys. Lett.* **71**, p.3622 (1997).
26. L. A. Gordon, R. C. Eckardt, and R. L. Byer, "Investigations of diffusion-bonded stacked GaAs for infrared quasi-phasematched parametric oscillations," *SPIE Proceedings Series* **2145**, p.316 (1994).

27. L. Gordon, G. L. Woods, R. C. Eckardt, R. R. Route, R. S. Feigelson, M. M. Fejer, and R. L. Byer, "Diffusion-bonded stacked GaAs for quasi-phase-matched second-harmonic generation of a carbon dioxide laser," *Electron. Lett.* **29**, p.1942 (1993).
28. S. J. B. Yoo, R. Bhat, C. Caneau, and M. A. Koza, "Quasi-phase-matched second-harmonic generation in AlGaAs waveguides with periodic domain inversion achieved by wafer-bonding," *Appl. Phys. Lett.* **66**, p.3410 (1995).
29. M. J. Angell, R. M. Emerson, J. L. Hoyt, J. F. Gibbons, L. A. Eyres, M. L. Bortz, and M. M. Fejer, "Growth of alternating $\langle 100 \rangle / \langle 111 \rangle$ -oriented II-VI regions for quasi-phase-matched nonlinear optical devices on GaAs substrates," *Appl. Phys. Lett.* **64**, p.3107 (1993).
30. C. B. Ebert, L. A. Eyres, M. M. Fejer, and J. S. Jr. Harris, "MBE growth of antiphase GaAs films using GaAs/Ge/GaAs heteroepitaxy," *J. Cryst. Growth* **201**, p.187 (1999).
31. S. Koh, T. Kondo, T. Ishiwada, C. Iwamoto, H. Ichinose, H. Yaguchi, T. Usami, Y. Shiraki, and R. Ito, "Sublattice reversal in GaAs/Si/GaAs (100) heterostructures by molecular beam epitaxy," *Jpn. J. Appl. Phys.* **37**, p.L1493 (1998).
32. S. Koh, T. Kondo, M. Ebihara, T. Ishiwada, H. Sawada, H. Ichinose, I. Shoji, and R. Ito, "GaAs/Ge/GaAs sublattice reversal epitaxy on GaAs (100) and (111) substrates for nonlinear optical devices," *Jpn. J. Appl. Phys.* **38**, p.L508 (1999).
33. R. W. Boyd, *Nonlinear Optics*, (Academic Press, San Diego, 1992).
34. P. A. Franken, A. E. Hill, C. W. Peters, and G. Weinreich, "Generation of Optical Harmonics," *Phys. Rev. Lett.* **7**, p.118 (1961).
35. J. Q. Yao and T. S. Fahlen, "Calculations of optimum phase match parameters for the biaxial crystal KTiOPO₄," *J. Appl. Phys.* **55**, p.65 (1984).

36. J. A. Armstrong, N. Bloembergen, J. Ducuing, and P. S. Pershan, "Interactions between light waves in a nonlinear dielectric," *Phys. Rev.* **127**, p.1918 (1962).
37. D. Marcuse, *Theory of dielectric waveguides*, (Academic Press, San Diego, 1991).
38. G. L. Woods, "Nonlinear optical frequency conversion devices based on intersubband transitions in semiconductor quantum wells," Ph.D. (Stanford University, 1997).
39. G. D. Boyd and D. A. Kleinman, "Parametric interaction of focused gaussian light beams," *J. Appl. Phys.* **39**, p.3597 (1968).
40. S. Guha, F. J. Wu, and J. Falk, "The effects of focusing on parametric oscillation," *IEEE J. Quantum Electron.* **QE-18**, p.907 (1982).
41. J. Mayet, "Quasi-phase-matched frequency conversion of gaussian beams," B.S. (Stanford University, 1996).
42. N.-H. Cho, B. C. De Cooman, C. B. Carter, R. Fletcher, and D. K. Wagner, "Antiphase boundaries in GaAs," *Appl. Phys. Lett.* **47**, p.879 (1985).
43. H. Kroemer, "Polar-on-nonpolar epitaxy: progress and new problems," *Inst. Phys. Conf. Ser.* **91**, p.21 (1987).
44. R. Fisher, W. T. Masselink, J. Klem, T. Henderson, T. C. McGlinn, M. V. Klein, and H. Morkoc, "Growth and properties of GaAs/AlGaAs on nonpolar substrates using molecular beam epitaxy," *J. Appl. Phys.* **58**, p.374 (1985).
45. S. M. Ting, E. A. Fitzgerald, R. M. Sieg, and S. A. Ringel, "Range of Defect Morphologies on GaAs grown on offcut (001) Ge substrates," *J. Electron. Mater.* **27**, p.451 (1998).
46. C. B. Ebert, "Quasi-phasesmatched waveguides for infrared nonlinear optics using GaAs/Ge/GaAs heteroepitaxy," Ph.D. (Stanford University, 1998).

47. L. A. Eyres, "Epitaxially orientation-patterned AlGaAs for nonlinear optical frequency conversion," Ph.D. (Stanford University, 2001).
48. W. Braun, *Applied RHEED: reflection high-energy diffraction during crystal growth*, (Springer, New York, 1999).
49. M. A. Herman and H. Sitter, *Molecular beam epitaxy: fundamentals and current status*, (Springer, Berlin, 1996).
50. Y. Horikoshi, "Migration-enhanced epitaxy of GaAs and AlGaAs," *Semicond. Sci. Technol.* **8**, p.1032 (1993).
51. M. Kawashima, S. Tadashi, and Y. Horikoshi, "Characteristics of AlGaAs/GaAs heterostructures grown by migration-enhanced epitaxy at high temperatures," *Semicond. Sci. Technol.* **10**, p.1237 (1995).
52. C. Lin, "Surface micromachined tunable optoelectronic devices," Ph.D. (Stanford University, 2002).
53. G. B. Stringfellow, *Organometallic vapor-phase epitaxy: theory and practice*, (Academic Press, San Diego, 1999).
54. J. L. Gentner, "Vapour phase growth of GaAs by the chloride process under reduced pressure," *Philips J. Res.* **38**, p.37 (1983).
55. F. Chavez, J. Mimila-Arroyo, F. Bailly, and J. C. Bourgoin, "Epitaxial GaAs by close space vapor transport," *J. Appl. Phys.* **54**, p.6646 (1983).
56. L. Becouarn, B. Gerard, M. Brevignon, J. Lehoux, Y. Gourdel, and E. Lallier, "Second harmonic generation of CO₂ laser using thick quasi-phase-matched GaAs layer grown by hydride vapour phase epitaxy," *Electron. Lett.* **34**, p.2409 (1998).
57. D. W. Shaw, "Kinetic aspects in the vapour phase epitaxy of III-V compounds," *J. Cryst. Growth* **31**, p.130 (1975).

58. L. A. Eyres, P. J. Tourreau, T. J. Pinguet, C. B. Ebert, J. S. Harris, Jr., M. M. Fejer, L. Becouarn, B. Gerard, and E. Lallier, "All-epitaxial fabrication of thick, orientation-patterned GaAs films for nonlinear optical frequency conversion," *Appl. Phys. Lett.* **79**, p.904 (2001).
59. E. Gil-Lafon, J. Napierala, D. Castelluci, A. Pimpinelli, R. Cadoret, and B. Gerard, "Selective growth of GaAs by HVPE: keys for accurate control of the growth morphologies," *J. Cryst. Growth* **222**, p.482 (2001).
60. J. I. Pankove, *Optical processes in semiconductors*, (Prentice-Hall, Englewood Cliffs, NJ, 1971).
61. S. R. Johnson and T. Tiedje, "Temperature dependence of the Urbach edge in GaAs," *J. Appl. Phys.* **78**, p.5609 (1995).
62. A. N. Pikhtin and A. D. Yas'kov, "Dispersion of the refractive index of semiconductors with diamond and zinc-blend structures," *Sov. Phys. Semicond.* **12**, p.622 (1978).
63. M. M. Choy and R. L. Byer, "Accurate second-order susceptibility measurements of visible and infrared nonlinear crystals," *Phys. Rev. B* **14**, p.1693 (1976).
64. I. Shoji, T. Kondo, A. Kitamoto, M. Shirane, and R. Ito, "Absolute scale of second-order nonlinear-optical coefficients," *J. Opt. Soc. Am. B* **14**, p.2268 (1997).
65. D. H. Jundt, "Temperature-dependent Sellmeier equation for the index of refraction, n_{e} , in congruent lithium niobate," *Opt. Lett.* **22**, p.1553 (1997).
66. D. A. Roberts, "Simplified characterization of uniaxial and biaxial nonlinear optical crystals: a plea for standardization of nomenclature and conventions," *IEEE J. Quantum Electron.* **28**, p.2057 (1992).

67. S. Kawanishi, M. H. Chou, K. Fujiura, M. M. Fejer, and T. Morioka, "All-optical modulation and time-division-multiplexing of 100 Gbit/s signal using quasi-phase matched mixing in LiNbO_3 waveguides," *Electron. Lett.* **36**, p.1568 (2000).
68. Yoo, S. J. B., Koza, M. A., Bhat, R., and Caneau, C. Bidirectionally pumped difference-frequency generation in AlGaAs waveguides: polarization-independent, multichannel wavelength conversion with input signal filtering capabilities. 6, p.107-108. 1998. San Francisco, CA, Opt. Soc. America. Technical Digest Summaries of papers presented at the Conference on Lasers and Electro-Optics Conference. 5-3-1998.
69. S. J. B. Yoo, C. Caneau, R. Bhat, M. A. Koza, A. Rajhel, and N. Antoniadis, "Wavelength conversion by difference frequency generation in AlGaAs waveguides with periodic domain inversion achieved by wafer bonding," *Appl. Phys. Lett.* **68**, p.2609 (1996).
70. M. S. Stern, "Semivectorial polarised finite difference method for optical waveguides with arbitrary index profiles," *IEEE Proceedings* **135**, p.56 (1988).
71. T. Skauli, O. Levi, P. Kuo, T. Pinguet, M.M. Fejer, J.S. Harris, to be published (2002)